Setting Experimental Bounds on Entangled Two-Photon Absorption Cross Sections

by

Kristen M. Parzuchowski

B.S., Michigan State University, 2017

M.S., University of Colorado, 2020

A thesis submitted to the
Faculty of the Graduate School of the
University of Colorado in partial fulfillment
of the requirements for the degree of
Doctor of Philosophy
Department of Physics
2023

Committee Members:
Ralph Jimenez, Co-Chair
Margaret M. Murnane, Co-Chair
Thomas R. Schibli
Adam Kaufman
Niels H. Damrauer

Parzuchowski, Kristen M. (Ph.D., Physics)

Setting Experimental Bounds on Entangled Two-Photon Absorption Cross Sections

Thesis directed by Prof. Ralph Jimenez

Two-photon absorption (2PA) is widely used in microscopy for deep, sub-cellular imaging. However, the efficiency of 2PA is limited by the properties of both the absorber and the excitation light. Entangled photon pairs produced via spontaneous parametric down-conversion (SPDC) exhibit correlations in energy, time and space that may improve the excitation efficiency relative to a classical laser. The most significant improvement is expected at low photon flux where isolated pairs interact with the absorber. In this regime, the rate of the entangled two-photon absorption (E2PA) process scales linearly with photon flux and the E2PA cross section (σ_E).

Despite over a decade of publications claiming to measure huge σ_E that suggest a quantum advantage exists of up to 10 orders of magnitude, in this thesis I will show strong evidence that σ_E are several orders of magnitude lower than previously reported. First, we provide relevant background information on nonlinear and quantum optics. Next, we discuss theoretical descriptions of σ_E and review the large body of experimental work in the field. Afterwards, we discuss the four experiments we designed to measure E2PA.

In the first and third experiments, we measure SPDC transmittance through samples of two-photon absorbers in room-temperature liquids. In our second experiment, we collect fluorescence from samples excited with SPDC. Despite the high sensitivity of the techniques, we could not resolve a signal in any of the measurements. We set upper bounds on the σ_E of eight independent absorbers that are up to five orders of magnitude lower than previously published σ_E.

The third experiment also served as a classical 2PA (C2PA) measurement system. We made one-to-one comparisons between E2PA and C2PA to bound the quantum advantage. We derived absolute C2PA cross sections that closely agreed with values already reported in literature. In the fourth experiment, we designed a toluene-filled hollow-core-fiber platform for 2PA measurements.

We measured C2PA down to 20 nanowatts, and expect to make further improvements. This platform is at least 4-fold more sensitive than a standard cuvette-based technique and thus is ideal for the next generation of E2PA measurements.

Dedication

To Nathan and Kevin

Acknowledgements

I am so grateful to have been surrounded by so many admirable individuals throughout my time in graduate school. First I would like to thank my family for their unending support. Thank you to my parents, Scott and Mary, for teaching me how to be a strong, independent individual. Thank you to my brothers, Nathan and Kevin, for sparking my interest for science in the first place. Thank you to all of my family members whom there are way too many of to name. Thank you to Benton for your encouragement and all the fun you bring to my life. Thank you to Bindy for always being eager for a break from work. Thank you to my friends from all parts of my life – those who have stuck around since kindergarten to those I have only met this year. You make life more fun! Thanks especially to Raegan, Rick, Dan, Heather, Lilah, Meeko, Sam, Mar and Scout.

To all my teachers – thank you for pushing me to be the best I can be. Thank you to my research advisor at Michigan State, Jaideep Singh, who taught me how to do research well and inspired me to keep doing it. Because of his guidance I sought out graduate schools throughout the country and landed in Colorado – for this I am so grateful. Thank you to my research advisor throughout graduate school, Ralph Jimenez. Thank you for setting me up with an awesome project and team that has prepared me for wherever my career takes me. Under Ralph's guidance I became a confident researcher. Thank you to Marty Stevens for advising me and teaching me how to present in plain English. Thank you to my committee members Margaret Murnane, Thomas Schibli, Adam Kaufman and Niels Damrauer for your guidance.

Thank you to Marty, Mike Mazurek and Thomas Gerrits for teaching me about quantum optics. Thanks to Alex Mikhaylov for teaching me about two-photon absorption and about working

in a lab. Thanks to Alex, Mike and Marty for aligning and realigning optics with me. Thanks to Mike and Marty for countless helpful discussions on experimental designs, data acquisition and data analysis. Thank you to Charlie Camp, Daniel Lum and Meng-Chang Wu for lending your support and advice from Gaithersburg.

Thank you to the Jimenez lab members past and present– Srijit, Alex, Ryan, Samantha, Sheng, Josh, Emma, Nancy, Richard, Sushil, Alan, Miles, Daniel, Annika and Connor. Thanks to Srijit, Alex, Ryan, Samantha, Sheng and Emma for the hikes, the shared meals, the Rec center activities, etc. Thanks to Srijit for keeping me sane during the middle of graduate school. Thanks to Alan, Miles and Daniel for continuing where I left off. I thank the incredible support staff at JILA – without you I would not have been able to complete this research.

Thank you!

Contents

Chapter

Appendix

Tables

Table

Figures

Figure

Chapter 1

Introduction

The field of nonlinear optics involves interactions of light with nonlinear media. Nonlinear optical effects occur in certain materials when the intensity of light is high enough to induce sizable nonlinear terms to the polarization of the material. The lowest order correction to the polarization is expected to be comparable to the linear response when the intensity of the electric field approaches that of atoms (10^{20} W m^{-2}) [1].

The field of quantum optics covers the quantum mechanical properties of the individual quanta of light, photons, and their interactions with matter. These two fields can delve into one another, and we will see that this is the case when we consider the nonlinear processes of spontaneous parametric down-conversion (SPDC) and entangled two-photon absorption (E2PA), both of which concern single photon pairs and nonlinear materials. Although the former process uses the strong field strengths typical of nonlinear optical phenomena, the latter pushes the boundaries of what is and isn't possible in nonlinear optics - using single photon pairs to seed a nonlinear process.

In this chapter we discuss the introductory material necessary for understanding this thesis. First, we look at the theory of second harmonic generation (SHG) and discuss the factors, such as phase-matching, that alter the intensity of the generation process. We then turn to its time reverse process, SPDC, and derive a wave function for the generated light and its intensity distribution. We consider the second-order coherence function and how it can be used to characterize the photon statistics of various sources including SPDC. Finally we discuss two-photon absorption (2PA) and derive the cross section for both one and two-photon absorption.

1.1 Classical Nonlinear Optics

First let's consider the classical Hamiltonian for the electromagnetic field

$$H = \frac{1}{2}\int d^3r[\mathbf{E}\cdot\mathbf{D} + \mathbf{B}\cdot\mathbf{H}], \tag{1.1}$$

where $\mathbf{E}, \mathbf{B}, \mathbf{D} = \epsilon_0\mathbf{E}+\mathbf{P}, \mathbf{H} = \mu\mathbf{B}$ are the electric field, magnetic flux density, electric displacement field and magnetizing field, respectively, ϵ_0, μ are the permittivity of free space and the permeability of the material, respectively, and $\mathbf{P}$ is the polarization of the material. This equation is the integral over space of the electromagnetic energy density. Using Hamilton's equations we derive Maxwell's equations [2],

$$\nabla\cdot\mathbf{D} = 0 \tag{1.2}$$

$$\nabla\cdot\mathbf{B} = 0 \tag{1.3}$$

$$\nabla\times\mathbf{E} = -\frac{\partial\mathbf{B}}{\partial t} \tag{1.4}$$

$$\nabla\times\mathbf{H} = -\frac{\partial\mathbf{D}}{\partial t}, \tag{1.5}$$

where we have assumed that there are no free charges or currents. From here, we can derive the wave equation for nonlinear media [1]

$$\nabla^2\mathbf{E} - \frac{n^2}{c^2}\frac{\partial^2}{\partial t^2}\mathbf{E} = \frac{1}{\epsilon_0 c^2}\frac{\partial^2}{\partial t^2}\mathbf{P}^{\mathrm{NL}}. \tag{1.6}$$

where $\mathbf{P}^{\mathrm{NL}}$ is the nonlinear part of the polarization. The total polarization, $P(t)$, of the material can be expanded to include the nonlinear terms, [1]

$$\begin{aligned}\mathbf{P}(t) = \mathbf{P}^{(1)}(t) + \mathbf{P}^{\mathrm{NL}}(t) &= \mathbf{P}^{(1)}(t) + \mathbf{P}^{(2)}(t) + \mathbf{P}^{(3)}(t) + \mathbf{P}^{(4)}(t) + ...\\ &= \epsilon_0\left(\chi^{(1)}\mathbf{E}(t) + \chi^{(2)}\mathbf{E}^2(t) + \chi^{(3)}\mathbf{E}^3(t) + \chi^{(4)}\mathbf{E}^4(t) + ...\right).\end{aligned} \tag{1.7}$$

Here, $\chi^{(n)}$ refers to the nth-order susceptibility of the medium and $P^{(1)}(t)$ is responsible for the ordinary linear effect of a material to polarize in response to an applied electric field and thus reduce the total electric field within the material. A wide range of nonlinear effects can occur from the higher order terms, and many can be more thoroughly understood using Eq. (1.6).

1.2 Second Harmonic Generation

Let's consider the process of SHG, in which two photons of frequency ω are destroyed and a photon of frequency 2ω is generated as shown in Fig. 1.1(a). We note that SHG is a special case of the process sum-frequency generation (SFG), in which the two photons that are destroyed can have non-degenerate frequencies.

In this section, our formalism is adapted from Ref. [1]. The polarization of the material is generated by two fields at frequency ω, thus we use the first term in the nonlinear polarization, $P^{(2)}$. We can assume that the electric field incident on the material is of the form

$$\mathbf{E}_\omega(\mathbf{r},t) = \mathbf{A}_\omega(\mathbf{r})e^{i(k_\omega z-\omega t)} + c.c., \tag{1.8}$$

where $\mathbf{A}_\omega(\mathbf{r})$ is the amplitude of the field, k_ω is the wavenumber, and the field is propagating in the z direction. We can then write the relevant polarization term as

$$\begin{aligned} P^{(2)} &= 2\epsilon_0 d_{\text{eff}}\mathbf{E}_\omega(\mathbf{r},t)\cdot\mathbf{E}_\omega(\mathbf{r},t) \\ &= 2\epsilon_0 d_{\text{eff}} A_\omega^2(\mathbf{r})(e^{i2(kz-\omega t)}+1) + c.c., \end{aligned} \tag{1.9}$$

where d_{eff} is related to the second order susceptibility tensor $\chi^{(2)}_{ijk}$. The precise form of d_{eff} depends on the polarization directions, propagation directions and frequencies of the optical waves and the symmetry properties of the crystal. The first term is responsible for the SHG and the second for a DC field known as optical rectification. We will drop this second term as it is not relevant for our purposes. We will look for solutions to Eq. (1.6) of the form $\mathbf{E}_{2\omega}(\mathbf{r},t) = \mathbf{A}_{2\omega}(\mathbf{r})e^{i(k_{2\omega}z-2\omega t)} + c.c.$. Plugging Eq. (1.9) into Eq. (1.6), we arrive at

$$\frac{\partial^2}{\partial z^2}A_{2\omega}(z) + 2ik_{2\omega}\frac{\partial}{\partial z}A_{2\omega}(z) + c.c. = -\frac{8d_{\text{eff}}\omega^2}{c^2}A_\omega^2 e^{i\Delta kz} + c.c., \tag{1.10}$$

where $\Delta k = 2k_\omega - k_{2\omega} = 2\omega(n_\omega - n_{2\omega})/c$ is the phase matching term. We assume we are working in the undepleted pump regime where the amplitude A_ω is independent of z. For $A_{2\omega}$, we assume the slowly varying amplitude approximation, which implies that the first term is much smaller than

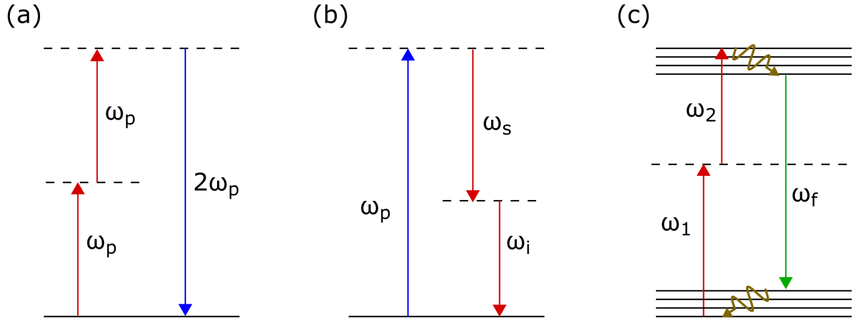

Figure 1.1: Level diagram of (a) second harmonic generation (SHG), (b) spontaneous parametric down-conversion (SPDC) and (c) two-photon absorption (2PA). Frequencies ω_p, $2\omega_p$, ω_s, ω_i, ω_1, ω_2 and ω_f refer to pump, second harmonic, signal, idler, nondegenerate frequency 1, nondegenerate frequency 2 and fluorescence respectively. Solid and dashed lines refer to real and virtual energy levels respectively. In SHG and SPDC energy is conserved. In 2PA, energy is lost through vibrational relaxation in both the excited and ground state (yellow wavy arrow).

the second. We drop the complex conjugate while maintaining the equality and are left with

$$\frac{\partial}{\partial z} A_{2\omega}(z) = i\frac{4d_{\text{eff}}\omega}{cn_{2\omega}} A_\omega^2 e^{i\Delta kz}. \tag{1.11}$$

Next we perform the z integrals and arrive at

$$A_{2\omega}(z) = \frac{4d_{\text{eff}}\omega}{cn_{2\omega}} A_\omega^2 \frac{\left(e^{i\Delta kL} - 1\right)}{\Delta k}. \tag{1.12}$$

We can then solve for the intensity of the second harmonic using the time-averaged Poynting vector, $I_{2\omega} = 2n_{2\omega}\epsilon_0 c|A_{2\omega}|^2$,

$$I_{2\omega} = \frac{8\left(d_{\text{eff}}\omega L\right)^2}{c^2 n_{2\omega} n_\omega^2 \epsilon_0} I_\omega^2 \text{sinc}^2(\Delta kL/2). \tag{1.13}$$

The second harmonic intensity scales quadratically with the pump intensity, which is expected since two photons are needed to produce a second harmonic photon. The intensity is very sensitive to the product of the phase matching parameter and the length of the crystal. For $\Delta k = 0$ or $\Delta k << 1/L$, the SHG efficiency is maximized and the intensity increases quadratically with the length of the crystal.

1.3 Phase Matching

The phase matching parameter, Δk, is important for all parametric nonlinear processes, so here we discuss it more generally. This parameter describes the necessity for momentum conservation.

As the phase product ΔkL increases, the intensity of the field generated from the nonlinear process decreases and then increases in an oscillatory manner. This can be understood as a phase walk-off of the generated beam from the pump. After a certain length of crystal, $L = L_c = 2/\Delta k$, walk-off leads to power flowing back into the pump from the generated beam. If the goal is to produce a sizeable signal, this walk-off should be minimized.

Perfect phase matching ($\Delta k = 0$) can be achieved by finding a material for which the indices of refraction for all of the waves are equal. This is not easy to find, but can be done it multiple ways. Typically the index of refraction of a material increases with frequency (normal dispersion), but it may also decrease with frequency (anomalous dispersion). If the crystal is birefringent, the index of refraction depends on the axis of the crystal. This birefringence can be used to phase match. For certain wavelength and polarization combinations of the high frequency and low frequency fields, the phase matching condition is met. In $\chi^{(2)}$ processes, types 0, I and II phase matching refer to the polarization of the high frequency photon being parallel (orthogonal) to both (neither), neither (both) and one (one) of the low frequency photons, respectively.

More variables can be added to the birefringent phase matching problem if we consider temperature or angle tuning the crystal. The temperature affects the index of refraction and tuning it can change Δk. For angle tuning, we can tilt the crystal and propagate the light along an axis with an index of refraction that is some combination of the indices for the symmetry axes of the crystal.

Another way to phase match is called quasi-phasematching. In this case $\Delta k \neq 0$ for any set of bulk crystal parameters. Instead, the optical domain of the crystal is flipped periodically (once per coherence length, L_c) to walk the waves back into phase with one another before the generated field intensity begins to decrease. This flipping of the optical domain effectively changes the sign of $\chi^{(2)}$ and the crystal is called a periodically poled crystal. If the crystal is periodically poled, it results in a modification where $\Delta k \to \Delta k - \frac{2\pi}{\Lambda}$, where $\Lambda = 2\pi/\Delta k$ is the poling period.

1.4 Spontaneous Parametric Down-conversion

Another nonlinear process called parametric down-conversion (PDC) is the time reverse of SFG. In this process a pump photon is destroyed and two photons are created, a signal and an idler photon, as shown in Fig. 1.1(b). When the process is seeded by a weak signal beam, it's referred to as stimulated PDC or parametric amplification. If there is no seed the process is called spontaneous PDC (SPDC) or parametric fluorescence. Stimulated PDC can be described using classical nonlinear optics, as we showed for SHG, however SPDC, which is seeded only by the vacuum, requires a quantum description.

Here we have adapted the formalism from Ref .[3]. We begin using the classical Hamiltonian for the electromagnetic field, Eq. (1.1). By inserting the expansion of the polarization (Eq. (1.7)), we can split the Hamiltonian into a linear and nonlinear part, $H = H^{\mathrm{L}} + H^{\mathrm{NL}}$. The first term in the nonlinear part takes the form

$$H^{\mathrm{NL}} = \frac{1}{2}\epsilon_0 \int d^3r \chi^{(2)}_{ijl} E_i(\mathbf{r},t) E_j(\mathbf{r},t) E_l(\mathbf{r},t), \tag{1.14}$$

where we have adopted Einstein notation, and $\chi^{(2)}_{ijl}$ depends on the frequencies of pump, signal and idler. To reach the quantum description we must quantize the electromagnetic field. The electric field functions $E(\mathbf{r},t)$ are replaced by field observables $\hat{E}(\mathbf{r},t)$ which separate into a sum of positive, $\hat{E}^{+}(\mathbf{r},t)$, and negative, $\hat{E}^{-}(\mathbf{r},t)$, frequency contributions. The positive contribution takes the form

$$\hat{E}^{+}(\mathbf{r},t) = \frac{1}{V^{1/2}} \sum_{\mathbf{k},s} i \sqrt{\frac{\hbar\omega(\mathbf{k})}{2\epsilon_0}} \hat{a}_{\mathbf{k},s}(t) \boldsymbol{\epsilon}_{\mathbf{k},s} e^{i\mathbf{k}\cdot\mathbf{r}}, \tag{1.15}$$

where s indicates the polarization component, $\mathbf{k}$ indicates the wavevector, $\boldsymbol{\epsilon}$ is a unit polarization vector, $\hat{a}(\hat{a}^{\dagger})$ is the annihilation (creation) operator, and V is the quantization volume.

Since the pump beam is bright enough to be treated classically, we leave the classical electric field function. After making the field replacements for signal and idler fields, the Hamiltonian for the system is of the form

$$\hat{H} = \hat{H}^{\mathrm{L}} + \hat{H}^{\mathrm{NL}} = \sum_{\mathbf{k},s} \hbar\omega(\mathbf{k})(\hat{n}_{\mathbf{k},s} + 1/2) + \frac{1}{2}\epsilon_0 \chi^{(2)}_{ijl} \int d^3r E_i(\mathbf{r},t)\hat{E}_j(\mathbf{r},t)\hat{E}_l(\mathbf{r},t), \tag{1.16}$$

where $\hat{n}$ is the number operator. In the nonlinear Hamiltonian multiple terms arise, but we keep the terms necessary for SPDC,

$$\hat{H}^{\mathrm{NL}} = \frac{1}{2}\epsilon_0 \chi^{(2)}_{ijl} \int d^3r \left(E_i(\mathbf{r},t)\hat{E}^-_j(\mathbf{r},t)\hat{E}^-_l(\mathbf{r},t) + h.c.\right). \tag{1.17}$$

We can compute the wave function of the SPDC state by using first-order time-dependent perturbation theory, where in the interaction picture

$$|\Psi(t)\rangle \approx \left(1 - \frac{i}{\hbar}\int_0^t dt' H^{\mathrm{NL}}(t')\right)|\Psi(0)\rangle, \tag{1.18}$$

where $|\Psi(0)\rangle = |0_1 0_2\rangle$ and 1 and 2 denote signal and idler photons. We make a few assumptions: that the pump is nearly monochromatic, the polarizations of signal and idler photons are fixed, the volume of the crystal is large relative to the wavelength of light and the pump amplitude varies slowly on the timescale of the interaction. Then we arrive at

$$|\Psi(t)\rangle \approx C_0|0_1 0_2\rangle + C_1 \int\int d^3k_1 d^3k_2 \Phi(\mathbf{k}_1,\mathbf{k}_2)\hat{a}^\dagger_1\hat{a}^\dagger_2|0_1 0_2\rangle, \tag{1.19}$$

where C_0 and C_1 are constants, with $C_1 \propto L_z\sqrt{I_p}$ where L_z is the crystal length in the z direction and I_p is the pump intensity. We emphasize here that the intensity of the SPDC increases linearly with pump intensity in contrast to SHG (Sec. 1.2). The joint transverse momentum [4] amplitude is

$$\Phi(\mathbf{k}_1,\mathbf{k}_2) = \mathcal{N}\mathrm{sinc}\left(\frac{\Delta k_z L_z}{2}\right)\nu(\mathbf{q}_p), \tag{1.20}$$

where $\mathcal{N}$ is a normalization constant, $\Delta k_z = k_{1z} + k_{2z} - k_{pz}$ is the phase matching parameter, ν is the transverse pump momentum profile and $\mathbf{q}_p$ is the projection of $\mathbf{k}_p$ onto the transverse plane. If we make a change of variables we can rewrite the function in terms of $\mathbf{q}_1$ and $\mathbf{q}_2$, the projections of $\mathbf{k}_1$ and $\mathbf{k}_2$ onto the transverse plane,

$$\begin{aligned}\Phi(\mathbf{k}_1,\mathbf{k}_2) &= u\left(|\mathbf{q}_1 - \mathbf{q}_2|\right)\nu\left(|\mathbf{q}_1 + \mathbf{q}_2|\right)\\ &= \mathcal{N}\mathrm{sinc}\left(\frac{L_z\lambda_p}{8\pi}|\mathbf{q}_1 - \mathbf{q}_2|^2\right)e^{-\sigma_p^2|\mathbf{q}_1+\mathbf{q}_2|^2}.\end{aligned} \tag{1.21}$$

Here λ_p is the pump wavelength and σ_p is the pump radius. We have made the assumption that the pump profile is Gaussian. We also note that, $|\mathbf{q}_1 - \mathbf{q}_2| = k_1 \sin(\theta_1) - k_2 \sin(\theta_2)$ and $|\mathbf{q}_1 + \mathbf{q}_2| = q_p$. The function $u(|\mathbf{q}_1 - \mathbf{q}_2|)$ is set by phase matching and the function $\nu(|\mathbf{q}_1 + \mathbf{q}_2|)$ is set by the pump profile. Here we note that this form of the joint transverse momentum amplitude illuminates that it is not separable into a function that depends only on the transverse momentum of signal and another for idler, rather the amplitude is separable into functions that depend on the difference or sum of the transverse momenta of signal and idler. This shows that the two photons are entangled.

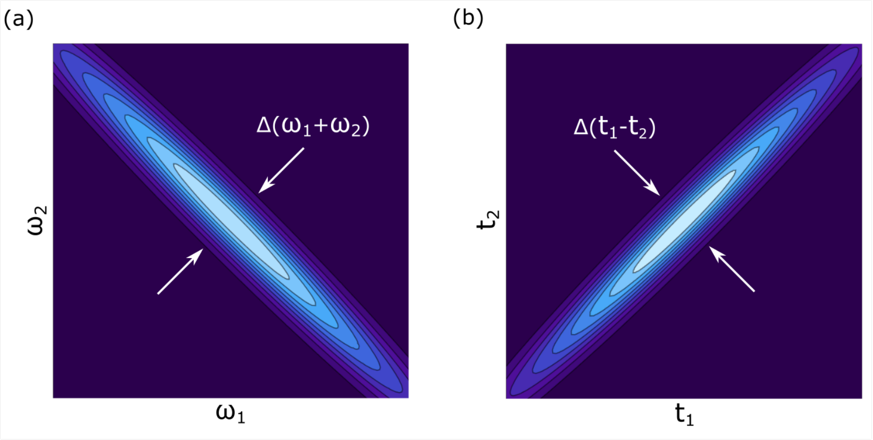

Figure 1.2: A schematic of a (a) joint spectral intensity (JSI) and (b) joint temporal intensity (JTI) of entangled photons produced via spontaneous parametric down-conversion. The diagonal width $\Delta(\omega_1 + \omega_2)$ of the JSI is set by the bandwidth of the pump laser and $\omega_1 + \omega_2$ is equal to the pump laser frequency. The antidiagonal width $\Delta(t_1 - t_2)$ of the JTI is inversely proportional to the bandwidth of the entangled photons [5]. This width is sometimes referred to as the entanglement time, T_e. T_e can increase as the beam propagates due to the group velocity dispersion of the optics the beam propagates through.

We can easily find the joint transverse momentum intensity, which is $|\Phi(\mathbf{k}_1, \mathbf{k}_2)|^2$. If we write the joint transverse momentum amplitude in terms of frequencies by making the substitutions of $k_i \rightarrow \omega_i n_i / c$, we end up with the joint spectral amplitude, $\Phi(\omega_1, \omega_2)$, and can likewise solve for the joint spectral intensity (JSI). A schematic of a JSI for SPDC is shown in Fig. 1.2(a). We can write the joint transverse-momentum or spectral amplitude in space or time coordinates, respectively, using a Fourier transform. In the space and time domain we will refer to these as the joint transverse-position or temporal amplitudes. A schematic of a joint temporal intensity (JTI) is shown in Fig. 1.2(b).

A number of useful quantities can be extracted from these various intensities. From the joint transverse-position intensity, we can find the entanglement area A_e. The width of the 2-dimensional distribution of an idler photon's position conditioned on the signal photon's position is $\propto \sqrt{A_e}$. It can be measured or calculated for a given transverse plane of the SPDC's propagation, and is known to be affected by optical elements. A lens, for example, performs a Fourier transform on an imaged object [3, 4]. If the lens is placed one focal length in front of the crystal, the Fourier transform of the SPDC beam at the crystal will lie at one focal length past the lens. This changes the position correlations in the image plane to position anticorrelations in the Fourier plane. An accurate comparison of measurement to calculation requires careful consideration of the optical path. We can even estimate a "birth zone" [3] of the SPDC by considering the crystal plane. From the JTI, we can determine the entanglement time, T_e. This quantity is the width of the distribution of idler arrival times conditioned on signal arrival time. The values of T_e and A_e are set by the temporal and spatial second-order coherence functions, $g^{(2)}$ [6, 7].

1.5 Second-Order Coherence Function

An important quantity to characterize the photon statistics of a light source is the second-order coherence function. In this section we follow the formalism of Refs. [8, 9]. First consider the first-order correlation function,

$$G_j^{(1)}(\mathbf{r}_1, t_1) = \left\langle \hat{\mathbf{E}}_j^-(\mathbf{r}_1, t_1) \hat{\mathbf{E}}_j^+(\mathbf{r}_1, t_1) \right\rangle , \tag{1.22}$$

where j indicates the mode of light that is measured at position r_1 and time t_1. This function is proportional to the counting rate of a photodetector. Next, consider a mode of light j measured at position r_1 and time t_1 and another mode k measured at r_2 and t_2, the rate at which the photodetectors detect a coincidence is proportional to the second-order correlation function,

$$G_{j,k}^{(2)}(\mathbf{r}_1, t_1; \mathbf{r}_2, t_2) = \left\langle \hat{\mathbf{E}}_j^-(\mathbf{r}_1, t_1) \hat{\mathbf{E}}_k^-(\mathbf{r}_2, t_2) \hat{\mathbf{E}}_k^+(\mathbf{r}_2, t_2) \hat{\mathbf{E}}_j^+(\mathbf{r}_1, t_1) \right\rangle . \tag{1.23}$$

It's useful to use a normalized version of these correlation functions, which at second order is written

$$\begin{aligned} g^{(2)}_{j,k}(\mathbf{r}_1, t_1; \mathbf{r}_2, t_2) &= \frac{G^{(2)}_{j,k}(\mathbf{r}_1, t_1; \mathbf{r}_2, t_2)}{G^{(1)}_{j}(\mathbf{r}_1, t_1) G^{(1)}_{k}(\mathbf{r}_2, t_2)} \\ &= \frac{\left\langle \hat{\mathbf{E}}^{-}_{j}(\mathbf{r}_1, t_1)\hat{\mathbf{E}}^{-}_{k}(\mathbf{r}_2, t_2)\hat{\mathbf{E}}^{+}_{k}(\mathbf{r}_2, t_2)\hat{\mathbf{E}}^{+}_{j}(\mathbf{r}_1, t_1)\right\rangle}{\left\langle \hat{\mathbf{E}}^{-}_{j}(\mathbf{r}_1, t_1)\hat{\mathbf{E}}^{+}_{j}(\mathbf{r}_1, t_1)\right\rangle \left\langle \hat{\mathbf{E}}^{-}_{k}(\mathbf{r}_2, t_2)\hat{\mathbf{E}}^{+}_{k}(\mathbf{r}_2, t_2)\right\rangle}. \end{aligned} \tag{1.24}$$

This function is referred to as the second-order coherence function in recognition of its ability to determine if a photon source is coherent ($|g^{(n)}| = 1$). Common factors can be canceled, and we can write this in terms of only creation and annihilation operators

$$g^{(2)}_{j,k}(\mathbf{r}_1, t_1; \mathbf{r}_2, t_2) = \frac{\left\langle \hat{a}^{\dagger}_{j}(\mathbf{r}_1, t_1)\hat{a}^{\dagger}_{k}(\mathbf{r}_2, t_2)\hat{a}_{k}(\mathbf{r}_2, t_2)\hat{a}_{j}(\mathbf{r}_1, t_1)\right\rangle}{\left\langle \hat{a}^{\dagger}_{j}(\mathbf{r}_1, t_1)\hat{a}_{j}(\mathbf{r}_1, t_1)\right\rangle \left\langle \hat{a}^{\dagger}_{k}(\mathbf{r}_2, t_2)\hat{a}_{k}(\mathbf{r}_2, t_2)\right\rangle}. \tag{1.25}$$

Then, if the measurement is on a single mode ($j = k$) measured at the same place ($r_1 = r_2$) and if the source is stationary (does not depend on exact values of t_1 and t_2), we can reduce this to the form

$$g^{(2)}(\tau) = \frac{\left\langle \hat{a}^{\dagger}(t)\hat{a}^{\dagger}(t+\tau)\hat{a}(t+\tau)\hat{a}(t)\right\rangle}{\left\langle \hat{a}^{\dagger}(t)\hat{a}(t)\right\rangle^{2}}, \tag{1.26}$$

where $\tau = t_2 - t_1$. For the special case of $\tau = 0$,

$$g^{(2)}(0) = \frac{\langle \hat{n}(t)(\hat{n}(t) - 1)\rangle}{\langle \hat{n}(t)\rangle^{2}}. \tag{1.27}$$

Depending on the optical setup, including the type of laser and detectors, there are different ways in which we can measure and calculate $g^{(2)}(0)$ as described in Ref. [9]. In the case relevant for this thesis of a pulsed source with photons detected using a Hanbury Brown-Twiss (HBT) interferometer with "click" detectors as schematically shown in Fig. 1.3(a), we can measure $\gamma^{(2)}_{\text{click}}$,

$$\gamma^{(2)}_{\text{click}}[m] = \frac{N_c[m]}{R_1 R_2 T_{\text{rep}} T_{\text{int}}}, \tag{1.28}$$

where R_1 and R_2 are the singles count rates on detectors 1 and 2 and $N_c[m]$ is the number of correlation events recorded by timing electronics in the histogram bin centered at an integer m number of pulses with width set by the repetition period T_{rep} for an experiment integration time T_{int}. The quantity $N_c[m]$ can be called the number of coincidences, and refers to the number of

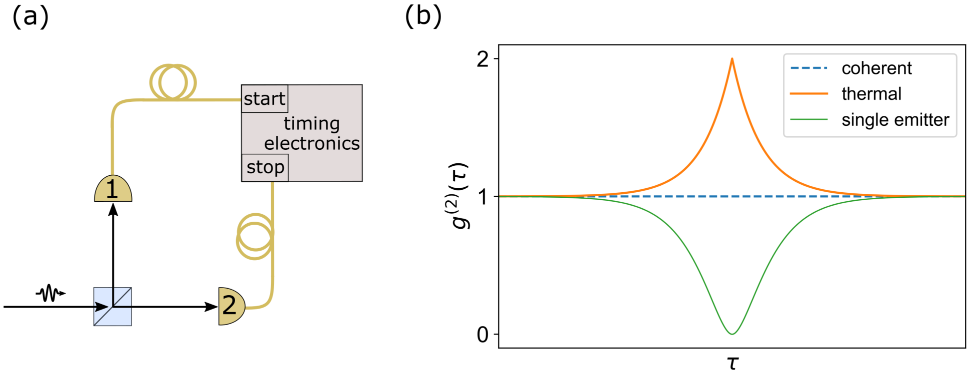

Figure 1.3: Schematic of (a) a Hanbury Brown-Twiss interferometer. Light is incident on a beamsplitter and detected at the two output ports on detectors 1 and 2. If detector 1 and detector 2 register photons within a short time window (coincidence) the difference in time (start-stop) is recorded. This time is τ for the second order coherence function ($g^{(2)}(\tau)$) measurements. (b) The second order coherence function for a coherent source, a thermal source and a single driven atomic emitter [10].

times a click on detector 1 is followed by a click on detector 2 within the repetition period. The quantity $\gamma^{(2)}_{\text{click}}[0]$ equals $g^{(2)}[0]$ when the photon detection efficiency or the multi-photon generation probability is very low [9].

In Fig. 1.3(b), the $g^{(2)}(\tau)$ values for sources demonstrating a range of photon statistics is shown. A value of $g^{(2)}(0) = 1$ is consistent with a coherent beam of light from a laser, and demonstrates Poissonian photon statistics. For $g^{(2)}(0) < 1$ the light shows sub-Poissonian photon statistics and is consistent with a single-photon source. For $g^{(2)}(0) > 1$ the light shows super-Poissonian photon statistics and is consistent with thermal light. Classical light fields are constrained to $g^{(2)} \geq 1$. Signal or idler photons follow a thermal distribution with $g^{(2)}(0) = 2$. SPDC has a $g^{(2)}(0)$ value that depends on the mean photon number. A degenerate, single-mode (in all degrees of freedom: polarization, spatial mode, spectral and temporal profiles) SPDC source can be modeled as a single-mode squeezed vacuum (SMSV), for which $g^{(2)} = 3 + 1/\mu$ [11] where $\mu = \langle \hat{a}^\dagger \hat{a} \rangle$ is the mean photon number.

1.6 Two-Photon Absorption

Next we turn to a $\chi^{(3)}$ nonlinear process: 2PA. In this process two photons are absorbed by an absorber, such as an atom or molecule, and a transition is made from a ground to excited state as shown in Fig. 1.1(c). Unlike the parametric process' SHG and SPDC, this process is non-parametric. In a parametric process, the initial and final quantum states of the system are identical. The only time that the system is not in this state is when it occupies a virtual state. In a non-parametric process, the final state is a different and real quantum state of the system. The part of the susceptibility involved in describing a parametric process is the real part and for non-parametric is the imaginary part.

We can derive the cross section for 2PA in multiple ways, here we will opt to derive it using second-order time-dependent perturbation theory for state amplitudes, as was done first by Maria Gӧppert-Mayer in 1931 [12]. We note that as pointed out in Ref. [5], this method considers only the double quantum coherence (DQC) pathway's contribution to 2PA, but the non-rephasing (NR) and rephasing (R) pathways also exist and may contribute especially if there are real intermediate states close to resonance with the exciting field. These pathways can be found using a fourth-order perturbative treatment of density matrices. Another method to derive the 2PA cross section is in terms of $\chi^{(3)}$ using energy considerations, see for example Ref. [13].

We will follow the derivation in Ref. [1] closely that considers an atom interacting with an electric field. The Hamiltonian for this system can be written as

$$\begin{aligned}\hat{H} &= \hat{H}_0 + \hat{V}(t) \\ &= \hat{H}_0 + \hat{d}E(t),\end{aligned} \tag{1.29}$$

where $\hat{H}_0$ is the free Hamiltonian for the atom, $\hat{d} = -e\hat{r}$ is the electric dipole moment operator, e is the charge of an electron, $\hat{r}$ is the position operator and

$$E(t) = Ee^{i\omega t} + c.c. \tag{1.30}$$

is a monochromatic electric field. We assume that the atomic wave function, $\psi(\mathbf{r}, t)$ obeys the

Schrödinger equation,

$$i\hbar\frac{\partial}{\partial t}\psi(\mathbf{r},t) = \hat{H}\psi(\mathbf{r},t). \tag{1.31}$$

The solution for the wave function of this system can be expressed as

$$\begin{aligned}\psi(\mathbf{r},t) &= \sum_l a_l(t)\psi_l(\mathbf{r},t)\\ &= \sum_l a_l(t)u_l(\mathbf{r})e^{-i\omega_l t},\end{aligned} \tag{1.32}$$

where $\psi_l(\mathbf{r},t)$ are the eigenstates of the free Hamiltonian and $a_l(t)$ is the time-dependent coefficient. Inputting Eq. (1.32) into Eq. (1.31), multiplying by $u_m^*(\mathbf{r})$ and integrating over all space we find

$$i\hbar\frac{\partial}{\partial t}a_m(t) = \sum_l a_l(t)V_{ml}e^{-i\omega_{lm}t}, \tag{1.33}$$

where $\omega_{lm} = \omega_l - \omega_m$ and

$$V_{ml} = \int d^3r u_m^*(\mathbf{r})\hat{V}u_l(\mathbf{r}). \tag{1.34}$$

Since Eq. (1.33) cannot be solved exactly, we instead perturbatively solve the equation by replacing V with λV, where λ is the expansion parameter (which varies from 0 to 1 depending on the strength of the perturbation), and expanding $a_m(t)$ in powers of the interaction,

$$a_m(t) = a_m^{(0)} + \lambda a_m^{(1)} + \lambda^2 a_m^{(2)} + \lambda^3 a_m^{(3)} + ... \tag{1.35}$$

Then we arrive at the generalized equation for any N,

$$i\hbar\frac{\partial}{\partial t}a_m^{(N)} = \sum_l a_l^{(N-1)}V_{ml}e^{-i\omega_{lm}t}. \tag{1.36}$$

First, we consider the first-order process which corresponds to one-photon absorption (1PA). Before the laser is turned on we assume that the atom is in the ground (g) state, corresponding to $a_g^{(0)} = 1$ and $a_l^{(0)} = 0$ for all $l \neq g$. Next we determine that

$$V_{mg} = -d_{mg}Ee^{-i\omega_{mg}t} + c.c. \tag{1.37}$$

The first term will correspond to 1PA, whereas the second to stimulated emission. We drop the second term as we are only interested in the absorption process. Then after integration over t we arrive at

$$a_m^{(1)}(t) = \frac{d_{mg}E}{\hbar(\omega_{mg}-\omega)}(e^{i(\omega_{mg}-\omega)t}-1). \tag{1.38}$$

We can describe the probability that the atom is in state m by

$$p_m^{(1)}(t) = |a_m^{(1)}(t)|^2 = \frac{|d_{mg}E|^2}{\hbar^2}\frac{4\sin^2((\omega_{mg}-\omega)t/2)}{(\omega_{mg}-\omega)^2} = \frac{|\mu_{mg}E|^2}{\hbar^2}f(t), \tag{1.39}$$

where the function $f(t)$ can be approximated by a Dirac delta function for long interaction times t,

$$f(t) = 2\pi t\delta(\omega_{mg}-\omega). \tag{1.40}$$

With this delta function the probability amplitude describes an infinitely narrow transition. To approach a more realistic description, we can give the state m some finite width in frequency space. We introduce the density of final states, $\rho_f(\omega_{mg})$ where $\rho_f(\omega_{mg})d\omega_{mg}$ is the probability that the transition frequency lies between ω_{mg} and $\omega_{mg}+d\omega_{mg}$. Then we have

$$\begin{aligned} p_m^{(1)}(t) = {} & \frac{|d_{mg}E|^2}{\hbar^2}2\pi t\int d\omega_{mg}\delta(\omega_{mg}-\omega)\rho_f(\omega_{mg}) \\ & = \frac{|d_{mg}E|^2}{\hbar^2}2\pi t\rho_f(\omega_{mg}=\omega). \end{aligned} \tag{1.41}$$

Next we derive the one photon transition rate (Fermi's golden rule)

$$\begin{aligned} R_{mg}^{(1)} &= p_m^{(1)}(t)/t \\ &= \frac{|d_{mg}E|^2}{\hbar^2}2\pi\rho_f(\omega_{mg}=\omega). \end{aligned} \tag{1.42}$$

We can now solve for the purely atomic quantity, the 1PA cross section,

$$\sigma_{mg}^{(1)} = R_{mg}^{(1)}/\phi = \frac{|d_{mg}|^2\omega}{n\epsilon_0 c\hbar}\pi\rho_f(\omega_{mg}=\omega), \tag{1.43}$$

where $\phi = \frac{2n\epsilon_0 c}{\hbar\omega}|E|^2$ is the photon flux. The 1PA cross section is quoted in units of cm^2, with typical cross sections on the order of 10^{-16} cm^2. To derive the 2PA cross section, we follow the exact same procedure, but at second order in the interaction. One can show that the probability of being in state n is

$$p_n^{(2)}(t) = |a_n^{(2)}(t)|^2 = \left|\sum_m \frac{d_{nm}d_{mg}E^2}{\hbar^2(\omega_{mg}-\omega)}\right|^2 2\pi t\rho_f(\omega_{ng}=2\omega). \tag{1.44}$$

Then the two-photon transition rate can be written

$$R_{ng}^{(2)} = p_n^{(2)}(t)/t = |a_n^{(2)}(t)|^2 = \left| \sum_m \frac{d_{nm} d_{mg} E^2}{\hbar^2 (\omega_{mg} - \omega)} \right|^2 2\pi \rho_f(\omega_{ng} = 2\omega). \tag{1.45}$$

In later sections we will refer to this as R. Next, we define the 2PA cross section

$$\sigma_{ng}^{(2)} = 2R_{ng}^{(2)}/\phi^2 = \left| \sum_m \frac{d_{nm} d_{mg} \omega}{\hbar n \epsilon_0 c (\omega_{mg} - \omega)} \right|^2 \pi \rho_f(\omega_{ng} = 2\omega). \tag{1.46}$$

In later sections, we will refer to this quantity as σ_C. It's useful to note that Eq. (1.46) is written for degenerate 2PA, however the cross section can be derived for nondegenerate 2PA by adding a second field to Eqn. (1.30). The factor of 2 in Eq. (1.46) differs from that shown in Ref. [1], but agrees with the formalism of Refs. [14, 15]. It holds the units of photons per molecule and makes the units for the cross section cm^4 s photon^{-1} molecule^{-1}. This convention is used in this thesis so that the cross section refers to the removal of two photons from the field and one molecule from the ground state. Typically σ_C are quoted in terms of GM (Goeppert-Mayer) units, where 1 GM = 10^{-50} cm^4 s photon^{-1} molecule^{-1}.

Typical values of σ_C for molecules are on the order of 1 to 100 GM [16, 17]. These values require that a high flux laser ($> 10^{25}$ photons cm^{-2} s^{-1}) be used to observe an absorption signal. Typically pulsed lasers meet these requirements by producing bursts of photons in a short time. However, the shorter the pulse in time, the wider the bandwidth of the photons and thus the more difficult it is for the sum of the energies of the photons to equal the transition energy. Among the many photons incident on the absorbing sample, only a small fraction (typically $< 10^{-15}$) are absorbed. Those that are absorbed arrived within the required short time window, which is set by the virtual state lifetime (femtoseconds [18]), and arrived close enough to the absorber to interact with it. Clearly, this excitation process is inefficient.

Chapter 2

Entangled Two-Photon Absorption

2.1 Publication Note

Parts of this chapter are adapted from:

[19] Parzuchowski, K.M., Mikhaylov, A., Mazurek, M.D., Wilson, R.N., Lum, D.J., Gerrits, T., Camp Jr, C.H., Stevens, M.J. and Jimenez, R., 2021. Setting bounds on entangled two-photon absorption cross sections in common fluorophores. *Physical Review Applied*, *15*(4), p.044012.

2.2 Introduction

In the previous chapter we discussed spontaneous parametric down-conversion (SPDC) and two-photon absorption (2PA), and pointed out the inefficiency of the 2PA process. In this chapter we discuss entangled 2PA (E2PA). This process refers to the excitation of a two-photon transition using a light source of entangled photons produced via SPDC.

Despite the inefficiency of 2PA, the process is widely used in two-photon excitation microscopy (2PEM) for cellular imaging deep within biological tissue [20, 21]. Excitation of a two-photon transition occurs much more efficiently at the focus than outside of the focal volume, which leads to a huge boost in resolution relative to a one-photon based technique. Fluorescence from the relaxation of the absorber is collected to reconstruct an image. 2PEM can only image about 1 mm deep into living brain tissue. Imaging to greater depths would require a higher laser intensity that perturbs the biological function of the tissue. Alternatively, a different light source that is more efficient at excitation of 2PA could be used.

Numerous theoretical and experimental studies have investigated the possibility of enhancing the efficiency of 2PA by exciting with nonclassical light [22, 11]. Photon pairs that are entangled in the energy-time and position-momentum degrees of freedom can exhibit the strong temporal and spatial correlations needed for 2PA. Theoretical studies on simple model systems [23, 24, 6] have predicted that using entangled photon pairs can lead to a significant "quantum advantage" in 2PA rates. Here we define quantum advantage as the ratio of the minimum photon flux necessary to observe classical 2PA (C2PA) to that for E2PA.

We will first look into the derivation of the E2PA cross section (σ_E) as was first done by Fei et al. [6] and discuss why a simpler definition is more useful for the experimental conditions used in this thesis. We then present the simple probabilistic model for the cross section similar to that shown by Fei et al. [6], and connect C2PA to E2PA. For a more comprehensive review of the theory of E2PA we suggest the work of Drago and Sipe [25] and Raymer and coworkers [5, 26, 27] .

Afterwards, we will discuss the range of E2PA experiments in literature, emphasizing that the size and measurability of the cross sections is under debate. We also present the challenges of reporting E2PA cross sections. Finally we will discuss the signatures of E2PA that serve as tools for designing and conducting an E2PA measurement.

2.3 Quantum Mechanical E2PA Cross Section

To derive σ_E, we can again (Sec. 1.6) use second-order time-dependent perturbation theory. We emphasize again that as mentioned in Raymer et al. [5], this derivation considers only the double-quantum coherence pathway and leaves out other pathways that may contribute to 2PA especially when the excitation field is near resonance with real intermediate states. Similar to the theoretical derivations of SPDC, we must adopt a quantum description. The probability of two-photon absorption can be written [28]

$$\begin{aligned}
p_f^{(2)} &= \left| \frac{1}{\hbar^2} \int_{t_0}^{t} dt_2 \int_{t_0}^{t_2} dt_1 \langle f|\hat{d}(t_2)\hat{d}(t_1)|i\rangle \langle \Psi_f|\hat{E}_2^{(+)}(t_2)\hat{E}_1^{(+)}(t_1)|\Psi_i\rangle \right|^2 \\
&= \frac{1}{\hbar^4} \int_{t_0}^{t} dt_2' \int_{t_0}^{t_2'} dt_1' \int_{t_0}^{t} dt_2 \int_{t_0}^{t_2} dt_1 \langle i|\hat{d}^\dagger(t_2')\hat{d}^\dagger(t_1')\hat{d}(t_2)\hat{d}(t_1)|i\rangle \\
&\qquad \times \langle \Psi_f|\hat{E}_1^{(-)}(t_2')\hat{E}_2^{(-)}(t_1')\hat{E}_2^{(+)}(t_2)\hat{E}_1^{(+)}(t_1)|\Psi_f\rangle, \qquad (2.1)
\end{aligned}$$

where $|i(f)\rangle$ denotes the initial (final) state wave function of the electron, $|\Psi_{i(f)}\rangle$ denotes the initial (final) state wave function of the optical field. Here we have considered the case where the field described by $\hat{E}_1^{(+)}(t_1)$ interacts first and $\hat{E}_2^{(+)}(t_2)$ interacts second [28]. We can take note that the probability (Eq. 2.1) consists of a material correlation function, M, and a second-order field correlation function, $G^{(2)}$,

$$p_f^{(2)} = \frac{1}{\hbar^4} \int_{t_0}^{t} dt_2' \int_{t_0}^{t_2'} dt_1' \int_{t_0}^{t} dt_2 \int_{t_0}^{t_2} dt_1 M(t_2', t_1', t_2, t_1) G^{(2)}(t_2', t_1', t_2, t_1). \qquad (2.2)$$

By replacing the field correlation function with the product of classical field amplitudes, we can recover Eq. (1.44). Evaluation of this equation for SPDC excitation shows that the field and material parameters are inseparable, leading to a definition for σ_E that depends on both field and absorber properties. It's important to note here that the time ordering of the fields and dipole moment operators results in E_1 and E_2 in Eq. (2.2) being associated to the first and second arriving photons, respectively, of a frequency anticorrelated pair [29, 30]. The relevant $G^{(2)}$ function is thus subtly different than the standard form in Eq. (1.23). The form of $G^{(2)}$ in Eq. 2.2 reduces to the standard $G^{(2)}(0)$ when the linewidth of the absorber's final state is significantly broader than the bandwidth of the exciting field [29, 30, 26].

The probability of E2PA is known to depend linearly, rather than quadratically, on photon flux [6, 24, 23] at low photon flux. The rate of E2PA contains both a linear component and the classical quadratic component that dominates at high photon flux

$$R_E = \frac{1}{2}(\sigma_E \phi + \sigma_C \phi^2). \qquad (2.3)$$

Using Eq. (1.19), (2.3) and (2.2) one can derive the σ_E. Here we've taken the derivation from Ref. [6] in the special case of a monochromatic pump and converted from natural to cgs units, used our convention for the factor of 2 in Eq. (2.3) and added in a density of final states, ρ_f,

$$\sigma_E = \frac{\pi\omega_1\omega_2}{2A_eT_e(\hbar n\epsilon_0 c)^2}\rho_f(\omega_{fi} = \omega_1 + \omega_2)$$
$$\times \left| \sum_j \left\{ D_{21}^{(j)} \frac{1 - \exp[-iT_e\Delta_1^{(j)} - T_e\kappa_j/2]}{\Delta_1^{(j)} - i\kappa_j/2} + D_{12}^{(j)} \frac{1 - \exp[-iT_e\Delta_2^{(j)} - T_e\kappa_j/2]}{\Delta_2^{(j)} - i\kappa_j/2} \right\} \right|^2, \tag{2.4}$$

where $D_{kl}^{(j)} = \langle f|d_k|j\rangle\langle j|d_l|i\rangle$ are the transition dipole matrix elements, k and l refer to photons 1 and 2 or vice versa, $\Delta_{1(2)}^{(j)} = \omega_j - \omega_i - \omega_{1(2)}$ is an energy mismatch parameter and κ_j is the intermediate state linewidth.

Large oscillations in σ_E as a function of T_e ("entanglement induced two-photon transparencies" [6]) have been theoretically predicted for a few atoms and molecular fluorophores [31, 32, 33], but have not been measured experimentally. For large values of $T_e\kappa_j$ the interference will wash out and σ_E approaches the probabilistic model we present below (Eq. (2.11)) [6]. Furthermore, as the degrees of freedom of the absorber increases (i.e. for large molecules, absorbers that interact with eachother, absorbers that interact with the surrounding medium and vibronic coupling) the amount of coherence between the photons and the absorber decreases, and σ_E is expected to approach the classical limit [31]. The absorbers studied in this thesis are large molecules or quantum dots dissolved in room-temperature solvents, and thus likely can be approximated by the probabilistic model.

2.4 Probabilistic E2PA Cross Section

Here we present a connection between a simple probabilistic theory describing E2PA and the well-accepted description of C2PA. We consider a single-mode field with mean photon number $\mu = \langle \hat{a}^\dagger \hat{a} \rangle$, the 2PA rate can be written [11, 34]

$$R = \kappa_2 \left\langle {\hat{a}^\dagger}^2 \hat{a}^2 \right\rangle = \kappa_2 \mu^2 g^{(2)}, \tag{2.5}$$

where κ_2 (s^{-1}) is a collection of constants quantifying the strength of the nonlinear interaction. It has been demonstrated, for example, that thermal light ($g^{(2)} = 2$) doubles the 2PA rate compared to laser excitation ($g^{(2)} = 1$) of the same intensity [35].

In the classical limit, the instantaneous 2PA rate for a single fluorophore can be written [15]

$$R = \frac{1}{2}\sigma_C \phi^2, \tag{2.6}$$

where ϕ is the photon flux, with units of cm^{-2} s^{-1}. The C2PA cross-section σ_C has units of GM, where $1\,\mathrm{GM} = 10^{-50}$ cm^4 s. (In this section we omit photons, excitations and fluorophores/absorbers from the units of various quantities for brevity; in later chapters we include them for clarity.)

For a pulsed laser ($g^{(2)} = 1$) source with temporal and spatial mode set by the pulse duration T (fs) and the beam area A (cm^2), if we rewrite Eq. (2.5) in terms of the photon flux, $\phi = \mu/(TA)$, and substitute

$$\kappa_2 = \frac{\sigma_C}{2T^2A^2}, \tag{2.7}$$

we arrive at the classical limit in Eq. (2.6).

In contrast to laser light, SPDC produces photon pairs exhibiting correlations in energy, time and space that can be tailored to enhance the rate and selectivity of 2PA [36, 37]. The energy correlations between the signal and idler photons within a pair are set by conservation of energy in the conversion of one pump photon to two down-converted photons and can be engineered to match the energy of a two-photon transition. Photon pair production is localized in space and time [3, 38], allowing for excitation with photons that nearly simultaneously arrive in a localized region of space.

A degenerate, single-mode (in all degrees of freedom: polarization, spatial mode, spectral and temporal profiles) SPDC source can be modeled as a single-mode squeezed vacuum (SMSV), for which $g^{(2)} = 3 + 1/\mu$ [11]. Substituting this expression into Eq. (2.5) yields

$$R = \kappa_2 \left(\mu + 3\mu^2\right). \tag{2.8}$$

For a pulsed source, substituting ϕ and Eq. (2.7) into Eq. (2.8) gives

$$R = \frac{1}{2}\sigma_C \left(\frac{\phi}{TA} + 3\phi^2\right). \tag{2.9}$$

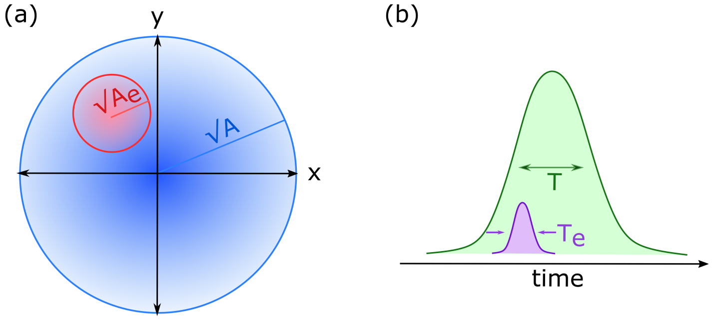

Figure 2.1: (a) Schematic of entanglement area, A_e, and beam area, A. Photons closely correlated in space may have A_e smaller than A. (b) Schematic of entanglement time, T_e, and the duration of either the pump pulse or the overall SPDC pulse, T. Photons closely correlated in time may have T_e smaller than T.

An alternative way to write Eq. (2.8) is [6]

$$R_E = \frac{1}{2}\left(\sigma_E \phi + 3\sigma_C \phi^2\right), \tag{2.10}$$

where σ_E has units of cm^2 and R_E is the instantaneous E2PA rate. For a single-mode field, the two cross sections are related by $\sigma_\mathrm{E} = \sigma_C/(TA)$. At low photon flux, the first term dominates and the E2PA process should scale linearly with ϕ [23, 24]. We note that it is more precise to say that the E2PA rate is linear in *photon number*, as Eq. (2.8) shows. If pulse duration or spot size were modified, the linear term should scale in the same way as the quadratic term, at least in the single-mode case considered here. At high photon flux, where many photon pairs overlap in time, the quadratic term dominates.

In a real experiment, the SPDC light typically occupies multiple modes and Eq. (2.8) does not hold. In this case, the coefficient for the linear term could in principle be larger than the coefficient for the quadratic term. Roughly speaking, if the two photons in a pair are more closely correlated in time than the pump pulse duration, the interaction strength could be enhanced by the factor T/T_e, where T_e is the entanglement time. Analogously, if the photons in a pair are more closely correlated in space than the beam size, the interaction strength could be modified by the factor A/A_e, where A_e is the entanglement area. A schematic of these quantities is illustrated in

Fig. 2.1. Following this simple, probabilistic argument leads to the approximation

$$\sigma_E \approx \frac{\sigma_C}{T_{\mathrm{e}} A_{\mathrm{e}}}. \tag{2.11}$$

Other than a factor of two difference due to our different definition of σ_E, this is the same approximation arrived at in Ref. [6], but following a different argument and making different assumptions. To maximize the E2PA rate, T_{e} and A_{e} should be as small as possible. For a large μ and a large number of modes, $g^{(2)} \rightarrow 1$ and the E2PA rate approaches the classical limit in Eq. (2.6).

Unlike σ_C, which depends only on wavelength for a particular molecular 2PA transition, the value of σ_E depends strongly on the properties of the excitation source and experiment. The values of A_e and T_e evolve as the SPDC beam propagates through optics from the down-conversion crystal to the sample [39, 40, 41, 42, 7, 43], and therefore depend on the details of the optical system used to measure E2PA. Calculating σ_E for a given experimental geometry thus requires knowledge of A_e and T_e within the excitation volume. Clearly, these factors complicate the ability to compare results from different experiments.

2.5 Experimental Literature Summary

There are broadly two experimental designs used for measuring E2PA as shown schematically in Fig. 2.2. The first is a transmittance-based experimental scheme, where a beam of entangled photon pairs is sent through a sample and the transmittance (the fraction of photon pairs that are transmitted through the sample) is measured. The second is a fluorescence-based experimental scheme, where a beam of entangled photon pairs is sent through a sample and the fluorescence that is emitted from the absorber is collected. Each of these techniques has their own unique advantages. For transmittance measurements, one can use a sample that has a low quantum yield and one can use a low photon pair flux. The latter of which is because the measured signal is a fractional change of transmission and increasing the incident flux does not increase the value in the low flux regime. Furthermore, the detectors must count single photons, thus low photon rates can be measured. For fluorescence measurements, the desired signal is background free and the alignment of these setups

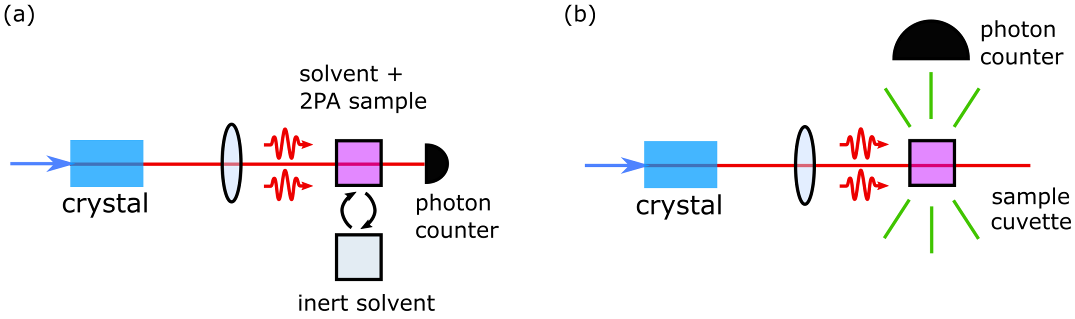

Figure 2.2: (a) Schematic of a transmittance-based measurement scheme. Photon pairs are generated by SPDC in a $\chi^{(2)}$ nonlinear crystal and sent through a cuvette containing a solvent and 2PA sample, then through a cuvette containing only the solvent. The ratio of photon counts detected for the two measurements gives the transmittance. (b) Schematic of a fluorescence-based measurement scheme. Photon pairs are generated by SPDC in a $\chi^{(2)}$ nonlinear crystal and sent through a cuvette containing a solvent and 2PA sample. Fluorescence photons are counted on a detector angled at 90° relative to the beam propagation direction.

can be less sensitive. The latter of which is because the measured signal is not typically collected onto a small detector, such as single-mode fiber-coupled detectors, far from the source, which is more likely in a transmittance measurement.

The SPDC sources used in E2PA experiments can vary. The pump laser, for example, can be continuous wave (CW) or pulsed. For a CW-pumped SPDC excitation source, the linear photon-flux-dependent term in Eq. (2.10) will remain dominant over the quadratic term at higher average fluxes than for that of a pulsed-pumped SPDC excitation source. This is because of the lower likelihood of uncorrelated pairs arriving at a fluorophore at the same time. SPDC sources vary in phase matching types (Section 1.3) and thus the photons in a pair may have perpendicular or parallel polarizations. Furthermore, an experimental design may rotate the polarization of one photon relative to its partner photon. Studies of C2PA [44, 45, 46] suggest that there is a small difference in efficiency (by a factor of two or three) of excitation when the two photons have perpendicular polarizations instead of parallel.

A summary of important parameters in selected E2PA reports is given in Table 2.1. These studies represent experimental efforts from all three of the independent groups that have claimed to

Table 2.1: Results and experimental parameters from selected E2PA studies. Cross sections (σ_C and σ_E) are quoted at the corresponding excitation wavelength (λ). Cross sections and entanglement times (T_e) are found as described in the main text. We estimate the entanglement area (A_e^{est}) required to explain the σ_E values based on Eq. (2.11).

Sample [Ref.]	λ (nm)	σ_C (GM)	σ_E (10^{-19} cm^2 fluorophore^{-1})	T_e (fs)	A_e^{est} (10^{-9} μm^2)
9R-S [47]	800	27.9	$2.02 - 2.69$	100	$1.0 - 1.4$
Rh6G [48]	1064	9.9 ± 1.5 [16]	$0.0099 - 0.019$	140	$38 - 72$
RhB [49]	808	260 ± 40 [16]	$0.17 - 42$	17	$3.6 - 900$
Tetraannulene [50]	800	2960	990	96	0.31

measure a signal from E2PA. Table 2.1 shows σ_C and σ_E values determined at several near infrared wavelengths. In Ref. [47], pulsed-pumped type-II SPDC was generated to excite a sample with $1-25\times10^6$ photons s^{-1} (the beam waist is not specified) in transmittance- and fluorescence-based E2PA schemes. For the studied 9R-S molecule, the σ_E values found using these two techniques differ slightly from one another. The measurement uncertainty was estimated to be 9% and 12% for transmittance- and fluorescence-based techniques. In Ref. [48], a continuous-wave (CW)-pumped type-0 SPDC source was used for entangled two-photon excited fluorescence (E2PEF) measurements with an effective incident photon rate of $2 - 50 \times 10^7$ photons s^{-1} (beam waist of 60 μm). A 100 times increase of the molar concentration led to a decrease in the measured σ_E value for Rhodamine 6G (Rh6G) by a factor of two. The uncertainties on the measured σ_E were estimated to be nearly 50%. A similar concentration dependence was observed in Ref. [49] using pulsed-pumped type-II SPDC excitation with an incident pair rate of $50 - 7,000$ photon pairs s^{-1} (beam waist of 61 μm) in a transmittance-based scheme, where the concentration dependence of σ_E for Rhodamine B (RhB) was attributed to potential aggregation effects in the solutions. The uncertainties on the published σ_E are $\approx$ 10%. In Ref. [50], a pulsed-pumped type-II SPDC source was used to excite the tetraannulene sample with $1 - 25 \times 10^6$ photons s^{-1} in a transmittance-based E2PA scheme. The measurement uncertainty was not estimated in this report. The values for σ_E of 990×10^{-19} cm^2 fluorophore^{-1} for tetraannulene [50] and 0.0099×10^{-19} cm^2 fluorophore^{-1} for Rh6G [48] are the largest and smallest values, respectively, that have been reported. In all these reports the photon flux is not specified, except for an order-of-magnitude estimate in Ref. [49], and the photon rate is not precisely defined.

No direct T_e measurements were completed in the aforementioned reports. In the case of Ref. [48] we estimate T_e based on the details provided by the authors, who estimated an effective flux reduced to the fraction of photon pairs that have $T_e = 140$ fs. In Refs. [47, 49, 50], the value of T_e was estimated at the output of the crystal, which in some cases can be orders of magnitude smaller than the value at the sample's position. This is especially true when the total group delay dispersion (GDD) of the optics is large or when the bandwidth of the SPDC is large (Chapter 3 Section 3.7). The value of T_e would be very sensitive to even small amounts of GDD in the latter case.

The values of A_e are not specified in any of these reports. We estimate the entanglement areas, A_e^{est}, required to explain the results of these previous reports, based on the probabilistic model, Eq. (2.11). The values of A_e^{est} range from $10^{-6} - 10^{-10}$ μm^2. This would require both photons within a pair to be confined to a region that is $10^{-6} - 10^{-10}$ times the diffraction limited spot size. We have no evidence that this level of confinement is feasible [41, 42, 40, 7]. Thus, the simple, probabilistic theory [6] used to derive Eq. (2.11) cannot explain these experimental results.

In addition to the inconsistencies of the results in Table 2.5 with theory, these reports have only measured one signature of E2PA. As we will explain in the next Section, the signature that they measure is not unique to E2PA and thus the origin of the signal is unclear. Another camp of researchers exist, including our researchers, that have not been able to resolve a signal due to E2PA, but have designed a sensitive experiment capable of measuring E2PA cross section upper bounds (σ_E^{UB}).

To the best of our knowledge, a complete summary of experimental results of E2PA is given in Table A.1 and shown in Fig. 2.3. This plot shows σ_E (marked by various blue × symbols) and σ_E^{UB} (marked by various orange ▼ symbols) values as a function of σ_C. From lightest to darkest, the shades of blue represent the results from University of Geneva [48], University of Michigan [47, 50, 51, 52, 53, 54, 55, 56] and Universidad de los Andes [49]. From lightest to darkest

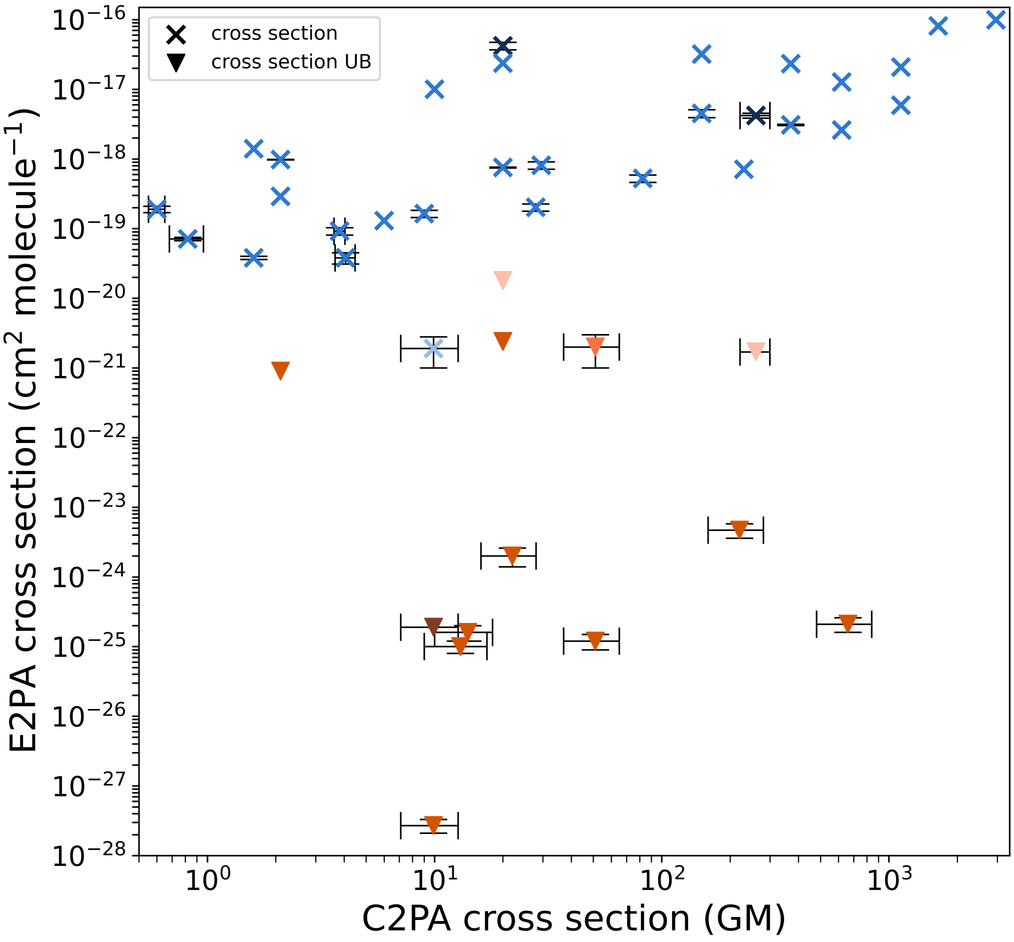

Figure 2.3: E2PA cross sections (marked by various blue × symbols) and cross section upper bounds (marked by various orange ▼ symbols) reported throughout literature. The values are plotted as a function of σ_C. Each shade of blue or orange indicates results from a different organization as mentioned in the main text. The data used for this plot can be found in Table A.1.

the shades of orange represent the results from Universidad Nacional Autónoma de México [57], California Institute of Technology [58], JILA/National Institute of Standards and Technology [59, 19, 60, 61](the work presented in this thesis) and University of Oregon [62]. The σ_E^{UB} have values lower than the reported σ_E, signifying the stark disagreement between these two groups. The size of σ_E has yet to be narrowed down which is evident by the vertical axis extending 12 orders of magnitude. The reports of σ_E^{UB} are recent, being published in the last 2 years, whereas the reports of σ_E have spanned 16 years and are primarily being published by one group.

The σ_E^{UB} used for Refs. [61, 57, 58, 62] were not provided in those publications, but were estimated in a similar manner to those used in our publications [59, 19] as shown in Appendix A. We note that some groups chose not to discuss their results in terms of E2PA cross sections in part because of the large variability of the value from one experiment to the next (Sec. 2.4). We use it in this thesis to make orders-of-magnitude comparisons between the results from various groups.

2.6 Signatures of E2PA

Although numerous experiments in literature report that E2PA signals are large and measurable, it is unclear what the origin of the measured signal is. In order to claim that a signal has a particular origin, a unique signature (or preferably multiple signatures) of the process must be identified. Here we discuss a number of signatures of E2PA, however this list is not exhaustive.

The most commonly known signature of E2PA is its linear dependence on excitation photon flux at low photon flux (Eq. (2.10)). This signature is not unique to E2PA and is shared with many other processes such as scattering, one photon absorption, or fluorescence from the coating of an optic in the beam path. Nevertheless, this signature is typically the only signature of E2PA measured by the groups who report σ_E.

Another signature of E2PA is the signal's dependence on the time delay between photons in a pair; as the time delay is scanned away from optimal overlap (zero time delay), the signal is expected to decrease towards zero in accordance with the simultaneity requirement of 2PA. In a recent report, Tabakaev *et al.* [48] observe such behavior in an E2PEF experiment. An interferometer was used before the sample to probabilistically and equally split photons and time delay half of the photon pairs, while the other half traversed the same path. The resulting E2PEF as a function of the time delay should consist of a constant signal due to the photon pairs that traveled the same path and a variable signal due to the photon pairs that traveled different paths. The signal at long time delays should be half the signal at zero delay. Instead, Tabakaev *et al.* observe a signal that tends to zero at large time delays. This unexpected result is pointed out by the authors of the study, but it has yet to be explained. Some of the other reports [51, 63, 64] have included time-delay scans, but with data reported at only a few delays.

Another signature of E2PA is the signal's dependence on the presence of both photons in a pair. If only one photon from each pair makes it to the two-photon absorber, the signal should disappear. This test could be performed in a straightforward manner by adding a longpass or shortpass filter centered at the pump wavelength (one must ensure that the alignment of the system does not change). This was done in our publication [61] and was used as confirmation that the origin of the signal was not E2PA. For type II SPDC, this can also be done by adding a polarizer to the beam. Another way to check for this signature is to probabilistically and equally split photons into two paths of an interferometer and block one arm of the interferometer, the signal should reduce to a quarter of its original size.

One variation of this previous signature is to attenuate the SPDC beam and observe a quadratic decrease of the signal. This differs from attenuation of the pump beam, which would cause the signal to scale linearly. This difference can be understood mathematically.

In the case of linear loss between the SPDC generation crystal and the sample, the 2PA rate (Eq. (2.5)) is modified [9]

$$R = \kappa_2 \mathcal{T}^2 \left\langle {\hat{a}^{\dagger}}^2 \hat{a}^2 \right\rangle = \kappa_2 \mathcal{T}^2 \mu^2 g^{(2)}, \tag{2.12}$$

where the linear loss has been modeled as a lossless beamsplitter with transmittance $\mathcal{T}$. For excitation with a pulsed single-mode SPDC source,

$$R = \frac{1}{2}\sigma_C \mathcal{T}^2 \left(\frac{\phi_{xtal}}{TA} + 3\phi_{xtal}^2 \right), \tag{2.13}$$

where ϕ_{xtal} is the photon flux in the SPDC crystal (in our notation this is photon flux, not photon pair flux). Rewriting in terms of the photon flux at the sample ($\phi_{sample} = \mathcal{T}\phi_{xtal}$) yields

$$R_E = \frac{1}{2}\left(\sigma_E \mathcal{T}\phi_{sample} + 3\sigma_C \phi_{sample}^2\right). \tag{2.14}$$

To extract σ_E, the flux at the sample should be scaled by $\mathcal{T}$. If the flux is adjusted by attenuating the pump power, the first term in R_E should scale linearly with ϕ_{sample}. If the flux is instead adjusted by attenuating the down-converted light, this term should scale quadratically with ϕ_{sample}. This signature should be present in either transmittance- or fluorescence-based measurement schemes. This loss-scaling signature was demonstrated in up-conversion of down-conversion by Dayan *et al.* [65, 66], and can be used as a method to distinguish E2PA from other linear loss processes.

2.7 Thesis Overview

The overall objective of this thesis work is to experimentally investigate E2PA in molecules dissolved in room temperature solvents. At the beginning of our research project we sought to replicate some aspects of the experimental design of previous works where sensational claims were made about the quantum advantage of E2PA. We soon found that we were not able to reproduce the results from these reports and in fact were not able to measure a signal at all. Afterwards we had to rethink our experimental design in order to increase our sensitivity. We designed sensitive fluorescence and transmittance experiments, but still could not measure a signal. We were the first to report upper bounds on σ_E, and we have done so for eight independent absorbers. Lastly, we designed a new platform for more sensitive 2PA measurements.

In Chapter 3 we describe the SPDC source used for these various experiments. We detail the capabilities of our systems and the methods used for characterizing this source.

In Chapter 4 we detail our first transmittance experiment. This setup includes an interferometer to test for time delay signatures of E2PA. We demonstrate how one could misinterpret one-photon losses as a signature of E2PA, and go on to account for these losses. We set an upper bound on the E2PA cross section of the studied sample, which shows disagreement with results in literature. The sensitivity of this experiment was limited by residual interference.

In Chapter 5 we discuss our fluorescence experiment. In this experiment we use our maximum SPDC flux and achieve our highest cross section sensitivity. We study both C2PA and E2PA in the same setup under nearly identical excitation conditions. Our C2PA measurements for the six studied samples are used to derive C2PA cross sections which all agree within a factor of two to the values published in literature. For E2PA we cannot measure a signal above our noise floor, and set upper bounds on the cross sections.

In Chapter 6 we cover our second transmittance experiment. Here we take lessons from our previous setup and design a higher sensitivity experiment. We redesign the interferometer and improve our data acquistion and analysis techniques to allow for long but stable measurements. We achieve a sensitivity to 0.05% change in transmittance, which is a 20-fold improvement from the last experiment. However, we do not measure a signal for any of seven samples measured at various concentrations. We set upper bounds on the E2PA cross sections for these molecules.

In Chapter 7 we describe our toluene-filled hollow-core-fiber platform for fluorescence measurements. Here we confine the sample and light into a 37 cm-long, $5\,\mu$m diameter tubing. We measure C2PA down to ≈ 20 nW excitation power. This is a four-fold improvement from the previous fluorescence experiment. We expect that we can use higher concentration samples to measure C2PA at lower powers.

In Chapter 8 we conclude our work and discuss work that was not included in this thesis. In another experiment, we found that the process hot-band absorption can mimic E2PA. This process could be the source of the signals measured by other groups. We discuss future work including the use of the fiber experiment for E2PA studies.

Chapter 3

Entangled Photon Source and Characterization

3.1 Publication Note

Parts of this chapter are adapted from:

[59] Mikhaylov, A., Parzuchowski, K.M., Mazurek, M.D., Lum, D.J., Gerrits, T., Camp Jr, C.H., Stevens, M.J. and Jimenez, R., 2020, February. A comprehensive experimental system for measuring molecular two-photon absorption using an ultrafast entangled photon pair excitation source. In *Advanced Optical Techniques for Quantum Information, Sensing, and Metrology* (Vol. 11295, pp. 48-61). SPIE.

and

[19] Parzuchowski, K.M., Mikhaylov, A., Mazurek, M.D., Wilson, R.N., Lum, D.J., Gerrits, T., Camp Jr, C.H., Stevens, M.J. and Jimenez, R., 2021. Setting bounds on entangled two-photon absorption cross sections in common fluorophores. *Physical Review Applied*, *15*(4), p.044012.

3.2 Introduction

In this chapter we discuss the setup and characterization of the entangled photon source used in the three E2PA measurements covered in this thesis. First we discuss the design of the source. Next we discuss the multi-mode detection stage, where all spatial modes of the SPDC are detected for the measurement and calibration of our mean photon number. Then we discuss the single-mode detection stage, which is used to detect a single spatial mode of SPDC. Using this setup we can characterize the joint spectrum, the entanglement time and $g^{(2)}(0)$. Finally we discuss entanglement area.

3.3 SPDC Source

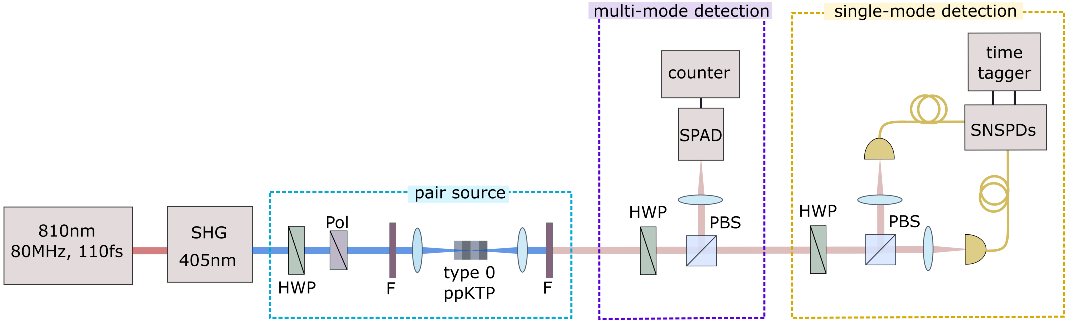

Figure 3.1: Schematic of the SPDC source and detection stages. The 810 nm pump laser (red) is frequency doubled (blue) in an SHG unit. A half-wave plate (HWP) and polarizer (pol) control the power. The light is filtered (F) and focused into a type-0 ppKTP crystal to generate SPDC. The pump light is filtered (F) out, and the SPDC is sent to either the multi-mode or single-mode detection stage. For multi-mode detection, all the light is focused onto a free-space-coupled single-photon avalanche diode (SPAD). For single-mode detection, all the light is sent into an Hanbury Brown-Twiss interferometer and launched into two single-mode fibers where it is detected on superconducting nanowire single-photon detectors (SNSPDs).

A schematic of our photon pair source and detection stages is shown in Fig. 3.1. A pump laser emits ≈ 110 fs pulses with a center wavelength of 810 nm (≈ 9 nm bandwidth) at a repetition rate of 8×10^7 pulses s^{-1}. The pulse duration and bandwidth is measured on a SwampOptics Grenouille 8-50-USB. The laser is frequency doubled via second-harmonic generation (SHG) to produce 405 nm light (≈ 3 nm bandwidth). A half-wave plate (HWP) and polarizer (pol) are used to control the power. Any remaining 810 nm light is filtered out. The beam is focused with a 300 mm lens into a type-0 periodically poled potassium titanyl phosphate (ppKTP) crystal to generate collinear SPDC photon pairs at 810 nm. The crystal is temperature controlled at $30.00°\mathrm{C} \pm 0.01°\mathrm{C}$. The beam size at the focus in the crystal is approximately 30 μm. Filters are used to remove the remaining 405 nm light. The part numbers for the components used in the experiments discussed in Chapters 4, 5, 6, and 7 (including those shown in Fig. 3.1) are listed in Appendices C, E, G, and I.

3.4 Characterizing Mean Photon Number

In this section, we seek to characterize the mean photon number of the multimodal SPDC. We discuss values for various parameters that were measured during the fluorescence experiment discussed in Chapter 5. To characterize the SPDC mean photon number at the sample (μ_{sample}), we direct all the SPDC light to the multi-mode detection stage shown in Fig. 3.1, which consists of a silicon single-photon avalanche diode (SPAD). We measure the count rate at low photon flux, and correct for the SPAD dead time and efficiency, the photon statistics of the down-conversion source, and the difference in optical losses between the two paths. We perform this procedure for three low photon fluxes (where the SPAD is not saturated), and then extrapolate to the high flux used in the fluorescence measurements. This high flux is the maximum flux we can produce from our source due to the damage threshold of our crystal.

For a measured count rate Q_{meas} on the SPAD, the measured click probability per laser pulse is

$$P_{click}^{meas} = \frac{Q_{meas}}{g}, \tag{3.1}$$

where $g = 8 \times 10^7$ pulses s^{-1} is the pulse repetition rate. Assuming a non-paralyzing dead time, the dead-time-corrected click probability can be found using [67]

$$P_{click}^{corr} = \frac{P_{click}^{meas}}{1 - N_{dead} P_{click}^{meas}}, \tag{3.2}$$

where N_{dead} is the number of laser pulses the SPAD is dead for following detection of a photon. We measure the dead time of this SPAD as ≈ 52 ns, implying that $N_{dead} = 4$. For a pump power of 50 μW, we measure $Q_{meas} = 4.4 \times 10^6$ cnt s^{-1}, and hence $P_{click}^{meas} = 0.055$. The dead-time-corrected click probability is $P_{click}^{corr} = 0.071$. This is the per-pulse click probability we would have expected to measure in the absence of dead time.

Converting this click probability to mean photon number requires knowledge of the system detection efficiency (η_{SDE}) and the photon statistics of the SPDC source. These can be related through the expression [68]

$$P^{corr}_{click} = \sum_{n=1}^{\infty}[1 - (1 - \eta_{\mathrm{SDE}})^n]P(n), \tag{3.3}$$

where $P(n)$ represents the probability that a pulse of SPDC light contains n photons at the output of the down-conversion crystal. At a wavelength of 810 nm, we calculate 83% cumulative transmittance of all the optics between the SPDC crystal and the SPAD based on manufacturer specifications. The manufacturer-specified efficiency of the SPAD is 55%. Thus the system detection efficiency is $\eta_{\mathrm{SDE}} \approx 0.46$. The photon number distribution of a SMSV can be written [11]

$$P(n) = \frac{\mu_{xtal}^{n/2} n!}{2^n (\frac{n}{2}!)^2 (1 + \mu_{xtal})^{(n+1)/2}} \tag{3.4}$$

for n even and $P(n) = 0$ for n odd. Here μ_{xtal} is the mean photon number generated at the down-conversion crystal. At 50 μW pump power ($P^{corr}_{click} = 0.071$ and $\eta_{\mathrm{SDE}} = 0.46$), we solve Eqs. (3.3) and (3.4) for μ_{xtal}. These numbers are consistent with a SMSV with mean photon number $\mu_{xtal} = 0.22$.

Although a SMSV can be a good first approximation to an SPDC source, our source emits into many spatial and spectral modes, as evidenced in part by the joint spectral measurements in Fig. 3.3(a). To approximate the many modes in our SPDC light, we perform a Bernoulli sampling of M equally populated SMSVs, each with mean photon number μ_{xtal}/M, assuming $\eta_{\mathrm{SDE}} = 0.46$ for all modes. We substitute the resulting photon probability distribution $P(n)$ into Eq. (3.3) for a range of M varying from 1 to 100, and find the resulting μ_{xtal} to only change in the range from 0.22 (one mode) to 0.21 (100 modes). Although we do not know exactly how many modes are present, the number of modes does not significantly impact the resulting value of μ_{xtal}, so we use the value of 0.22 for 50 μW pump power.

We repeat this procedure at two other low pump powers (75 and 100 μW), and extrapolate the resulting linear fit to find $\mu_{xtal} \approx 147$ photons pulse^{-1} at the maximum pump power of 30 mW. Correcting this for the 24% loss between the SPDC crystal and the sample yields $\mu_{sample} \approx 112$ photons pulse^{-1}. This mean photon number is used to calculate the peak photon flux at the sample using Eq. (5.12).

We can estimate the number of SPDC spectral modes based on the ratio of the SPDC to laser spectral widths, which gives ≈ 8 spectral modes. It follows that there are ≈ 14 photons mode^{-1} pulse^{-1} at the sample. For these operating conditions, at which many pairs are spectrally and temporally overlapped, we may expect a significant contribution to any measured signal from the classical term in the E2PA rate (Eq. (2.3)).

3.5 Superconducting Nanowire Single-Photon Detectors

In the single-mode detection stage (Fig 3.1) the light is sent into an HBT interferometer (Fig. 1.3) and each arm is focused into a fiber held in a fiber launching stage. The 5 m-long single-mode fiber patch cables are connected to superconducting nanowire single-photon detectors (SNSPDs). The SNSPDs are cooled down to ≈ 4 K with a closed-cycle helium cryocooler. The SNSPDs' temperature is monitored. Bias and readout modules are used to extract the digitized and amplified signals that are analyzed with a time tagger triggered to the laser. The singles and coincidence rates are measured.

3.6 Time-of-Flight Spectrometer

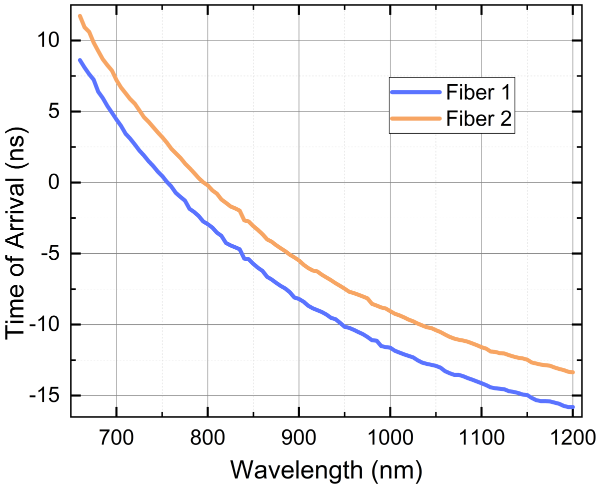

Figure 3.2: Measured time of arrival (ns) of photons as a function of their wavelength (nm) for the two 500-m-long fibers

To build a time-of-flight fiber-based spectrometer [69], the 5-m-long patch cables in the single-mode detection stage (Fig. 3.1) are attached to 500-m-long fibers that then connect to the SNSPDs. The fiber group delay dispersion causes the various frequency components of the photons to spread out in time and thus get detected at different times. These arrival times can thus be associated to the frequency of the light.

We characterized the fiber dispersion by launching the pulsed laser into the fiber, tuning the wavelength in the range 660-1200 nm in 5 nm steps. The time of arrival of the laser (centered at each wavelength) at the detector relative to the laser trigger pulse was recorded. We did the measurement with the 5-m-long patch cables only and with the 5-m-long patch cables attached to the long fibers. We subtracted the time of arrival for the short fiber from the time of arrival for the long fiber. We plotted time of arrival as a function of wavelength in Fig. 3.2. Using the slopes of these curves in the 825-875 nm range, we can extract the dispersion parameter of the fiber, which is -0.111 ± 0.004 and -0.115 ± 0.004 ns nm^{-1} km^{-1} in close agreement with the manufacturer's specifications at 850 nm of -0.106 ± 0.004 ns nm^{-1} km^{-1}. At the wavelength range of interest, 785-835 nm, the slopes are both -0.055 ± 0.002 ns nm^{-1}.

To measure the joint spectral intensity (JSI), we direct all the SPDC to the single-mode detection stage shown in Fig. 3.1 with the 500-m-long fibers attached. We operate at a low pump power such that we expect up to one photon pair to be generated per pulse. The signal and idler detection times for each coincidence are recorded. We accumulate coincidences until the shape of the JSI has a large signal to noise ratio and the structure stops changing. Initially we have a plot of idler photon arrival times as a function of signal photon arrival times. We use the characterized dispersion parameter of the fiber to convert the axes of the measured JSI from time of arrival to wavelength. In Fig. 3.3(a) we show the JSI of the SPDC source without any bandpass filters. The unfiltered SPDC source was used for the fluorescence experiment discussed in Chapter 5. In the transmittance measurements discussed in Chapters 4 and 6, bandpass filters filtered the SPDC to 9 and 11 nm FWHM respectively. The shape of the JSI indicates the expected wavelength anticorrelation of SPDC. Taking the projection of the JSI on the vertical and horizontal axes (for type-0 SPDC these can be called signal and idler projections, or vice versa) reveals several results, see Fig.3.3(b). The vertical and horizontal projections are shown in red and blue, respectively, with FWHM of 72 and 79 nm. The various features in the spectra and the detuning from degeneracy is likely a result of a combination of measurement artifacts, such as the spectral profiles of the optics.

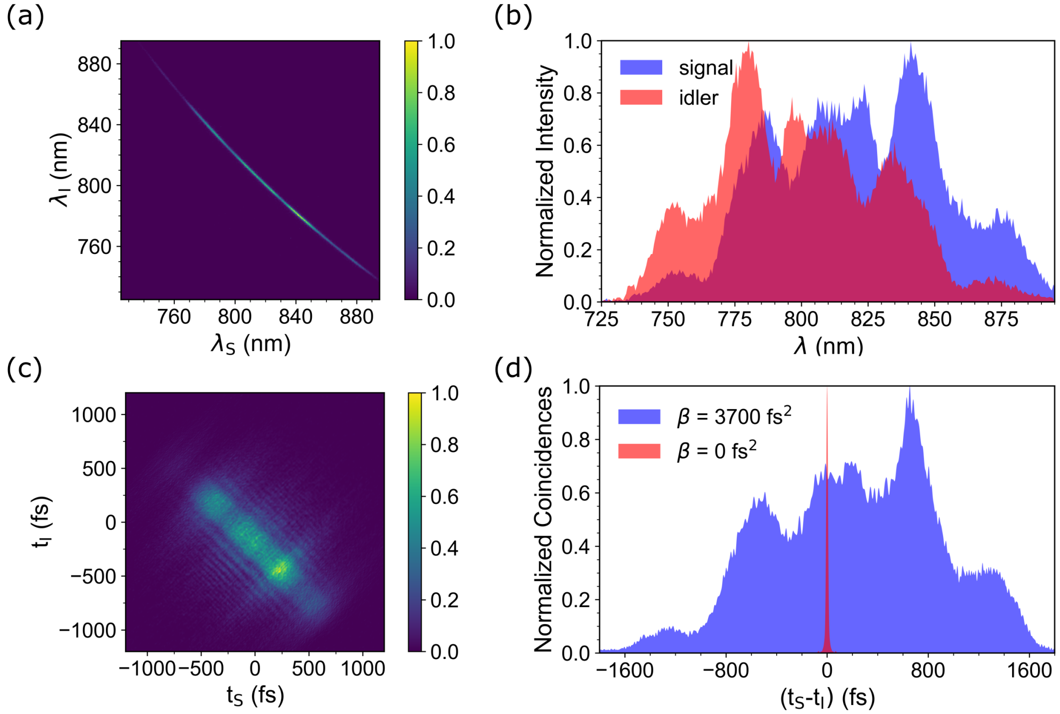

Figure 3.3: (a) Measured joint spectral intensity (JSI) where $\lambda_{\mathrm{S,I}}$ are the signal and idler wavelengths. (b) The JSI is projected onto the horizontal axis and vertical axis showing the signal (blue) and idler (red) spectra respectively. The FWHM of the signal and idler spectra are 79 and 72 nm respectively. The overlap of the spectra is evident in the dark red region. (c) Calculated joint temporal intensity (JTI) obtained through a discrete Fourier transform as described in the main text. (d) Projection onto the antidiagonal axis, t_{S}-t_{I}, of the JTI shown in (c) (blue) and for a transform-limited ($\beta = 0\,\mathrm{fs}^2$) pulse (red). The FWHM of these projections are 1620 fs and 17 fs.

3.7 Entanglement Time

In this section we discuss how we estimate the entanglement time T_e of our SPDC source at the sample. Here we consider the conditions in the fluorescence experiment as discussed in Chapter 5.

For the transmittance experiments discussed in Chapters 4 and 6, we discuss the estimation of the entanglement time for those experimental conditions within the chapters themselves.

The entanglement time is the width of the temporal $g^{(2)}$ function [6], which can be estimated as the FWHM of the antidiagonal projection of the joint temporal intensity (JTI) distribution. We do not measure the JTI directly; instead we calculate it based on our measured JSI. Computing the JTI from the JSI requires knowledge of the spectral phase of the SPDC. We do not have a measurement of this phase; instead we estimate the accumulated group delay dispersion (β) of the pulse from the center of the crystal to the center of the sample to be 3700 fs^2. Our most dispersive elements are the polarizing beamsplitter and the ppKTP crystal. We set the joint spectral amplitude (JSA) in the frequency domain to the square root of the JSI in the frequency domain multiplied by the phase factor due to β, $\mathrm{JSA} = \sqrt{\mathrm{JSI}}e^{i\beta(\omega_\mathrm{S}-\omega_\mathrm{P}/2)^2/2}e^{i\beta(\omega_\mathrm{I}-\omega_\mathrm{P}/2)^2/2}$ where ω_S, ω_I, and ω_P are the frequencies of the signal, idler and pump fields, respectively. In asserting this, we assume that the SPDC is transform limited in the center of the crystal and that the only significant accumulated phase factor is that due to β. We note that β for signal photons would be distinct from that for idler photons if the two were instead orthogonally polarized [39]. This is due to birefringence of various optical elements. We perform a discrete Fourier transform on the JSA to obtain the joint temporal amplitude (JTA). The magnitude squared of the JTA gives the JTI shown in Fig. 3.3(c). The projection of the JTI onto the antidiagonal ($\mathrm{t_S}$-$\mathrm{t_I}$) is shown in blue in Fig. 3.3(d).

We find that $T_e \approx 1620\,\mathrm{fs}$. This can be compared with a transform-limited ($\beta = 0\,\mathrm{fs}^2$) pulse (Fig. 3.3(d) in red) that has $T_e \approx 17\,\mathrm{fs}$. The projections of the JTI onto horizontal and vertical axes both have FWHMs of 1040 fs. This width is a good approximation for the pulse duration of signal and idler beams because it is significantly larger than the pump pulse duration.

To make a probabilistic estimate of the advantage of lossless dispersion compensation or a dispersion-free setup on the rate of E2PA in our experiment, we consider how dispersion affects the SPDC's fulfillment of the simultaneity requirement of 2PA. This simultaneity requirement asserts that two photons must arrive at the absorber within a time window (Δt) set by the absorber's virtual state lifetime. For a dispersed pulse, fewer of the SPDC photon pairs arrive within this

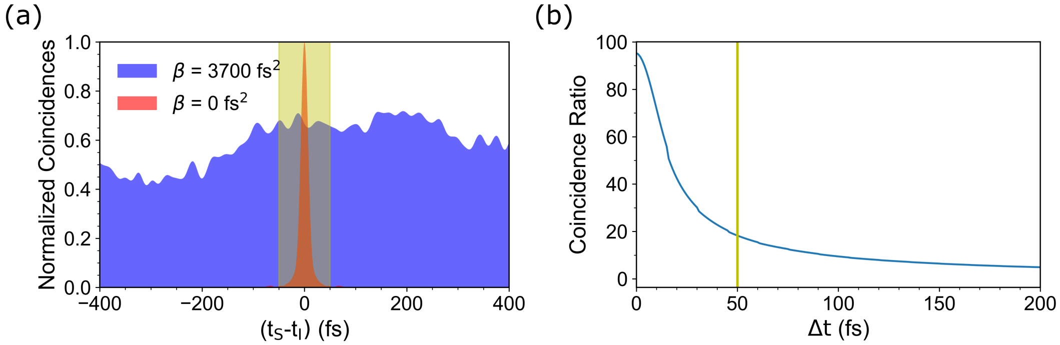

Figure 3.4: (a) The joint temporal intensity from Fig. 3.3(c) with a yellow filled-in region indicating a 50 fs time window (see main text for explanation). (b) The ratio of the number of coincidences of the transform-limited SPDC satisfying the relation $|\mathrm{t_S} - \mathrm{t_I}| \leq \Delta\mathrm{t}$ to that for the dispersed SPDC ($\beta = 3700$ fs^2) as a function of Δt. The yellow bar indicates the 50 fs time window shown in (a).

time window. A precise calculation of the virtual state lifetime of these large molecular absorbers is not feasible, however we can consider any arbitrary time window. In Fig. 3.4(a) the projection of the JTI from Fig. 3.3(d) is shown with a reduced range along the horizontal axis, along with a time window $\Delta\mathrm{t} = 50\,\mathrm{fs}$ indicated in yellow. The number of photon pairs of the transform limited SPDC ($\beta = 0\,\mathrm{fs}$) which satisfy $|\mathrm{t_S} - \mathrm{t_I}| \leq \Delta\mathrm{t}$ divided by the number of photon pairs of the dispersed SPDC ($\beta = 3700\,\mathrm{fs}$) which satisfy the same constraint (called the coincidence ratio) is shown in Fig. 3.4(b) as a function of Δt. A yellow bar indicates the 50 fs time window shown in Fig. 3.4(a). For the smallest possible Δt we can consider based on our resolution (1 fs), the coincidence ratio is 95. Thus a factor of 95 more photon pairs of the transform-limited SPDC satisfy $|\mathrm{t_S} - \mathrm{t_I}| \leq 1$ fs than for the dispersed SPDC. This implies that for a virtual state lifetime of 1 fs, lossless dispersion compensation or a dispersion-free setup would at most improve our E2PA rate by a factor of 95. If the virtual state lifetime is longer, the factor is smaller as indicated in Fig. 3.4(b). This probabilistic analysis of the entanglement time's effect on the rate of E2PA ignores quantum interference effects predicted by more sophisticated theoretical models [6, 32, 33, 31]. The work on these models is ongoing and needs more thorough study. However, as mentioned in Chapter 2, Section 2.3, the interference effects are likely washed out for the absorbers studied in this thesis.

It is worth noting that we could reduce the T_e of our source by reducing the SPDC bandwidth with a bandpass filter that is narrower than the $\approx$ 76 nm width. This would consequently reduce our photon flux. We do not try this for the fluorescence experiment as it seems unlikely that a decreased photon flux will increase our likelihood of measuring E2PA. However, for the transmittance experiments this is a useful strategy since we do not and cannot use our maximum SPDC flux. We find that the T_e values under these conditions are much smaller.

3.8 Characterizing Second-Order Coherence

To measure $g^{(2)}(0)$ we must use our single-mode detection stage (Fig. 3.1). The characterization done here considers the low flux single-mode of photon pairs detected in the transmittance experiment presented in Chapter 6. For this section we look back at the parameter $\gamma^{(2)}_{\text{click}}$ written out in Eq. 1.28 in terms of parameters measurable in our setup. First we show that $\gamma^{(2)}[0] \approx g^{(2)}[0]$.

The parameter $g^{(2)}[0]$ can be written out in terms of the per pulse photon probabilities of the measured source of photons [9], where $P(n)$ is the probability that the source emits n photons,

$$\begin{aligned} g^{(2)}[0] &= \frac{\sum_{n=0}^{\infty} n(n-1)P(n)}{\left[\sum_{n=0}^{\infty} nP(n)\right]^2} \\ &= \frac{2P(2) + 6P(3) + 12P(4) + ...}{\left[P(1) + 2P(2) + 3P(3) + ...\right]^2}. \end{aligned} \tag{3.5}$$

For our pair source, there is no chance for emission of odd numbers of photons so $P(1) = P(3) = 0$ along with the even higher order photon numbers. We operate in a low flux regime where $P(2) >> P(4) >> P(6)$, thus we only keep $P(2)$ and arrive at

$$g^{(2)}[0] \approx \frac{2P(2)}{(2P(2))^2} = \frac{1}{2P(2)}. \tag{3.6}$$

Similarly $\gamma^{(2)}_{\text{click}}[0]$ can be written out in terms of per pulse photon probabilities [9],

$$\gamma^{(2)}_{\text{click}}[0] = \frac{\eta_1\eta_2|\mathcal{R}|^2|\mathcal{T}|^2\left[2P(2) + 6P(3)(1 - \frac{1}{2}\eta_1|\mathcal{R}|^2 - \frac{1}{2}\eta_2|\mathcal{T}|^2) + ...\right]}{\eta_1|\mathcal{R}|^2\left[P(1) + 2P(2)(1 - \frac{1}{2}\eta_1|\mathcal{R}|^2) + ...\right]\eta_2|\mathcal{T}|^2\left[P(1) + 2P(2)(1 - \frac{1}{2}\eta_2|\mathcal{T}|^2) + ...\right]}, \tag{3.7}$$

where $\mathcal{R}$ and $\mathcal{T}$ are the reflection and transmittance efficiencies of the beamsplitter in the single-mode detection stage and η_1 and η_2 are the detection efficiencies for detectors 1 and 2. Again keeping only the $P(2)$ terms,

$$\gamma^{(2)}_{\text{click}}[0] \approx \frac{2P(2)}{4P(2)^2(1-\frac{1}{2}\eta_1|\mathcal{R}|^2)(1-\frac{1}{2}\eta_2|\mathcal{T}|^2)}. \tag{3.8}$$

Next we assume $\frac{1}{2}\eta_1|\mathcal{R}|^2 << 1$ and $\frac{1}{2}\eta_2|\mathcal{T}| << 1$, which is true in our case, and arrive at

$$\gamma^{(2)}_{\text{click}}[0] \approx \frac{1}{2P(2)} \approx g^{(2)}[0]. \tag{3.9}$$

Looking back at Eq. 1.28, we measure the quantities R_1, R_2 and $N_c[0]$. We use a pump laser with repetition time, $T_{\text{rep}} = 12.5$ ns and an integration time of 1 s. Typical values of R_1,R_2 and $N_c[0]$ are 1×10^5 cnt s^{-1}, 1×10^5 cnt s^{-1} and 6×10^3 cnt. This gives $\gamma^{(2)}_{\text{click}} = 48$. This value should only be considered accurate for the experiment discussed in Chapter 6. At high flux, such as that used for the fluorescence measurements, $g^{(2)}$ would much smaller (approaching 1) since multiple pairs can be overlapped in the same pulse, rendering the beam's photon statistics similar to the photon statistics of a laser.

3.9 Entanglement Area

Unfortunately, we do not have a direct measurement of entanglement area A_e; we can only estimate a range of values for A_e. The estimate of the lower bound is based on the diffraction limit. We find no evidence that the two photons can be focused to a region significantly smaller than that set by the diffraction limit. It has been shown [70, 71, 43, 42, 41, 38] that entangled photons can be focused to a spot size that is a few-fold smaller, however we neglect these factors here as they have a minor effect in the orders-of-magnitude comparisons we present. Thus, we set the bound using a circular area with radius (r) set by the central wavelength of excitation ($r \approx \lambda$), which is $2.1\,\mu\text{m}^2$. The estimate of the upper bound varies depending on the experiment. For the transmittance experiment we set the upper bound to an elliptical area with diameters set by the measured transverse FWHMs of an 810 nm laser backpropagated through the setup at its focus in the sample. For the fluorescence experiment the diameters are set by the measured transverse FWHMs of the SPDC beam at its focus in the sample.

Chapter 4

An Introduction to Transmittance Measurements for Entangled Two-Photon Absorption

4.1 Publication Note

This chapter is adapted from:

[59] Mikhaylov, A., Parzuchowski, K.M., Mazurek, M.D., Lum, D.J., Gerrits, T., Camp Jr, C.H., Stevens, M.J. and Jimenez, R., 2020, February. A comprehensive experimental system for measuring molecular two-photon absorption using an ultrafast entangled photon pair excitation source. In *Advanced Optical Techniques for Quantum Information, Sensing, and Metrology* (Vol. 11295, pp. 48-61). SPIE.

4.2 Introduction

In this chapter, we study entangled two-photon absorption (E2PA) using a transmittance-based scheme. We are motivated by the previous experimental works in literature that report E2PA signals using simple transmittance measurement schemes such as that shown in Fig. 2.2. We reiterate (Chapter 2 Section 2.6) that these previous publications only verified one signature of E2PA, the linear dependence of the signal on photon flux, which is not unique to E2PA. This signature is consistent with many one-photon losses such as scattering, one-photon absorption, fluorescence from an optical component or misalignment.

We design our experiment with the goal of reproducing the results from literature and improving on the simple design. Our design has the capability to test for a unique signature of E2PA:

it's dependence on the time delay between photons in a pair (Chapter 2 Section 2.6). We introduce control over the time delay using a Mach-Zehnder interferometer. We find that the interferometer allows us to distinguish E2PA from one-photon losses, but it requires careful consideration of the one-photon losses.

Our two photon absorbing sample is Zinc-tetraphenylporphyrin (ZnTPP) dissolved in toluene. ZnTPP is a commercially available compound for which E2PA cross section σ_E values have been reported [53, 49]. It has been suggested that the value of $\sigma_E = 2.37 \times 10^{-17}$ cm^2 for ZnTPP at 800 nm can be used as a reference standard for E2PA experiments [72], thus it's an important sample to study.

We first analyze our data using a simple method that doesn't use the time-delayed data. This technique is sensitive to one-photon losses and two-photon absorption. The derived changes in transmittance can erroneously be used to derive an σ_E close to the values reported in literature. When we switch to an analysis technique that uses the time-delayed data that is only sensitive to two-photon absorption (2PA), we find that the changes in transmittance for ZnTPP are below are measurement sensitivity of 1%. Using this sensitivity we set an upper bound on the cross section, σ_E^{UB}, for ZnTPP of 1.7×10^{-19} cm^2. This is considerably lower than what has been reported. We believe our measurement technique and analysis form a basis for conducting E2PA experiments in a more quantitative manner.

4.3 Experimental Setup

A schematic illustration of the experimental setup is presented in Fig. 4.1. Here we give a brief overview of the setup, a thorough description of the components is given in Appendix C. It consists of an SPDC pair source, an interferometer, a sample telescope and a single-mode detection stage. The SPDC source is as described in Chapter 3 Section 3.1. We use a bandpass filter to filter the SPDC bandwidth to ≈ 9 nm.

The collimated SPDC beam is steered into a Mach-Zehnder interferometer. A half-wave plate (HWP1) is set at the interferometer's input to rotate the SPDC beam polarization such that the

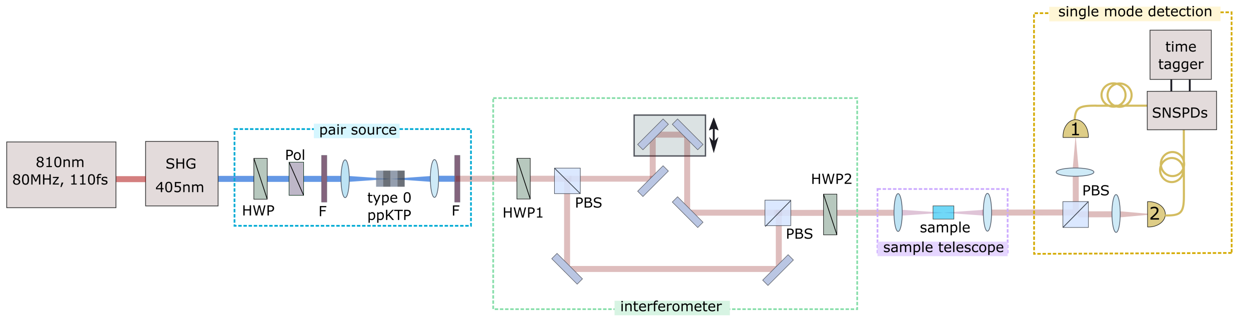

Figure 4.1: Schematic of the experimental setup. The 810 nm laser (dark red) is frequency doubled at an SHG unit. The 405 nm beam (blue) is directed through a half-wave plate (HWP) and polarizer (pol) to control the power. Any remaining 810 nm light is rejected with a set of filters and two dichroic mirrors (F). The beam is focused into a type-0 ppKTP crystal to generate collinear degenerate SPDC at 810 nm (light red). The SPDC is collimated and the 405 nm pump is blocked with a set of filters and two dichroic mirrors (F). HWP1 rotates the SPDC polarization for equal probabilistic splitting at a polarizing beamsplitter (PBS). The beams are directed through either the stationary or delay arm of the interferometer. A retroreflector on a translation stage is used for time delay control in the delay arm. The beams are recombined at a PBS and focused into a cuvette. The beam is collimated and directed into the single mode detection stage which consists of HWP2 and a PBS to switch between detection modes.

photons are split probabilistically and equally at a polarizing beamsplitter (PBS). A retroreflector is set on a motorized translation stage to adjust the length of the delay arm of the interferometer. The beams traveling through the two arms are recombined at a PBS.

The SPDC is focused with a 50 mm lens into a cuvette that contains either a solvent or a solution of two-photon absorbing molecules dissolved in the solvent (sample). A 50 mm lens collimates the light and the beam is sent into the single-mode detection stage described in Chapter 3 Section 3.5. Next, HWP2 and a PBS are used to switch between two detection modes: the alignment mode (HWP2 at 22.5°) and the E2PA measurement mode (HWP2 at 0°). In the measurement mode, the polarization of the photons is not rotated at HWP2 and nearly all the light from the stationary arm goes to detector 1 and nearly all the light from the delay arm goes to detector 2. In the alignment mode, the polarization of the photons is rotated 45° such that the light from each arm has a nearly equal probability of going to either detector.

The sample preparation is done at described in Appendix B. We use the reported molar extinction coefficient [73] of ZnTPP to prepare a sample of 1.0×10^{-4} mol L^{-1} ZnTPP in toluene. A standard 1 cm spectroscopic quartz cuvette is used for all measurements.

4.4 Experimental Characterization

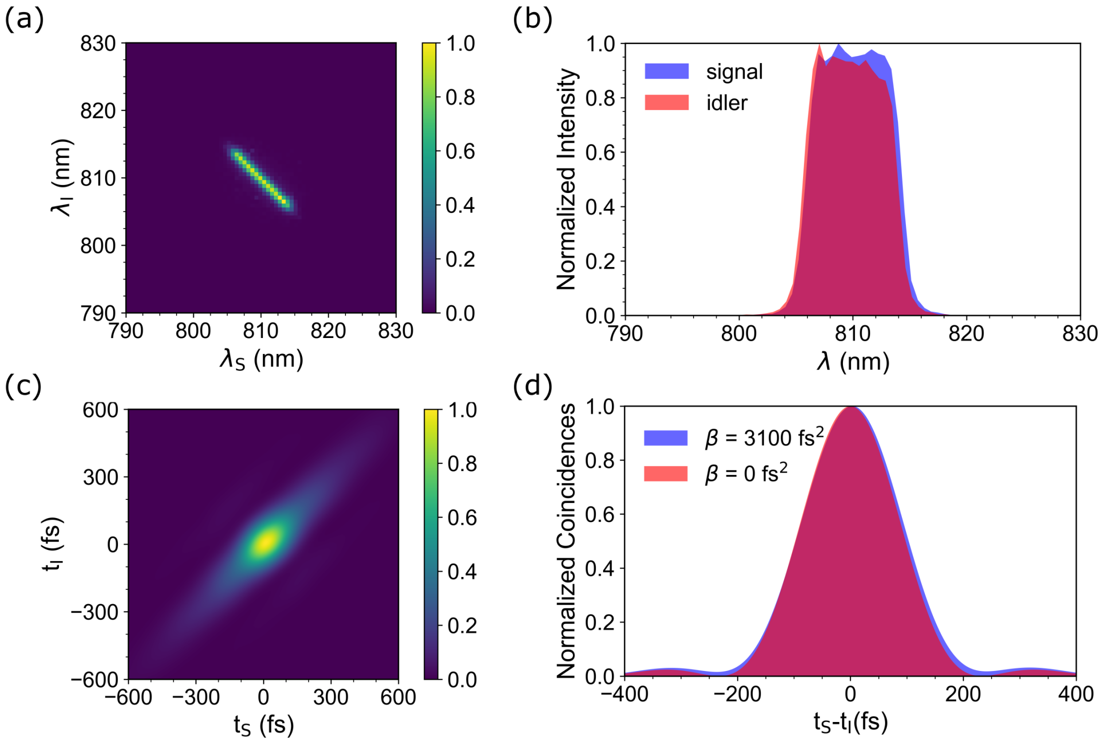

Figure 4.2: (a) Measured joint spectral intensity (JSI) where $\lambda_{\mathrm{S,I}}$ are the signal and idler wavelengths. (b) The JSI is projected onto the horizontal axis and vertical axis showing the signal (blue) and idler (red) spectra respectively. The FWHM of the signal and idler spectra are both 8.7 nm, which is set by an optical filter. The overlap of the spectra is evident in the dark red region. (c) Calculated joint temporal intensity (JTI) obtained through a discrete Fourier transform. (d) Projection onto the antidiagonal axis, t_{S}-t_{I}, of the JTI shown in (c) (blue) and for a transform-limited ($\beta = 0\,\mathrm{fs}^2$) pulse (red). The FWHM of these projections are 213 fs and 208 fs.

We measure the joint spectral intensity (JSI) of our source using the time-of-fight spectrometer described in Chapter 3 Section 3.6. The JSI is shown in Fig. 4.2(a). The bandwidth is set by a bandpass filter placed after the SPDC source. The JSI projections onto vertical and horizontal axes in Fig.4.2(b) are used to estimate the marginal FWHM bandwidths of the photons as 8.7 nm.

We estimate the total group delay dispersion (GDD) of our optical elements between the ppKTP crystal and the center of the sample to be approximately 3100 fs^2 at 810 nm. We use this GDD to simulate the joint temporal intensity (JTI) using the procedure described in Chapter 3 Section 3.7. The result is shown in Fig. 4.2(c). The FWHM of the projection of the JTI onto the antidiagonal axis (Fig. 4.2(d)) is used to estimate the entanglement time as 213 fs. We note that this size of GDD has a nearly negligible effect on our entanglement time due to the narrow bandwidth of our filtered SPDC. The pulse duration of the SPDC can be estimated by the projection of the JTI onto the horizontal and vertical axes, which is ≈ 258 fs.

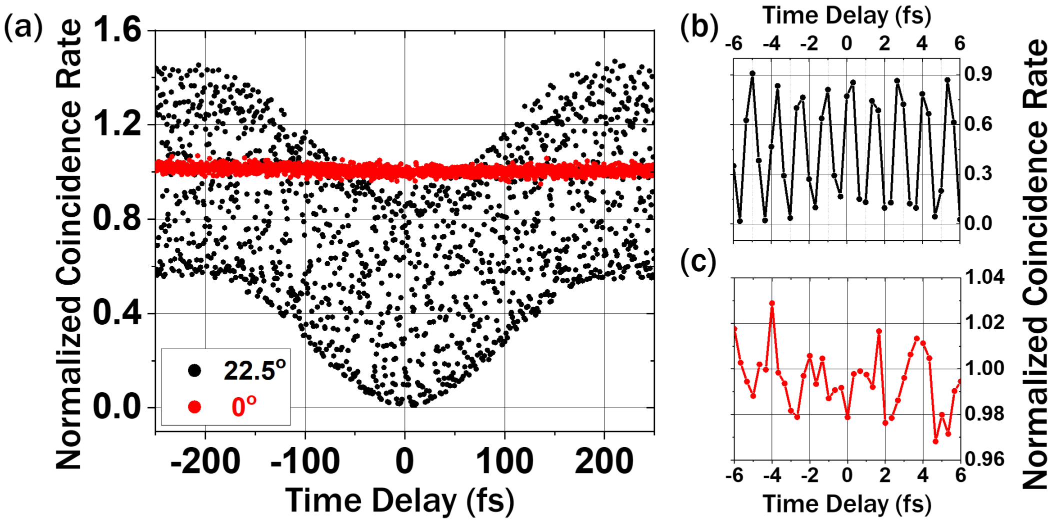

Figure 4.3: (a) The normalized coincidence rate as a function of time delay measured with toluene in the beam path for the alignment mode (black symbols) and E2PA measurement mode (red symbols) configurations over a 500 fs delay range. (b-c) A 12 fs delay range of plot (a) centered at zero delay for the alignment mode (b) and E2PA measurement mode (c). In (b) we observe interference fringes whereas in (c) we observe low amplitude oscillations due to residual interference. The rates are normalized to have average values close to 1 at large delay positions.

In the alignment mode configuration, interference occurs at the PBS in the single-mode detection stage and can be measured in the coincidence rate between detectors 1 and 2. We plot the alignment mode rate in black in Fig. 4.3(a) and (b). The pattern shows a dip as a function of time delay that's at a minimum ("zero delay") at optimal overlap due to Hong-Ou-Mandel

(HOM) interference. Fast-oscillating fringes are superimposed on the HOM dip due to NOON-type interference. We explain the interference pattern in the next section. We measure a fringe visibility of ≈ 90%, which implies that the photons have a high overlap in all degrees of freedom (spatial, spectral, temporal and polarization mode) and thus are indistinguishable. In the E2PA measurement mode, interference is suppressed as shown in red in Fig. 4.3(a) and (c). Due to imperfections of our polarization optics, a small amount of light from the stationary arm leaks to detector 2 and similarly from the delay arm to detector 1. This results in low amplitude residual interference near zero delay.

4.5 Origin of Alignment-Mode Interference Pattern

When characterizing our setup in alignment mode, we measure the interferogram shown in Fig. 4.3(a). Here we explain the structure of this interference pattern.

We begin by modeling the state of each photon pair produced in the SPDC crystal as (see, e.g., Ref. [74] for details):

$$|\psi\rangle = \iint d\omega_1 d\omega_2 f(\omega_1, \omega_2) \hat{a}^\dagger_{\mathrm{H},1} \hat{a}^\dagger_{\mathrm{H},2} |0\rangle \,, \tag{4.1}$$

where the operator $\hat{a}^\dagger_{\mathrm{H},i}$ is the creation operator that creates a horizontally-polarized photon with frequency ω_i. The function $f(\omega_1, \omega_2)$ defines the joint spectral amplitude (JSA) of the photon pair. Because we are modeling light from a type-0 down-conversion process, we must ensure that the JSA is symmetric, i.e. it must obey the relation $f(\omega_1, \omega_2) = f(\omega_2, \omega_1)$.

To calculate the coincidence rate at the interferometer output as a function of time delay, we first consider how light is transformed as it propagates through the interferometer. First, the light travels through HWP1, which is set to an angle of 22.5°, which rotates horizontally polarized light (indicated by subscript ‘H’) to diagonally polarized light. We represent this rotation with the following transformation:

$$\hat{a}^\dagger_{\mathrm{H},j} \rightarrow \frac{1}{\sqrt{2}} \left(\hat{a}^\dagger_{\mathrm{H},j} + \hat{a}^\dagger_{\mathrm{V},j} \right) , \tag{4.2}$$

where $j \in \{1,2\}$, and the 'V' subscript indicates vertical polarization. The light then enters the interferometer, where the vertically-polarized component of the beam travels a fixed path length, and the horizontally-polarized component is delayed by time τ, which is represented by multiplying the $\hat{a}_{\mathrm{H,j}}$ operators by the phase term $\exp\{-i\omega_j\tau\}$. The light is recombined at a PBS, then travels through HWP2, which is also set to an angle of 22.5°. The horizontally polarized component of the light is transformed according to Eq. (4.2), and the vertically polarized component undergoes the transformation:

$$\hat{a}^{\dagger}_{\mathrm{V},j} \rightarrow \frac{1}{\sqrt{2}}\left(\hat{a}^{\dagger}_{\mathrm{H},j} - \hat{a}^{\dagger}_{\mathrm{V},j}\right). \tag{4.3}$$

Finally, the light is split at a PBS, where the vertical component travels to detector 1 and the horizontal component travels to detector 2. The total transformation the light undergoes from the crystal through the last HWP can be summarized as:

$$\hat{a}^{\dagger}_{\mathrm{H},j} \rightarrow \frac{1}{2}\left[\hat{a}^{\dagger}_{\mathrm{H},j}\left(e^{-i\omega_j\tau}+1\right) + \hat{a}^{\dagger}_{\mathrm{V},j}\left(e^{-i\omega_j\tau}-1\right)\right]. \tag{4.4}$$

To calculate the coincidence rate, $R(\tau)$, between detectors D1 and D2, we apply the transformation (4.4) to the SPDC state (4.1), and then find the magnitude of the terms that lead to coincidences. The result is:

$$R(\tau) \propto \iint d\omega_1 d\omega_2 \left|f(\omega_1,\omega_2)\right|^2 \left|e^{-i\omega_1\tau}+1\right|^2 \left|e^{-i\omega_2\tau}-1\right|^2, \tag{4.5}$$

which we can can separate into two terms:

$$R = R^{\mathrm{HOM}}(\tau) + R^{\mathrm{NOON}}(\tau), \tag{4.6}$$

with

$$R^{\mathrm{HOM}}(\tau) = 2\iint d\omega_1 d\omega_2 \left|f(\omega_1,\omega_2)\right|^2 \left[1-\cos(\omega_1-\omega_2)\tau\right], \tag{4.7}$$

and

$$R^{\mathrm{NOON}}(\tau) = 2\iint d\omega_1 d\omega_2 \left|f(\omega_1,\omega_2)\right|^2 \left[1+2\cos\omega_1\tau-2\cos\omega_2\tau-\cos(\omega_1+\omega_2)\tau\right]. \tag{4.8}$$

The first term, R^{HOM}, leads to a coincidence rate that is constant for large time delays, and decreases to zero at delay $\tau = 0$; this is HOM interference [75]. The second term, R^{NOON}, describes a NOON-type interferogram with fringes that oscillate at the sum of the two photon frequencies [76].

We complete the calculation by choosing a specific form of the JSA and evaluating the integrals in Eqs. (4.7) and (4.8). For simplicity, we assume the pump laser has a Gaussian spectrum with center frequency $2\omega_0$ and width σ_p. We also assume the SPDC process is degenerate and that the photons have Gaussian spectra with width σ. We write the JSA as:

$$f(\omega_1, \omega_2) = \frac{(2\sigma^2 + \sigma_p^2)^{1/4}}{(2\pi\sigma^2\sigma_p)^{1/2}} \exp\left\{-\frac{(\omega_1 - \omega_0)^2}{4\sigma^2} - \frac{(\omega_2 - \omega_0)^2}{4\sigma^2} - \frac{(\omega_1 + \omega_2 - 2\omega_0)^2}{4\sigma_p^2}\right\}. \tag{4.9}$$

The resulting coincidence rates are:

$$R^{\mathrm{HOM}}(\tau) = \frac{1}{2}\left(1 - \exp\left\{-\sigma^2\tau^2\right\}\right), \tag{4.10}$$

and

$$R^{\mathrm{NOON}}(\tau) = \frac{1}{2}\left(1 - \exp\left\{-\frac{\sigma^2\sigma_p^2\tau^2}{2\sigma^2 + \sigma_p^2}\right\}\cos 2\omega_0\tau\right). \tag{4.11}$$

The explicit form of Eqs. (4.10) and (4.11) demonstrates the HOM-type and NOON-type components of the interferogram.

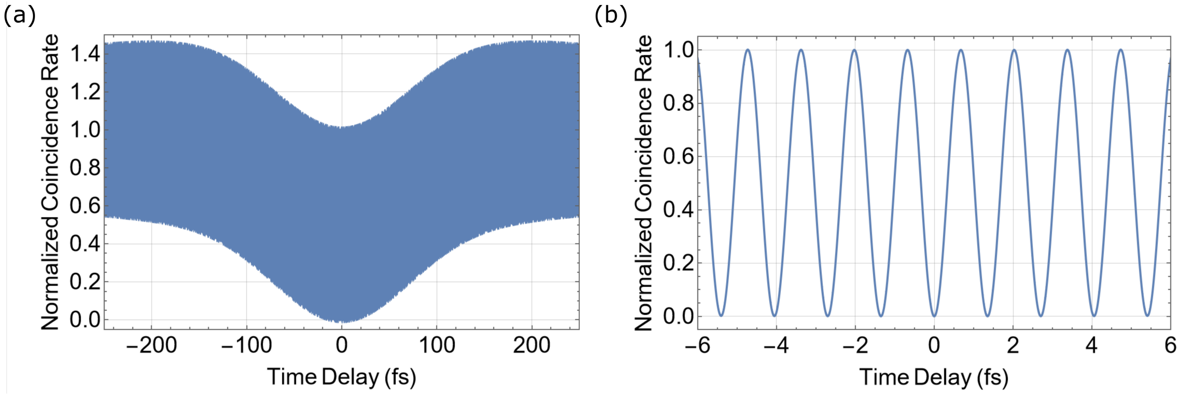

Figure 4.4: Calculated coincidence rate as a function of interferometer time delay. (a) A 500 fs range of the interferogram composed of fast-oscillating fringes superimposed on a HOM-type dip. (b) A 12 fs range of the same graph to show the fringes, the period of ≈ 1.35 fs is consistent with a pump wavelength of 405 nm.

We can plot $R(\tau) = R^{\mathrm{HOM}}(\tau) + R^{\mathrm{NOON}}(\tau)$ if we choose specific parameters for the JSA, which we display in Fig. 4.4. For the pump we choose $\sigma_p = 0.002\,\mathrm{fs}^{-1}$ and a center wavelength of

405 nm, which corresponds to a full width at half maximum (FWHM) of ≈ 0.2 nm. We choose a center wavelength of 810 nm for the down-conversion, and $\sigma = 0.01\,\mathrm{fs}^{-1}$, which corresponds to a single-photon spectrum with ≈ 6 nm bandwidth. With these parameters, the calculated coincidence rate $R(\tau)$ qualitatively approximates the measured interferogram in Fig. 4.3.

4.6 Experimental Procedures

After verifying the alignment of the setup, we rotate HWP2 to 0° to operate in the E2PA measurement mode. Ideally, we would completely turn off any interference and measure zero interference visibility, with the only observed change in coincidences as a function of time delay due to E2PA. However, we measure residual interference. This artifact (linear interference fringes superimposed on a possibly small remaining HOM dip) could be incorrectly attributed to E2PA. To mitigate the effect of the residual interference, we record the coincidence rates over several fringes in the vicinity of zero delay and average them. This averaging procedure is repeated for a delay of approximately -6.7 ps, corresponding to a path-length difference of 2 mm from zero delay; we denote this position as "τ delay". The uncertainty is estimated from the standard deviations in the measured counts and is $\approx 1\%$. This defines the sensitivity limit in measuring changes in the coincidence rates.

For the E2PA measurements we tune the 405 nm pump power from $\approx 60\,\mu$W to 11 mW using the HWP; the coincidence rates are approximately $2 \times 10^2 - 3.7 \times 10^4$ cnt s^{-1} and singles rates are $10^3 - 10^6$ cnt s^{-1}. Measured coincidence rates are shown in Fig. 4.5 and given in Appendix D. We record the coincidence rates for photon pairs transmitted through the solvent (blue symbols) and subsequently through the sample (red symbols) at τ (a) and zero delays (b). All measurements are repeated multiple times, from which standard deviations (relative) are estimated. Sample removal and refill is done using a pipette and the cuvette is fixed in the beam path.

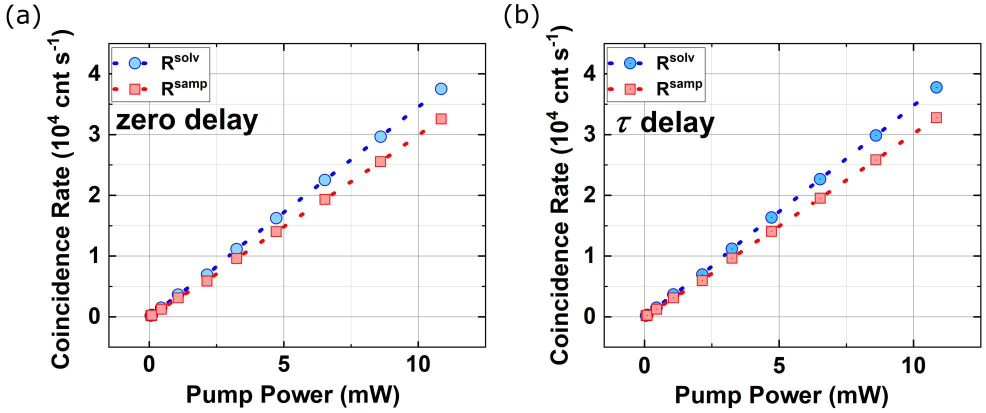

Figure 4.5: Coincidence rates measured in the experiment. The rates (in counts per second, cnt s^{-1}) are measured as a function of the pump power (mW). The experiments were conducted for neat solvent (blue symbols) and sample (red symbols) at the (a) zero- and (b) τ-delay positions. All rates were averaged according to the procedure described in Section 4.6.

4.7 Deriving a Cross Section

In this section, we describe how a measured change in transmittance due to E2PA can be used to estimate an E2PA cross section.

Consider a beam of photon pairs that is described by a flux ϕ. We can derive an expression describing how ϕ changes while the beam propagates along the z-axis through a sample. The beam enters the sample at $z = 0$. The sample's length is L. Assuming the beam experiences only linear losses while interacting with the sample that causes some attenuation in the flux characterized by κ, the change in the flux $d\phi$ over some small distance dz can be written

$$\frac{d\phi}{dz} = -\phi\kappa. \tag{4.12}$$

We make the approximation that the beam is collimated over the length L (Rayleigh range $\gg L$) and has constant intensity over its cross section. For our experimental conditions this is not precise (the SPDC beam is not uniform and is focused into the sample); however, we ignore this discrepancy and proceed with the simplest case. A more rigorous analysis (similar to what has been developed for z-scan type measurements [15]) should be applied for a general treatment. With the aforementioned assumptions integration of Eq. (4.12) becomes trivial. Assuming weak absorption ($\kappa L \ll 1$), we find,

$$\phi_{\text{out}} \simeq \phi_{\text{in}} \left(1 - \kappa L\right). \tag{4.13}$$

We can introduce a relative change in the flux, $\delta\phi$, as

$$\delta\phi = \frac{\Delta\phi}{\phi_{\text{in}}}. \tag{4.14}$$

where $\Delta\phi = \phi_{\text{in}} - \phi_{\text{out}}$ and $\phi_{\text{in(out)}}$ is the flux going into (out of) the sample. Using Eq. (4.13), this becomes

$$\delta\phi \simeq \frac{\phi_{\text{in}} - \phi_{\text{in}} \left(1 - \kappa L\right)}{\phi_{\text{in}}} = \kappa L. \tag{4.15}$$

All of our experimental data is recorded as detected photon pair rates, R, rather than flux values. Therefore, it is convenient to rewrite the equations in a slightly different way using R instead of ϕ. Since ϕ differs from R only by a factor of $1/A$ where A is the beam area, it is straightforward to show that,

$$\delta\phi = \delta R = \frac{\Delta R}{R_{\text{in}}} \approx \kappa L, \tag{4.16}$$

where $\Delta R = R_{\text{in}} - R_{\text{out}}$ and $R_{\text{in(out)}}$ is the photon rate going into (out of) the sample. Since we fiber couple the light transmitted through the sample before it is detected, A is specific to the spatial mode coupled into fiber.

If the change in transmittance ($\delta\phi$ or equivalently δR) is due to E2PA only, then $\kappa = n\sigma_E$, where n is the number density of the sample (in molecules per cm^3).

Then we find,

$$\sigma_E \simeq \frac{\delta R}{nL}, \tag{4.17}$$

where σ_E and L are in units of cm^2 molecule^{-1} and cm, respectively.

4.8 Data Analysis Case Studies

In this section we show how the measured coincidence rates are used to calculate a δR that is only sensitive to E2PA rather than one-photon losses. We start with the most simplistic approach adopted from previous reports (i.e. Refs. [53, 49]) and discuss the pitfalls of this method. We progressively add more complexity to show how our experimental setup and analysis can be used to account for one-photon loss mechanisms.

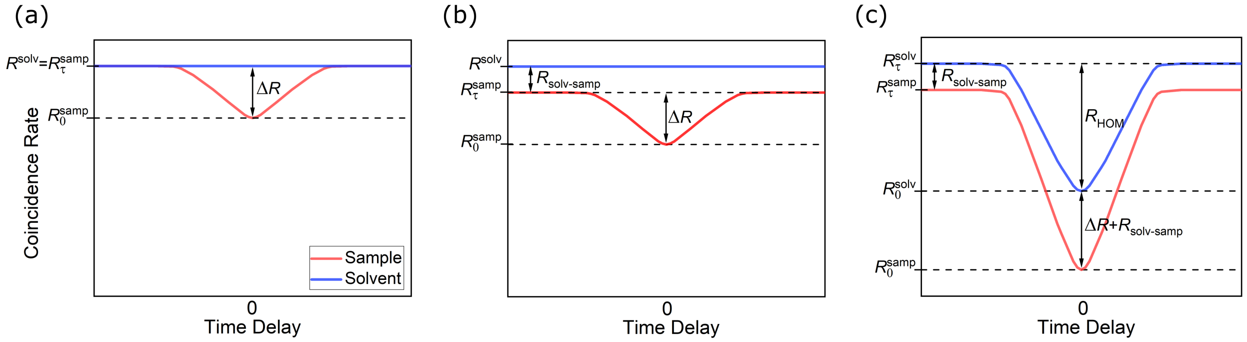

Figure 4.6: A schematic showing notations used in the data analysis case studies. Each panel corresponds to a different case considered in Section 4.8: (a) illustrates case 1, (b) illustrates case 2 and (c) illustrates case 3.

4.8.1 Case 1. Measuring sample and solvent without time delay

Here we start by using only data at zero delay. We assume that if there is a difference in coincidence rates measured with the solvent (R_0^{solv}) and with the sample (R_0^{samp}) (at zero delay), it's due to E2PA. This situation is schematically depicted in Fig. 4.6(a). It shows coincidence rates as a function of the time delay. All curves are not real data and not shown to scale. Under this assumption, $\Delta R = R_0^{\text{solv}} - R_0^{\text{samp}}$.

From Section 4.7, Eq. (4.16)

$$\delta R = \frac{\Delta R}{R_{\text{in}}} \simeq \frac{R_0^{\text{solv}} - R_0^{\text{samp}}}{R_0^{\text{solv}}}.$$

We use the rates measured at different pump powers (Table D.1 in Appendix D) to calculate average δR values. We find $\delta R = 0.146 \pm 0.010$. This assumption ignores the likely scenario that switching a solvent with a sample can introduce one-photon losses to the measurement. These losses could be one-photon absorption, scattering or misalignment. In section 4.9, we will see that this way of analyzing the data leads to an overestimate of σ_E values.

4.8.2 Case 2. Measuring sample with time delay

Next consider a case where only the sample is measured and the time delay is varied between the zero- and τ-delay positions. Here we assume that the difference in the coincidence rates measured at τ and zero delays, R_{τ}^{samp} and R_{0}^{samp}, respectively, is proportional to E2PA. This scenario is depicted in Fig. 4.6(b). Under these assumptions, $\Delta R = R_{\tau}^{\text{samp}} - R_{0}^{\text{samp}}$ and

$$\delta R = \frac{\Delta R}{R_{\text{in}}} \simeq \frac{R_{\tau}^{\text{samp}} - R_{0}^{\text{samp}}}{R_{\tau}^{\text{samp}}}$$

This technique avoids some of the pitfalls that render case 1 incorrect since the one-photon losses that are associated with switching the sample with a solvent are not introduced. Those losses are shown in Fig. 4.6(b) as $R_{\text{solv}-\text{samp}}$.

From the measured rates we deduce $\delta R = 0.006 \pm 0.005$. The first two lowest power points (lowest rates in Table D.1) are excluded from the calculation. Including these removed points results in a large additional uncertainty in δR. One can see that in this case, the value of δR is much smaller than in case 1. This is because the largest one-photon losses contributing to the δR derived in case 1 are removed in case 2. However, case 2 can only derive accurate δR values when the one-photon losses in the experiment are the same at zero and τ delays. This assumption is not correct, especially since we noted that there are residual interference effects evident at zero delay. However, the delay-dependent one-photon losses are smaller or of similar magnitude to our experimental uncertainty as shown by the derived δR. In the next case study, we account for all one-photon losses including the residual interference.

4.8.3 Case 3. Measuring sample and solvent with time delay

Here we account for all the one-photon losses by using both the sample and solvent measurements at both time delays. We assume that the residual interference effects are the same magnitude for sample and solvent measurements. We denote the loss in the coincidence rate associated with residual interference at zero delay as R_{HOM}. Additionally, if there is some misalignment associated with replacing solvent with sample or due to moving the stage between the two delay positions, the corresponding losses in the coincidence rates are $R_{\text{solv}-\text{samp}}$ and R_{stage}, respectively. A schematic describing this case is shown in Fig. 4.6(c), however R_{stage} is not shown.

In this case, the coincidence rates measured with the sample at the two delay positions are

$$R_\tau^{\text{samp}} = R_{\text{in}} - R_{\text{solv}-\text{samp}} - R_{\text{stage}},$$

$$R_0^{\text{samp}} = R_{\text{in}} - \Delta R - R_{\text{HOM}} - R_{\text{solv}-\text{samp}},$$

and for the solvent,

$$R_\tau^{\text{solv}} = R_{\text{in}} - R_{\text{stage}},$$

$$R_0^{\text{solv}} = R_{\text{in}} - R_{\text{HOM}}.$$

Using these relations one can show

$$\Delta R = (R_\tau^{\text{samp}} - R_0^{\text{samp}}) - \left(R_\tau^{\text{solv}} - R_0^{\text{solv}}\right).$$

Here, $R_{\text{in}} \simeq R_0^{\text{solv}}$. Then,

$$\delta R \simeq \frac{\Delta R}{R_0^{\text{solv}}} = \frac{(R_\tau^{\text{samp}} - R_0^{\text{samp}}) - \left(R_\tau^{\text{solv}} - R_0^{\text{solv}}\right)}{R_0^{\text{solv}}}.$$

Thus, δR is independent of $R_{\text{solv}-\text{samp}}$, R_{HOM} and R_{stage}. Using this analysis, $\delta R = -0.001 \pm 0.004$. Again, we excluded the lowest power points from the analysis to reduce the calculated uncertainty. The average δR value is lower than the associated uncertainty, thus, we cannot assign this change in transmittance to a measured signal in our experiment.

4.9 Results

Here we estimate σ_E values using Eq. (4.17). The derived σ_E values are listed in Table 4.1. First we consider case 1 where we found $\delta R = 0.146 \pm 0.010$. We can use this value to derive $\sigma_E = (2.43 \pm 0.20) \times 10^{-18}$ cm^2, however this change in transmittance may be due to one-photon losses as discussed in Section 4.8.1. It's useful to note that this σ_E value is within the range of σ_E values for ZnTPP from other reports where a very similar analysis procedure was used: $\sigma_E = 2.37 \times 10^{-17}$ cm^2 as reported in Ref. [53] and $(1 - 10) \times 10^{-18}$ cm^2 as reported in Ref. [49].

For cases 2 and 3 we found $\delta R = 0.006 \pm 0.005$ and $\delta R = -0.001 \pm 0.004$, respectively. These δR are effectively zero within the estimated uncertainty. Therefore, we did not use them to calculate the corresponding σ_E values.

Let us consider a limiting case to estimate our experimental upper bound on σ_E. We call this situation case 4 (Table 4.1). The smallest δR that can be measured reliably in our experiment is about 0.01. Thus, we calculate from Eq. (4.17): $\sigma_E^{\mathrm{UB}} \approx 1.7 \times 10^{-19}$ cm^2, which serves as an upper bound for ZnTPP.

Table 4.1: Summary of the changes in transmittance δR and calculated σ_E values for ZnTPP. Cases 1-3 correspond to the 3 different analysis case studies, with case 3 illustrating the correct analysis procedure. Case 4 illustrates a limiting situation used to place an upper bound on σ_E.

Case	δR	$\sigma_E \times 10^{19}$ cm^2
1	0.146 ± 0.010	24.3 ± 1.6
2	0.006 ± 0.005	–
3	-0.001 ± 0.004	–
4	0.01	1.7

4.10 Conclusions

In this chapter we presented our vision of a comprehensive transmittance–based scheme for E2PA measurements. We performed a careful characterization of the experimental apparatus, and we showed that the implementation of a time delay between the two photons was essential for a one-photon loss insensitive transmittance measurement.

We used data analysis case studies to highlight the importance of using the time delay. If no time delay is implemented (case 1), then the calculated δR value includes spurious contributions from scattering or other one-photon losses. The value of δR derived in case 2 is inherently free of the measurable losses attributed to case 1, however it may include delay-dependent one-photon losses. To eliminate all one-photon losses we applied the analysis presented in case 3. In cases 2 and 3 the derived δR values are significantly lower than the results obtained in case 1 (Table 4.1).

Thus, simplistic subtraction schemes like those used in case 1 are insufficient and can lead to a many-orders-of-magnitude overestimate in σ_E values.

We illustrated this procedure in our pilot study of ZnTPP using 810 nm SPDC excitation. We showed that if the time delay was not applied, one can erroneously use their measurements to derive a σ_E value that is in agreement with published values in literature. The real changes in transmittance due to E2PA for ZnTPP were below our experimental sensitivity of $\approx 1\%$. Thus, we estimated ZnTPP's $\sigma_E \leq 1.7 \times 10^{-19}$ cm^2, which is significantly lower than previously published σ_E values.

Chapter 5

Bounding Entangled Two-Photon Absorption Cross Sections with a Fluorescence-Based Scheme

5.1 Publication Note

This chapter is adapted from:

[19] Parzuchowski, K.M., Mikhaylov, A., Mazurek, M.D., Wilson, R.N., Lum, D.J., Gerrits, T., Camp Jr, C.H., Stevens, M.J. and Jimenez, R., 2021. Setting bounds on entangled two-photon absorption cross sections in common fluorophores. *Physical Review Applied*, *15*(4), p.044012.

5.2 Introduction

In this chapter, we investigate entangled two-photon absorption (E2PA) using a fluorescence-based measurement scheme. We are motivated to determine whether a large quantum advantage (QA) exists. Some reports suggest the QA is nearly 10 orders of magnitude [52, 54]. However, in these reports it is unclear whether the signals are caused by E2PA or some other process as discussed in Chapter 2 Section 2.5. Furthermore, the methodology in these reports has not advanced to the point where classical two-photon absorption (C2PA) and E2PA can be measured in the same setup, and thus the excitation conditions can differ significantly leading to orders-of-magnitude error in the QA quantification.

We present a method for measuring both entangled two-photon excited fluorescence (E2PEF) and classical two-photon excited fluorescence (C2PEF) in one experimental setup. We characterize our excitation sources, fluorescence collection system and samples to determine our 2PA cross-section sensitivity. The C2PEF measurements are used to derive C2PA cross sections, σ_C, for the six studied fluorophores. The values strongly agree with previously reported C2PA cross sections [17, 47, 77]. Although we do not detect measurable E2PEF signals for any of the six fluorophores, we can bound the maximum efficiency of the E2PA process in each fluorophore by placing upper bounds on its E2PA cross section, σ_E. The C2PEF and E2PEF measurements are also used to bound the QA. Our established upper bounds on σ_E are up to four orders of magnitude lower than the smallest published value of σ_E [48]. For two of the samples, the upper bounds on σ_E are four and five orders of magnitude lower than the previously reported cross sections [48, 47].

5.3 Experimental Setup and Characterization

Here we give a brief overview of our experimental setup and characterizations. A thorough description of the components is given in Appendix E. A schematic of the experimental setup is shown in Fig. 5.1 and it consists of a laser source, a photon pair source, a single-mode detection stage, a multi-mode detection stage and the two-photon excited fluorescence (2PEF) measurement system. A pump laser emits ≈ 110 fs pulses with a center wavelength of 810 nm (≈ 9 nm bandwidth) at a repetition rate of 8×10^7 pulses s^{-1}. The laser output is frequency doubled to produce 405 nm light (≈ 3 nm bandwidth), of which 30 mW is used to produce SPDC for E2PA as described in Chapter 3 Section 3.3. A small fraction of the 810 nm pump laser is routed around the nonlinear crystals and used for C2PA.

We characterize the joint spectrum of the photon pairs with the time-of-flight fiber spectrometer using the single-mode detection stage as described in Chapter 3 Section 3.6. In this configuration, the single-mode detection stage consists of a 50-50 fiber beamsplitter rather than a free-space beamsplitter. The SPDC is approximately degenerate and centered at 810 nm with ≈ 76 nm bandwidth. We determine the entanglement time (Chapter 3 Section 3.7) using the estimated joint temporal intensity, which accounts for the approximately 3700 fs^2 of dispersion accumulated by each photon pair before reaching the center of the cuvette. The value of T_e at the sample position is ≈ 1620 fs. Although T_e is larger than in the ideal (dispersion-free) case, we make

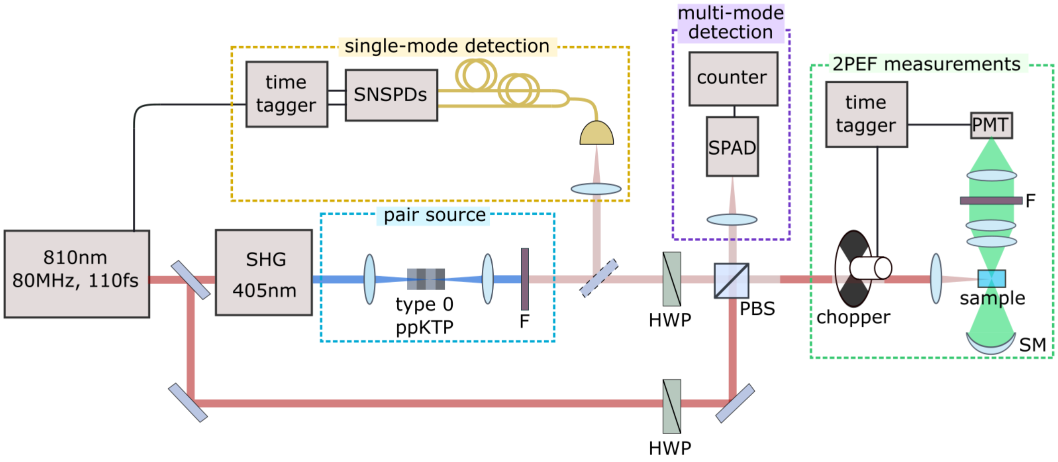

Figure 5.1: Schematic of the experimental setup. The 810 nm laser (dark red) is split into two paths; one path is used for C2PEF measurements and the other for E2PEF measurements. The light in the C2PEF path is directed through a half-wave plate (HWP) and polarizing beamsplitter (PBS) to control the power of light directed to the 2PEF measurement system. The laser is optically chopped (chopper) and focused into a sample. The fluorescence (green) is collected onto a photon-counting PMT and all scattered light rejected using filters (F). The PMT pulses are shaped and sent to a time tagger that is synchronized with the optical chopper. The light in the E2PEF path is frequency doubled (blue) via second-harmonic generation (SHG) and focused into a type-0 ppKTP crystal to generate collinear SPDC photon pairs at 810 nm (light red). Filters (F) are used to remove the remaining 405 nm light. To characterize the joint spectral intensity of the light, a flip mirror directs the pairs into the time-of-flight spectrometer which uses the single-mode detection stage. To characterize the absolute SPDC photon rate at the sample, a HWP and PBS direct the light to a single-photon avalanche diode (SPAD) in the multi-mode detection stage. For E2PEF measurements, the HWP is rotated to transmit all SPDC photons through the PBS; this light travels along the same path as the light used in the C2PEF measurements where it is focused into a 2PA sample.

a probabilistic estimate that lossless dispersion compensation would at most increase the rate of E2PA by a factor of 95 (Chapter 3 Section 3.7).

The SPDC photon rate is measured using the multi-mode detection stage. The optical system was designed to minimize losses, thereby minimizing the number of unpaired photons focused into the sample. Taking into account the single-photon detection rate, the SPAD dead time and efficiency, the photon statistics of the SPDC and the optical losses in our setup from the center of the crystal to the center of the sample ($\approx 24\%$), we estimate that ≈ 147 photons pulse^{-1} are generated at the output of the crystal and ≈ 112 photons pulse^{-1} arrive at the sample while operating at our maximum pump power (30 mW) (Chapter 3 Section 3.4).

We estimate that the value of A_e is in the range of $2.1 - 13,700\,\mu\text{m}^2$ as described in Chapter 3 Section 3.9. The value of A_e likely changes throughout the cuvette because the beam is not collimated. The range of values that A_e could take on at the edge of the cuvette is $2.1 - 2,160,000\,\mu\text{m}^2$. This subtle point is taken into account in Section 5.5.

For C2PEF and E2PEF measurements, we use a polarizing beamsplitter (PBS) to combine the SPDC and laser beams, and align them along the same path. The power of the laser beam is controlled using a half-wave plate (HWP) in conjunction with the PBS, varying from $0.079 - 10.5\,\mu\text{W}$. The beams are sent through an optical chopper, then focused in the center of a cuvette to a beam FWHM of $\approx 68\,\mu\text{m}$ and $\approx 49\,\mu\text{m}$ for the SPDC and laser beams respectively. For E2PEF measurements, we block the laser beam, and for C2PEF measurements we block the SPDC beam. The portion of the beam absorbed in the sample is partially re-emitted as fluorescence, which is collected and focused onto a photon-counting photomultiplier tube (PMT). A combination of a shortpass and bandpass filter (selected for each fluorophore, see Section 5.5) in front of the PMT reject scattered 810 nm and 405 nm light. The SPDC beam is found to have a larger divergence within the sample compared to the laser beam (Section 5.4). The divergence is taken into account by using the characterization of the spatially dependent geometrical collection efficiency (Section 5.5). The geometrical collection efficiency of the fluorescence collection system is characterized using numerical simulations and 1PEF measurements (Section 5.4) and determined to be 15.4% and 4.7% for a point source and line source (extending the length of the cuvette) of fluorescence, respectively. The two beams are found to be displaced from each other in the sample by $\approx 5\,\mu\text{m}$ horizontally and vertically. As Section 5.4 and Appendix F explain, our experimental apparatus is carefully designed and characterized to be robust against small changes in alignment like these. The longitudinal displacement between the beams is compensated for.

The six fluorophores investigated in this study are the 1,3,5-triazine-based octupolar molecule “AF455” [78, 79] in toluene, Qdot ITK carboxyl quantum dot 605 (qdot 605) in borate buffer, fluorescein in pH 11 water, the benzodithiophene derivative “9R-S” [47] in chloroform, rhodamine

590 (Rh6G) in methanol and coumarin 153 (C153) in toluene (details on sample preparation in Appendix B). These samples are of particular interest because of their well-known and large values of σ_C at 810 nm (see Table 5.3). In addition, two of these samples (Rh6G and 9R-S) were studied in previous reports of E2PA [48, 47].

5.4 Fluorescence Collection Efficiency

Initial characterization of the fluorescence system's geometrical collection efficiency is performed using Zemax's OpticStudio. The solvent, glass cuvette walls, four collection optics and detector surface are modeled in the program. Using a merit function and an optimization algorithm, we find the ideal spacing of the optics.

A 2PA process can only occur if two photons are sufficiently spatially overlapped at a fluorophore, thus the rate of C2PA and E2PA depend on the focusing of the respective beams. For C2PA, this is clearly evident through the quadratic photon flux dependence in the excitation rate (Eq. (2.6)), where the photon flux depends inversely on the beam size. For E2PA, this spatial dependence is hidden because the excitation rate depends linearly on photon flux (Eq. (2.10)) in a similar manner to 1PA (a beam-size-independent process). The spatial dependence is instead included in the E2PA cross section (Eq. (2.11)), which depends inversely on the entanglement area.

In our experiment, the excitation beams are not collimated (see divergence of the SPDC (green) and laser (blue) beams in Fig. 5.2(a)) and thus the excitation volume is a non-trivial shape. Furthermore the E2PA beam does not have a constant entanglement area (or E2PA cross section) which complicates the ability to perform an exact calculation of the E2PA cross section (or in our case an upper bound) for a given E2PA signal. To approximate this, we calculate the E2PA cross-section upper bound in the region with nearly constant entanglement area (Section 5.5). For this calculation and our calculation of the C2PA cross section (Section 5.5) it is critical to characterize the collection efficiency of our system as a function of the origin of the fluorescence along the z-direction. Ideally we would also take into account the collection efficiency's x- and y-dependence, however as we discuss below, this is less critical to the final result.

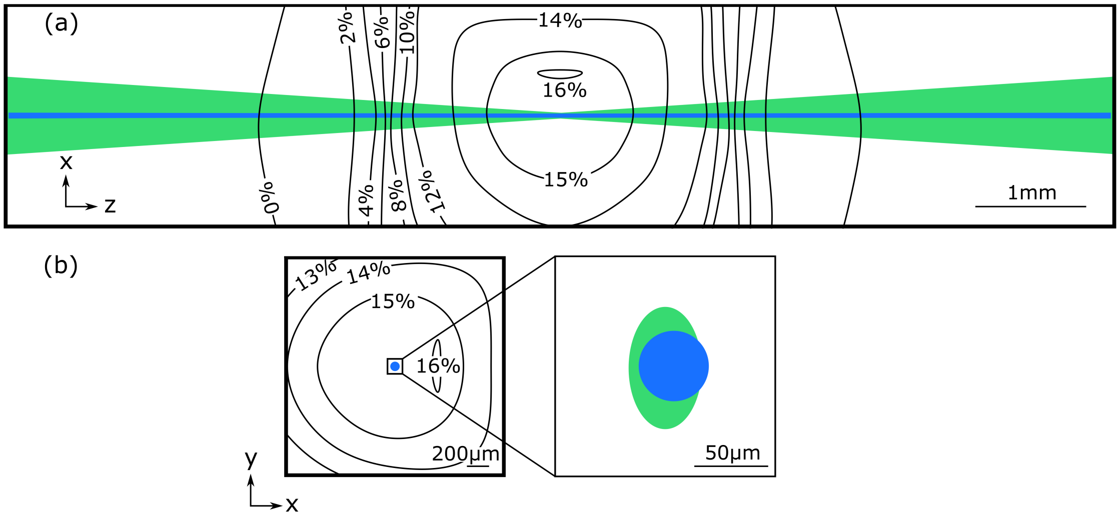

Figure 5.2: Illustration of the geometrical collection efficiency inside of the cuvette and the laser/SPDC beam overlap. (a) A cross section of the cuvette in the xz plane. The selected contours show where the collection efficiency is constant, based on Zemax simulations. The magnitude of the collection efficiency is scaled based on 1PEF measurements. The beam propagation is shown for the laser beam (blue) and the SPDC beam (green). (b) A cross section of the cuvette in the xy plane. The magnified image on the right is a view of the center of the xy plane and shows approximate beam FWHMs and overlap.

In Zemax, we simulate the collection efficiency as a function of the origin of the fluorescence within the cuvette volume. We model a point source of fluorescence that emits rays isotropically at some position in the cuvette. The number of those rays collected onto the detector are counted. We systematically translate this source in all directions to trace out contour plots of collection efficiency in the xz plane (centered in y) (Fig. 5.2(a)) and the xy plane (centered in z) (Fig. 5.2(b)). In Fig. 5.2 we rescale the collection efficiency found through Zemax to match experimental values, as discussed below. We find that the collection efficiency is slightly asymmetric in the x direction, collecting slightly better when the point source is displaced towards the PMT. We ignore this minor asymmetry in the experiment and center the beams through the cuvette.

Although the spatial distributions of the excitation beams have some transverse extent, Fig. 5.2 shows that transverse displacements from $x = y = 0$ must be large to significantly affect the collection efficiency ($> 10^2\,\mu$m at $z = 0$ and transverse displacements nearly negligible beyond

$|z| > 1$ mm). Our excitation beams' spatial distributions in the transverse directions are contained within a region of nearly constant collection efficiency, thus in our calculations (Section 5.5) we ignore the transverse spatial distribution of the excited fluorescence.

In Zemax, we simulate the total collection efficiency (κ) of a particular excitation volume for the limiting cases of a uniform cylindrical excitation volume (50 μm diameter) that extends the length of the cuvette (centered in x and y) and for that of a point source centered in the cuvette. For the former, the collection efficiency is at a minimum for the system (for a uniform excitation volume centered in the cuvette with 50 μm diameter), $\kappa_{\text{min}} = 6.1\%$, and for the latter, the collection efficiency is at a maximum for the system, $\kappa_{\text{max}} = 20.2\%$

To a good approximation, the collection efficiency K (found using Zemax) as a function of z (cm) fits to a complementary error function. This can be qualitatively understood by the similarity of the simulation of the collection efficiency as a function of z to a knife's edge beam profile measurement, which fits the same type of function. In both cases an intensity is measured as a function of the placement of an object. This object alters the intensity passed to a detector. Thus, the collection efficiency as a function of z takes the form

$$K(z) = \frac{\kappa_{\text{max}}}{2} \text{erfc}\left(\alpha(|z| - z_0)\right), \tag{5.1}$$

where $\kappa_{\text{max}} = 0.20$, $\alpha = 2.8\,\text{cm}^{-1}$ and $z_0 = 1.5\,\text{cm}$. These parameters are set by Zemax collection efficiency simulations for the translation of a point source along the z direction (centered in x (cm) and y (cm)), and $z = 0$ is the center of the cuvette. The function $K(z)$ is used to calculate the portions of an excitation volume extended along the z direction that contribute to the collected fluorescence signal. Below we discuss our method to scale the collection efficiency as a function of z, $K(z)^{'}$ (where $^{'}$ indicates the experimental value rather than simulated), to fit the experimental conditions.

We measure the minimum collection efficiency, $\kappa^{'}_{\text{min}}$, of our fluorescence setup using a 1PEF-based technique. The results of this measurement are compared to the Zemax simulation of κ_{min} to scale the collection efficiency for experimental differences. As we mentioned, $\kappa^{'}_{\text{min}}$ characterizes a system with a nearly uniform cylindrical excitation volume (50 μm diameter) that extends the length of the cuvette, thus we use an excitation source which generates an excitation volume of this kind.

In a similar manner to the treatment in Ref. [16], the measured 1PEF rate, F_1 (cnt s^{-1}), can be described by

$$F_1 = N_1 \frac{W}{h\nu} \kappa^{'}_{\mathrm{min}} \int\limits_{\lambda_i}^{\lambda_f} \gamma(\lambda)\Phi(\lambda) d\lambda, \tag{5.2}$$

where N_1 (excitations photon^{-1}) is the number of excitations per photon, W (W) is the average power incident on the sample, $h\nu$ (J) is the average energy of an incident photon, $\lambda_{i,f}$ (nm) are initial and final wavelengths chosen to integrate over the entire emission spectrum of the sample, $\gamma(\lambda)$ (cnt photon^{-1})] is the wavelength-dependent component transmission efficiency (detector, filters, lenses and cuvette), and $\Phi(\lambda)$ (photons excitation^{-1} nm^{-1}) is the differential quantum yield. A normalization of quantum yield is used such that $\int_0^\infty \Phi(\lambda) d\lambda$ gives the value published in literature for the total quantum yield of the fluorophore (Table 5.1).

The number of excitations per photon is found using

$$N_1 = 1 - 10^{-OD}, \tag{5.3}$$

where $OD = \epsilon c l$ is the optical density of the sample at the excitation wavelength, ϵ (L mol^{-1} cm^{-1}) is the extinction coefficient of the sample at the central excitation wavelength, c (mol L^{-1}) is the molar concentration of the sample and l (cm) is the cuvette length.

We estimate $\gamma(\lambda)$,

$$\gamma(\lambda) = \prod_{i=1}^{N} \mathcal{T}_{\mathrm{filter}_i}(\lambda) \prod_{j=1}^{M=3} \mathcal{T}_{\mathrm{lens}_j}(\lambda) \mathcal{T}_{\mathrm{cuvette}}(\lambda) \frac{1}{2} \left(1 + \mathcal{T}^2_{\mathrm{cuvette}}(\lambda) \mathcal{R}_{\mathrm{sph.mirror}}(\lambda)\right) QE(\lambda), \tag{5.4}$$

where $\mathcal{T}(\lambda)$ and $\mathcal{R}(\lambda)$ are the transmittance and reflectance of a given optic and $QE(\lambda)$ is the PMT quantum efficiency. The various manufacturers' specifications are used to calculate $\gamma(\lambda)$. Here, we use one filter (bandpass) (F5) and thus $N = 1$. The laser, PMT quantum efficiency, fluorophore absorption and emission and filter transmittance spectra are shown in Fig 5.3(g)-(h).

To calculate $\kappa^{'}_{\text{min}}$, we input Eq. (5.3) into Eq. (5.2), and solve for the minimum collection efficiency,

$$\kappa^{'}_{\text{min}} = \frac{F_1}{(1 - 10^{-OD})W/(h\nu) \int\limits_{\lambda_i}^{\lambda_f} \gamma(\lambda)\Phi(\lambda)d\lambda}. \tag{5.5}$$

The excitation source is a CW 458 nm laser. The beam FWHM and Rayleigh range at the focus on cam1 in Fig. E.1 is measured to be 15 μm and 1 mm respectively. This Rayleigh range suggests that the beam size will be significantly larger at the edge of the 10 mm path length cuvette compared to at the center. However, the beam has a small transverse spatial extent for all z (at $|z| = l/2$ the beam size is $\approx 4\%$ of the cuvette width) relative to the collection efficiency contour spacing in the transverse direction. Thus, the excitation volume can be approximated as a uniform cylindrical volume that extends the length of the cuvette. Using a similar argument, although the beam size is smaller than that used in the simulation (50 μm), the difference can be neglected based on the relatively large spacing of the collection efficiency contours.

We use the samples Rh6G in ethanol and fluorescein in pH 11 water. The sample is prepared at a relatively low concentration ($\approx 0.1 - 10 \times 10^{-6}$ mol L^{-1}) and the OD is measured in a spectrophotometer. During measurements, the amount of power (W) reaching the sample is measured after lens L8 and varied using the ND wheel F6 after the output of the laser (see notation in Fig. E.1). We first send the laser through the solvent to check that there is no signal due to scattered light. Next, the laser is sent through the sample and a signal is measured. The fluorescence signal is measured at six different excitation powers ranging from 10 - 150 nW.

Using the comparison of the experimentally determined and simulated minimum collection efficiency, we rescale the maximum collection efficiency of the system, $\kappa^{'}_{\text{max}} = \kappa^{'}_{\text{min}}/\kappa_{\text{min}} \times \kappa_{\text{max}}$, which goes into the experimental $K(z)^{'}$ (same as Eq. (5.1), but with $\kappa^{'}_{\text{max}}$ instead of κ_{max}). We measured an average $\kappa^{'}_{\text{min}} = 3.9 \pm 0.6\%$ and $5.4 \pm 0.7\%$ for Rh6G and fluorescein respectively. Using the average of these two, we find $\kappa^{'}_{\text{max}} = 15.4\%$.

We note that in fluorescence measurements, especially those performed at high sample concentrations, fluorescence self-absorption can reduce the measured signal. In our experiment, our narrow cuvette width minimized this effect. Our measurements suggest that self-absorption is negligible.

5.5 Calculating C2PA and E2PA Cross Sections

Here we describe the equations relevant for the calculation of the C2PA cross sections and E2PA cross-section upper bounds based on our measured data. First we describe the C2PEF signal and the derivation of C2PA cross sections from the fit to our C2PEF data. Then we describe the E2PEF signal and the derivation of E2PA cross-section upper bounds based on our measurable fluorescence lower bound.

The C2PEF signal, F_C (cnt s^{-1}), measured in our experiment can be described by

$$F_C = g \int_{-l/2}^{l/2} N_C(z) K(z)' dz \int_{\lambda_i}^{\lambda_f} \gamma(\lambda)\Phi(\lambda) d\lambda, \tag{5.6}$$

where g (pulses s^{-1}) is the pulse repetition rate, l (cm) is the cuvette path length, $N_C(z)$ (excitations cm^{-1} pulse^{-1}) is the number of excitations per infinitesimal step dz (cm) along the cuvette length per laser pulse, $K(z)'$ is the geometrical collection efficiency as a function of z (cm) as described in Eq. (5.1), $\gamma(\lambda)$ (cnt photon^{-1}) is the component transmission efficiency as described in Eq. (5.4) (where here $N = 2$) and $\Phi(\lambda)$ (photon excitation^{-1} nm^{-1}) is the differential fluorescence quantum yield. A proper normalization of quantum yield is used such that $\Phi = \int_0^\infty \Phi(\lambda) d\lambda$ gives the value published in literature (Table 5.1) for the total quantum yield of the fluorophore. The integration limits for the λ (nm) integral are set so that the integral spans over the entire emission spectrum of the fluorophore. The laser, fluorophore emission, PMT quantum efficiency and filter spectra for 2PEF measurements are shown in Fig 5.3(a)-(f).

The experimental conditions are such that ground state depletion and beam depletion are negligible [15], thus we define $N_C(z)$ as

$$N_C(z) = \frac{1}{2}\sigma_C n \int_{-1/2g}^{1/2g} \int_{-\infty}^{\infty} \int_{-\infty}^{\infty} \phi(x,y,z,t)^2 dx dy dt, \tag{5.7}$$

where σ_C (1 GM = 10^{-50} cm^4 s photon^{-1} fluorophore^{-1}) is the C2PA cross section, n (fluorophores cm^{-3}) is the number density of fluorophores and $\phi(x, y, z, t)$ (photons cm^{-2} s^{-1}) is the photon flux of the laser beam. The factor of 1/2 carries units of excitations per photons absorbed. The dx (cm) and dy (cm) integrals extend over the entire beam and the dt (fs) integral extends over the pulse repetition time ($1/g$). Equation (5.7), is related to the familiar phenomenological C2PA excitation rate, R (excitations s^{-1} fluorophore^{-1}), described in Eq. (2.6) by

$$N_C(z) = n \int_{-1/2g}^{1/2g} \int_{-\infty}^{\infty} \int_{-\infty}^{\infty} R dx dy dt, \tag{5.8}$$

with R having implied dependence on x, y, z and t.

The temporal and transverse spatial profiles of the laser beam or SPDC beam can be approximated by Gaussian distributions. Assuming the laser is always on, $\phi(x, y, z, t)$ takes the form

$$\phi(x, y, z, t) = \phi_0(z) \text{Exp}\left(-4\text{ln}2\left(\frac{x^2}{\Delta x(z)^2} + \frac{y^2}{\Delta y(z)^2}\right)\right) \sum_{i=-\infty}^{\infty} \text{Exp}\left(-4\text{ln}2\frac{(t + i/g)^2}{\tau^2}\right), \tag{5.9}$$

where $\phi_0(z)$ (photons cm^{-2} s^{-1}) is the peak photon flux as a function of z, τ (fs) is the FWHM pulse duration and $\Delta x(z)$ (cm) and $\Delta y(z)$ (cm) are the FWHM beam widths. The photon flux has z dependence because it is focused into the sample. The FWHM beam width in the x direction, for example, varies as a function of z as

$$\Delta x(z) = \Delta x_0 \sqrt{1 + (z/z_R)^2}, \tag{5.10}$$

where Δx_0 (cm) is the beam FWHM at the focus and z_R (cm) is the Rayleigh range.

We can define the average photon rate at the sample Q (photons s^{-1}) in terms of the photon flux $\phi(x, y, z, t)$,

$$Q = g \int_{-1/2g}^{1/2g} \int_{-\infty}^{\infty} \int_{-\infty}^{\infty} \phi(x, y, 0, t) dx dy dt = \frac{W}{h\nu}, \tag{5.11}$$

where W (W) is the average laser or SPDC power and $h\nu$ (J) is the average energy of an incident photon. Here we have arbitrarily chosen to use the photon flux at $z = 0$. The peak photon flux, $\phi_0(z)$, can be found from Eq. (5.11) by performing the integration of $\phi(x, y, 0, t)$ over x, y and t,

$$\phi_0(z) = \frac{W}{h\nu}\left(\frac{4\text{ln}(2)}{\pi}\right)^{3/2} \frac{1}{\Delta x(z)\Delta y(z) g\tau} = \frac{2\sqrt{2}\mu}{TA(z)}. \tag{5.12}$$

The second equality emphasizes, in accordance with Chapter 2 Section 2.3, that the peak photon flux can be expressed as $2\sqrt{2}$ multiplied by the mean photon number at the sample $\mu = Q/g$ (photons pulse^{-1}) divided by the effective mode area, $A(z)$ (cm^2), and the effective pulse duration, $T = \tau/\sqrt{2\ln(2)}$ (fs). The factors of 2 and $\sqrt{2}$ scale the photon rate to the effective photon rate at the location of the beam's peak in space and time. The effective beam area as a function of z is found through the x and y integration of the photon flux

$$A(z) = \frac{\pi \Delta x(z) \Delta y(z)}{2\ln(2)}. \tag{5.13}$$

Using Eqs. (5.7), (5.9) and (5.12), and performing the integration over x, y and t, we can rewrite Eq. (5.6) in terms of the laser power

$$F_C = \sqrt{2}\left(\frac{\ln(2)}{\pi}\right)^{3/2} \frac{\sigma_C n W^2}{\tau g\,(h\nu)^2} \int\limits_{-l/2}^{l/2} \frac{K(z)'}{\Delta x(z)\Delta y(z)} dz \int\limits_{\lambda_i}^{\lambda_f} \gamma(\lambda)\Phi(\lambda) d\lambda. \tag{5.14}$$

To derive the C2PA cross section, we solve for σ_C in Eq. (5.14),

$$\sigma_C = \frac{1}{\sqrt{2}}\left(\frac{\pi}{\ln(2)}\right)^{3/2} \frac{\tau g\,(h\nu)^2}{n} \frac{F_C/W^2}{\int\limits_{-l/2}^{l/2} K(z)'/(\Delta x(z)\Delta y(z)) dz \int\limits_{\lambda_i}^{\lambda_f} \gamma(\lambda)\Phi(\lambda) d\lambda}. \tag{5.15}$$

All the parameters in Eq. (5.15) are known for our measurements through experiments, simulations and specifications. The parameter τ is measured using a SwampOptics Grenouille 8-50-USB, g and $h\nu$ are specified by the laser manufacturer, n is measured (Appendix B), $K(z)'$ is determined through Zemax and experimental verification (Section 5.4), Δx_0, Δy_0 and z_R are measured (Appendix F), $\gamma(\lambda)$ is calculated based on optics' specifications (Section 5.4), $\Phi(\lambda)$ is known from published measurements and F_C/W^2 (cnt s^{-1} μW^{-2}) is the fit to our experimental C2PEF data. Table 5.1 shows values for sample specific parameters and Table 5.2 shows values for apparatus parameters general for all samples. The results of our C2PEF measurements produce the experimental C2PA cross sections (using Eq. (5.15)), σ_C^{exp}, shown in Table 5.3.

If we assume the expected E2PEF signal depends only linearly on photon flux, we can estimate

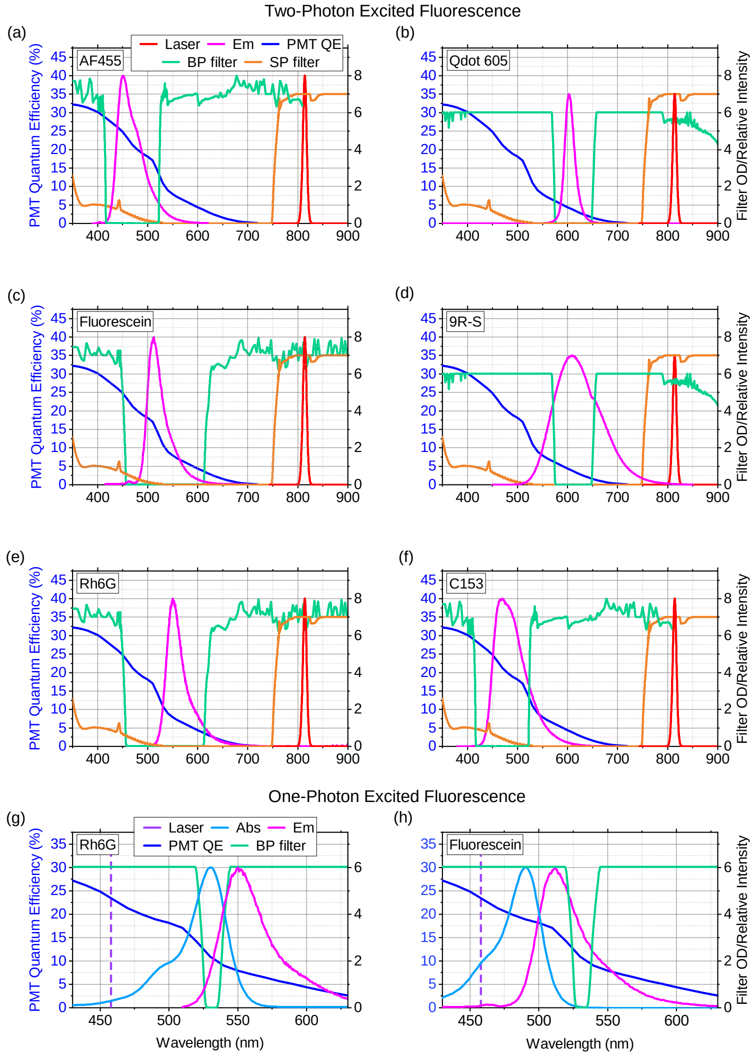

Figure 5.3: Spectral overlap summary for two-photon excited fluorescence (2PEF) measurements (a)-(f) of samples (a) AF455 in toluene, (b) qdot 605 in borate buffer, (c) fluorescein in pH 11 water, (d) 9R-S in chloroform, (e) Rh6G in methanol and (f) C153 in toluene and one-photon excited fluorescence (1PEF) collection efficiency measurements (g)-(h) of samples (g) Rh6G in ethanol and (h) fluorescein in pH 11 water. For 2PEF, the laser (red), fluorophore emission (Em) (magenta), PMT quantum efficiency (QE) (blue), bandpass (BP) filter (light green) and shortpass (SP) filter (orange) spectra are shown. The laser spectrum is measured using a USB4000 OceanOptics spectrometer. The SPDC spectrum is shown in Fig. 3.3. For 1PEF, the laser (indigo), fluorophore absorption (Abs) (light blue) and emission (Em) (magenta), PMT QE (blue) and BP filter (light green) spectra are shown. The PMT QE is indicated along the left vertical axes, whereas all other spectra use the right vertical axes. For the filters, the right vertical axes indicate the filter optical density (OD), whereas for all other spectra the right vertical axes show a relative intensity. The relative intensities of the laser, absorption and emission are normalized to the height of the peak filter OD for the respective plot. The absorption and emission spectra are measured using a spectrophotometer and fluorometer, except for qdot 605 (data taken from ThermoFisher). The PMT QE is taken from Hamamatsu specifications. All filter spectra are from the manufacturer, except for the SP filter in the 350-550 nm range (spectrophotometer).

Table 5.1: Summary of sample parameters

Sample	$c \times 10^6$ (mol L^{-1})	Φ [Ref.] (photon excitation^{-1})	$\int_{\lambda_i}^{\lambda_f} \gamma(\lambda)\Phi(\lambda)d\lambda/\Phi$
AF455	1100	0.67 [79]	0.0515
Qdot 605	8	0.74 ± 0.04 [80]	0.0285
Fluorescein	1100	0.93 [81]	0.0789
Rh6G	1500	0.90 [82]	0.0484
C153	1100	0.82 ± 0.04 [83]	0.0580
9R-S	390	0.66 [47]	0.0157

the E2PEF signal F_E (cnt s^{-1}) generated in our experiment as

$$F_E = gN_E \int_{-z_R}^{z_R} K(z)' dz \int_{\lambda_i}^{\lambda_f} \gamma(\lambda)\Phi(\lambda)d\lambda, \tag{5.16}$$

where N_E (excitations cm^{-1} pulse^{-1}) is the number of excitations per infinitesimal step dz along the cuvette length per laser pulse. The parameter N_E is defined as

$$N_E = \frac{1}{2}\sigma_E \mathcal{T} \frac{Q}{g} n, \tag{5.17}$$

where σ_E (cm^2 $\mathrm{fluorophore}^{-1}$) is the E2PA cross section and $\mathcal{T}$ is the transmittance of the photons through all the optics between the center of the crystal and the center of the sample. The parameter $\mathcal{T}$ is included in N_E but not N_C because of the result found in Chapter 2 Section 2.6 (in this Section, ϕ and Q are unlabeled but represent the values at the sample). As we mentioned in Section 5.4 and Chapter 2 Section 2.3, the dependence of the E2PA rate on the spatial overlap of photons is contained in the cross section (unlike for C2PA) and thus a cross section is only valid for a beam of constant entanglement area and thus size. Our SPDC beam is not collimated, instead we attempt to compensate for the changing entanglement area by setting the limits of the z integral from $-z_R$ to z_R, which is the region that we expect the majority of a potential E2PEF signal to arise from and should have fairly uniform entanglement area and time.

Table 5.2: Summary of apparatus parameters

Parameter	unit	Laser	SPDC
Δx_0	μm	49	51
Δy_0	μm	49	84
z_R	mm	5.1	0.4
τ	fs	111	1040
g	10^6 pulses s^{-1}	80	
$K(z)'$		$\frac{0.154}{2}\text{erfc}\,(2.78(\lvert z(\text{cm})\rvert - 1.51))$	
Q	photons s^{-1}	N/A	8.9×10^9
$\mathcal{T}$		N/A	0.76
F^{LB}	cnt s^{-1}	0.22	

We can rewrite Eq. (5.16) using Eq. (5.17),

$$F_E = \frac{1}{2}\sigma_E \mathcal{T} Q n \int_{-z_R}^{z_R} K(z)' dz \int_{\lambda_i}^{\lambda_f} \gamma(\lambda)\Phi(\lambda) d\lambda. \tag{5.18}$$

To place an upper bound on the E2PA cross section we replace F_E in Eq. (5.18) with the measurable fluorescence lower bound F^{LB} (cnt s^{-1}) and solve for σ_E, which becomes the cross-section upper bound, σ_E^{UB} (cm^2 fluorophore^{-1}),

$$\sigma_E^{\text{UB}} = \frac{2F^{\text{LB}}}{\mathcal{T} Q n \int_{-z_R}^{z_R} K(z)' dz \int_{\lambda_i}^{\lambda_f} \gamma(\lambda)\Phi(\lambda) d\lambda}. \tag{5.19}$$

F^{LB} is measured (Section 5.6), $\mathcal{T}$ is calculated based on the manufacturer's specifications, Q is measured (Chapter 3 Section 3.4) and the parameters n, $K(z)'$, $\gamma(\lambda)$ and $\Phi(\lambda)$ are found in the methods described for C2PEF. All parameters are listed in Tables 5.1 and 5.2.

In order to generate a curve for E2PEF as a function of the mean photon number (the diagonals in Fig. 5.4), the slope $\frac{F_E}{Q/g}$ is solved for in Eq. (5.18) and a selected σ_E is used. This slope is multiplied by the mean photon number on the horizontal axes.

The uncertainty on our C2PA cross sections and E2PA cross-section upper bounds are calculated by propagating the errors in all the measured and calculated parameters that go into either Eq. (5.15) or Eq. (5.19). We multiply these values by the coverage factor ($k = 2$). The uncertainty in C2PA cross sections is then $\approx 28\%$ and for E2PA cross-section upper bounds $\approx 24\%$.

5.6 Data Acquisition

In this section we describe the details of data acquisition for C2PEF and E2PEF measurements. First we describe our fluorescence background subtraction method. Next we describe how C2PEF measurements are performed. Afterwards we describe the choice of integration times for E2PEF measurements and how those measurements are performed. Lastly we describe how the measured quantities, including the measurable fluorescence lower bound, are determined.

The laser and SPDC beams are optically chopped to perform on-the-fly background subtraction on the fluorescence signal. The timetagger histogram, which shows counts registered on the PMT as a function of time, is separated into background and signal portions. The background portion (chopper blade blocking beam) is subtracted from the signal portion (chopper blade passing beam). We calibrate this background subtraction method using a strong C2PEF signal. For $\approx 5\%$ of the measurement runtime the chopper blade is neither completely blocking nor passing the beam; this portion of the measurement is discarded.

For C2PEF measurements, the laser power is controlled using a motorized half-wave plate (HWP3 in Fig. E.1). The power is measured (Thorlabs S130C power sensor and PM100D meter) by flipping the sensor into the beam using a motorized flip mount that ensures repeatable positioning. The power sensor and meter are compared with a calibrated photodiode to determine the correction factor necessary for absolute power readings. At each power, $3-5$ C2PEF measurements are performed. The integration times at higher powers are 30 seconds and at lower powers are 30 minutes.

We characterize the stability of the fluorescence measurements using an Allan deviation analysis, and base our measurement integration time for the E2PEF measurements on the result. To do this, we place the 1.10×10^{-3} mol L^{-1} fluorescein sample in the cuvette, unshutter the laser beam and measure the C2PEF signal every minute for one 14 hour period overnight and one 11 hour period during the day. We use this data to check the Allan deviation at various integration times. The Allan deviation is found to have a minimum at 45 minutes integration time.

For E2PEF measurements, the SPDC pump laser power is set to 30 mW and monitored periodically. Three E2PEF measurements are performed on each sample. These measurements are each 45 minutes long. We also block the beam periodically and take a 45 minute background measurement. We compare these measurements with those with the beam unblocked to look for significant changes in the signal. We find no changes.

The measurable fluorescence lower bound, F^{LB}, is assigned by first checking the results of C2PEF measurements at low photon flux and then by measuring "zero signal" with SPDC excitation. We measure C2PEF at rates as low as 0.38 ± 0.24 cnt s^{-1} that agree well with the quadratic fit of the C2PEF data measured at higher excitation flux. This sets our confidence in signals at least as low as 0.38 cnt s^{-1}. Next, we measure zero signal to determine what we should expect in the absence of signal. To do this, we place the 1.10×10^{-3} mol L^{-1} fluorescein sample in the cuvette, unshutter the SPDC beam and subsequently block the SPDC beam using black aluminum foil tape (Thorlabs T205-1.0) placed after filters F3 in Fig. E.1. We then acquire data for 405 minutes, or nine 45 minute measurements. The purpose of blocking the beam instead of shuttering it is to serve as an additional check for scattered light entering the detector. The fluorescein sample aids in this purpose by serving as a source that could be excited by either scattered or background light. The average of these measurements is $0.04^{+0.22}_{-0.04}$ cnt s^{-1}. It was clear from these measurements that no stray signals enter the detector. From this, our F^{LB} is set to 0.22 cnt s^{-1} (2σ from zero) with $\approx 95\%$ confidence. The value of F^{LB} sets the vertical position of the light green region in Fig. 5.4.

5.7 Results and Discussion

We measure C2PEF over a range of photon fluxes for all six fluorophores. We use the fit to our experimental data to derive C2PA cross sections (details in Section 5.5, values in Table 5.3). The values strongly agree with the cross sections reported in literature. For all six fluorophores we are unable to discern an E2PEF signal. We use our measurable fluorescence lower bound to derive upper bounds on the E2PA cross sections (details in Section 5.5, values in Table 5.3).

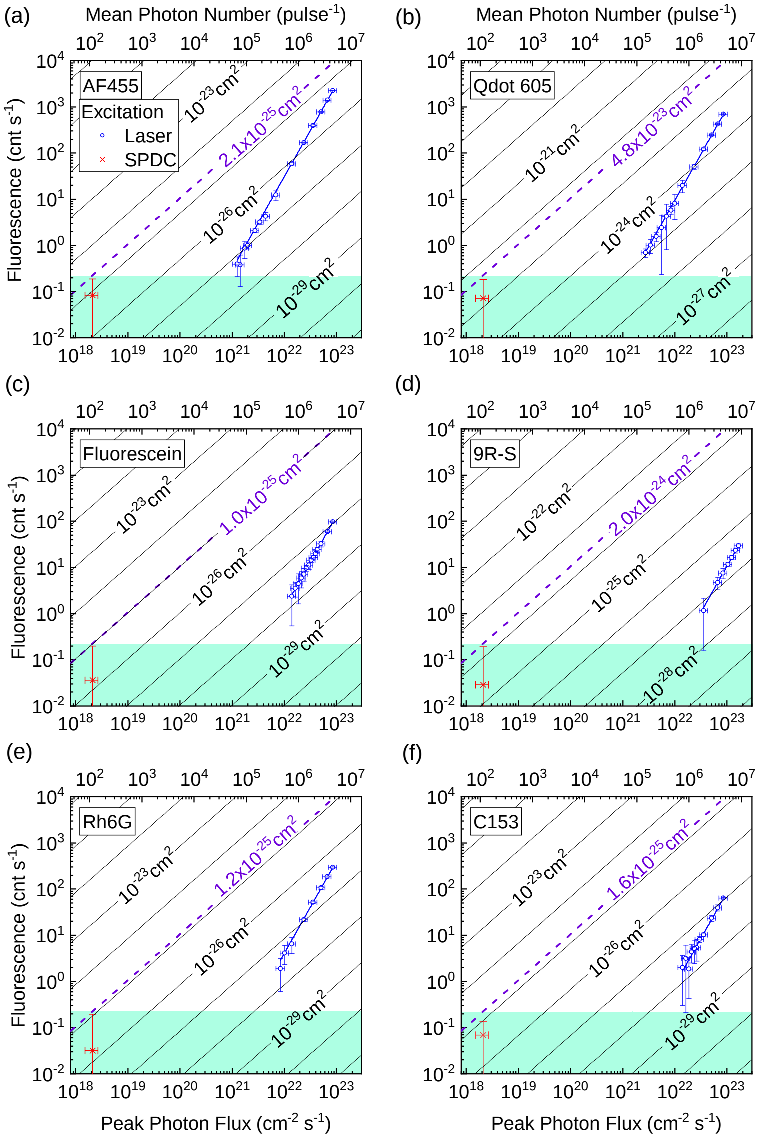

Figure 5.4: Measured (blue data points), fit (blue solid lines) and calculated (black solid and purple dashed lines) fluorescence signal (left vertical axis in cnt s^{-1}) for (a) 1.10×10^{-3} mol L^{-1} AF455 in toluene, (b) 8×10^{-6} mol L^{-1} qdot 605 in borate buffer, (c) 1.10×10^{-3} mol L^{-1} fluorescein in pH 11 water, (d) 3.90×10^{-4} mol L^{-1} 9R-S in chloroform, (e) 1.50×10^{-3} mol L^{-1} Rh6G in methanol and (f) 1.10×10^{-3} mol L^{-1} C153 in toluene. The bottom horizontal axis corresponds to the peak photon flux (photons cm^{-2} s^{-1}) of the coherent source (laser) (blue data points) or SPDC source (red data points). On the upper horizontal axis we show the SPDC mean photon number (photons $pulse^{-1}$), which corresponds to the peak photon flux on the lower horizontal axis. A signal below 0.22 cnt s^{-1} is indistinguishable from zero (green region). All E2PEF measurements produce a null result. Solid diagonal black lines show the calculated count rate expected for various potential σ_E in order-of-magnitude increments (σ_E noted along selected lines) for each fluorophore, assuming that the absorption rate is composed of only the linear photon-flux-dependent term. The purple dashed diagonal line represents the calculated count rate using σ_E^{UB} (noted in purple) for each sample.

Table 5.3: Summary of literature C2PA cross sections (σ_C^{lit}), measured C2PA cross sections (σ_C^{exp}), measured E2PA cross-section upper bounds (σ_E^{UB}), estimates for the E2PA cross sections (σ_E^{est}) (based on Eq. (2.11) using $T_e = 1620\,\text{fs}$ and $A_e = 2.1\,\mu\text{m}^2$) and measured quantum advantage upper bounds (QA^{UB}).

Sample	σ_C^{lit} [Ref.]	σ_C^{exp}	$\sigma_E^{\text{UB}} \times 10^{25}$	$\sigma_E^{\text{est}} \times 10^{30}$	QA^{UB}
	(GM)		(cm^2 fluorophore^{-1})		
AF455	350 ± 30 [17]	660 ± 180	2.1 ± 0.5	190	410 ± 140
Qdot 605	27000 ± 8000 [77]	46000 ± 13000	480 ± 120	14000	730 ± 240
Fluorescein	21 ± 2 [17]	13 ± 4	1.0 ± 0.2	3.8	2000 ± 700
9R-S	27.9 [47]	22 ± 6	20 ± 6	6.5	7000 ± 2000
Rh6G	78 ± 7 [17]	51 ± 14	1.2 ± 0.3	15	1100 ± 400
C153	17 ± 2 [17]	14 ± 4	1.6 ± 0.4	4.1	2400 ± 800

Figure 5.4 shows measured fluorescence count rates as a function of peak photon flux for both laser (blue symbols) and SPDC (red symbols) excitation for all six fluorophores on log-log plots. For all samples, we find the fit (blue line) to the C2PEF signal to have a quadratic power dependence (with exponents in the range $1.95 - 2.05$); the signals are thus free of spurious events such as 1PEF or scattered light. For AF455 (Fig. 5.4(a)), we measure C2PEF down to the lowest peak photon flux of all the samples, 1.3×10^{21} photons cm^{-2} s^{-1}, which is only 620 times larger than our SPDC peak photon flux. The C2PEF of fluorescein, 9R-S, Rh6G and C153 (Fig. 5.4(c)-(f)) is observed at a minimum flux approximately a factor of 10 higher than for AF455 and qdot 605 (Fig. 5.4(a),(b)). This minimum flux could be extended to lower values (but not as low as AF455 or qdot 605) if a longer integration time were used for the measurements. Fluorescence signals as low as 0.22 cnt s^{-1} should be measurable in our experiment (Section 5.6). We denote this measurable fluorescence lower bound as F^{LB}. A signal below this level is masked by the noise floor. As mentioned above, we do not observe E2PEF for any of the studied samples. This is demonstrated by the SPDC excitation data points (shown in red) lying below the noise floor (the green region in Fig. 5.4). For these measurements we use 30 mW pump power, which is just below the damage threshold of the SPDC crystal, to generate an SPDC peak photon flux of 2.1×10^{18} photons cm^{-2} s^{-1}.

The C2PEF measurements are averaged for each sample at each power. The E2PEF measurements are averaged for each sample. These averages are displayed on Fig. 5.4. The corresponding vertical error bars are assigned in a systematic way. First, we compare the standard deviation of the set of measurements to the sets' uncertainty due to Poisson counting statistics. The larger of these two values is multiplied by two (coverage factor $k = 2$) and used for the vertical error bar.

The horizontal error bars correspond to the uncertainty in peak photon flux (bottom axis), which is larger than the uncertainty in mean photon number (top axis). This larger uncertainty arises because of the additional uncertainty in the beam size and pulse duration. The uncertainty in the mean photon number, beam size and pulse duration is propagated to give an uncertainty in peak photon flux. A coverage factor $k = 2$ is again used to achieve $\approx 95\%$ confidence that the true value lies within the bounds set by the error bars. We note that the conversion factor from mean photon number to peak photon flux is different for the coherent source compared to the SPDC source because of its shorter pulse duration and smaller beam size. The laser conversion factor differs from that for SPDC by a factor of 16.7, thus Fig. 5.4 only shows the SPDC mean photon flux on the top horizontal axes.

We use our experimental characterizations and the component of the E2PA rate that depends linearly on excitation flux to calculate E2PEF signals for various potential values of σ_E (Section 5.5). The results of these calculations are displayed as black diagonal lines in Fig. 5.4, with the corresponding σ_E value noted along selected lines. The purple dashed diagonal line corresponds to the fluorescence signal calculated using the cross section that produces F^{LB} at the peak photon flux of our SPDC source. We denote this cross section the E2PA cross-section upper bound, σ_E^{UB}. A summary of σ_E^{UB} values is given in Table 5.3 and written in purple along the dashed diagonal lines. The sample fluorescein has the lowest σ_E^{UB} of $1.0 \pm 0.2 \times 10^{-25}$ cm^2 fluorophore^{-1}. The values of σ_E^{UB} for Rh6G, C153 and AF455 differ by less than or nearly a factor of two from that for fluorescein. Many of the parameters for these four samples are similar in magnitude: concentration, quantum yield and the overlap of the emission spectra with the fluorescence collection system's transmittance spectrum (details on these parameters in Section 5.5). For 9R-S, the upper bound is one order of magnitude larger, which results from the poor overlap of the emission and system transmittance spectra. For qdot 605, the upper bound is a factor of 24 larger than for

9R-S. This is a result of poor spectral overlap, in addition to a sample concentration two orders of magnitude lower than that used for all other samples. As recommended by the supplier, we use the concentration of qdot 605 as received to avoid compromising the chemical stability of the sample.

The upper bounds our measurements place on σ_E range from 10^{-25} to $\approx 5 \times 10^{-23}$ cm^2 fluorophore^{-1}. These are in stark contrast to the previously reported σ_E values of 10^{-21} – 10^{-16} cm^2 fluorophore^{-1} shown in Table 2.1 and Fig. 2.3. A particularly illuminating comparison can be made between our result and the published result for samples 9R-S and Rh6G. Using the previously reported σ_E values, we estimate the expected E2PEF count rate in our setup. Assuming sample 9R-S has $\sigma_E \approx 2.4 \times 10^{-19}$ cm^2 fluorophore^{-1} [47], our calculations predict an E2PEF signal of 2.6×10^4 cnt s^{-1}. For Rh6G, a value of $\sigma_E \approx 1.5 \times 10^{-21}$ cm^2 fluorophore^{-1} [48] predicts an E2PEF signal of 2.7×10^3 cnt s^{-1}. We note that Ref. [48] used 1064 nm excitation whereas we excite at 810 nm, however, if σ_E follows the same dependence on excitation wavelength as σ_C, 810 nm excitation should be more efficient by a factor of 7 [16]. In either case, we actually measure a signal that is indistinguishable from zero, which is at least three to five orders of magnitude smaller than expected based on prior reports. We are able to reach such a high cross-section sensitivity in part because of our relatively large incident SPDC photon rate (8.9×10^9 photons s^{-1}).

Although A_e and T_e likely vary between experiments, we have no reason to believe these parameters alone differ by the many orders of magnitude required to explain this discrepancy. However, because A_e and T_e alter σ_E and because the role of these parameters is not completely understood for E2PA in molecules, A_e and T_e should be reported alongside σ_E values whenever possible. There are other experimental parameters that vary between experiments, such as pump laser and SPDC spectral and temporal widths and the SPDC crystal characteristics. The effects of these differences are not well known and need more thorough study.

Table 5.3 also shows estimates of the E2PA cross section for the six fluorophores, σ_E^{est}. These estimates are based on the relation given in Eq. (2.11) using our derived σ_C^{exp} given in Table 5.3 and our estimates of T_e and A_e specified in Section 5.3. We use the lower bound of A_e in this estimation to show the largest value σ_E^{est} could take on. Although we do not anticipate Eq. (2.11) to yield an exact result, this estimate can provide useful insight about σ_E values in a similar manner to the estimates of ionization cross sections for atoms in Ref. [84]. These σ_E^{est} values are three to five orders of magnitude below our established cross-section upper bounds. These estimates provide a reference for the cross-section sensitivity necessary to observe E2PA.

We use our C2PEF and E2PEF results to determine an upper bound on the "quantum advantage" of 2PA (QA^{UB}). As previously mentioned (Chapter 2), we define the quantum advantage (QA) as the ratio of the minimum photon flux required to observe C2PA to that for E2PA. By extrapolating our C2PEF fit to F^{LB} for the sample AF455, for example, we determine that C2PEF should be measurable down to 8.5×10^{20} photons cm^{-2} s^{-1}. E2PEF is not measurable at our maximum SPDC photon flux, 2.1×10^{18} photons cm^{-2} s^{-1}, but might be measurable at a higher photon flux. Thus, QA^{UB} of 2PA for this sample is 410. Values of QA^{UB} for all the samples (Table 5.3) range from $410 - 7000$, in contrast with QA of nearly 10^{10} in previous reports [52, 54]. It is worth mentioning that the QA can be increased if A_e and T_e are decreased while all other excitation parameters are held fixed, however a many-orders-of-magnitude increase is unlikely.

There are other publications in this field that support our findings. In particular, Ashkenazy *et al.* [85] argued that using "typical" values of A_e ($50\,\mu\text{m}^2$) and T_e (50 fs), they can estimate $\sigma_E \approx 10^{-29}$ cm^2 fluorophore^{-1} for metallic nanoparticles with a large C2PA cross section ($\sigma_C \approx$ 100 GM at 1050 nm). Cross sections of this size are in agreement with our established bounds of σ_E. Another interesting example is provided in the recent work by Li *et al.* [86] who used a single setup to measure both C2PEF and squeezed-light 2PEF (SL2PEF) of the samples DCM in dimethyl sulfoxide and fluorescein in pH 13 water. The squeezed light generated by four-wave mixing in a Rubidium vapor cell was varied over the range of $10^{13} - 10^{16}$ photons s^{-1} (compare to our $\approx 10^{10}$ SPDC photons s^{-1}). The SL2PEF signals from DCM and fluorescein are factors of $\approx 2.0 - 2.8$ and ≈ 47 larger, respectively, than the C2PEF signals at the same excitation flux. The authors did not report values for cross sections. However, these significant but modest enhancements and the fact that measurements were performed with a squeezed light source that provides orders-of-magnitude higher photon rate than an SPDC source, are consistent with the upper bounds established in this study.

5.8 Conclusions

In this chapter, we discussed important aspects of designing and implementing a fluorescence-based E2PA measurement. We presented an experimental apparatus for measuring E2PEF and C2PEF in nearly identical experimental conditions. The results from C2PEF serve as a vital reference point for the capability of our fluorescence system. Although we do not observe an E2PEF signal, our results set upper bounds on σ_E of the six chosen fluorophores in the range of $10^{-25} - 5 \times 10^{-23}$ cm^2 fluorophore^{-1}. Two of these samples have published σ_E values that are four and five orders of magnitude larger than the upper bounds we report.

We emphasize that σ_E depends on spatio-temporal properties of the excitation source, unlike σ_C. Without knowing the entanglement area and entanglement time, there is significant ambiguity in comparing cross sections measured in different experimental apparatuses. For our source, we estimated a range within which our entanglement area is constrained, $2.1 - 13,700\,\mu\text{m}^2$, and we estimated the entanglement time, 1620 fs, based on our measured SPDC spectrum and estimated group delay dispersion. While we had hoped to measure these quantities directly, in lieu of this we made explicit the details of our setup and the assumptions that went into the estimation of these quantities.

Our results differ significantly from previous E2PA publications using SPDC excitation. Our evidence indicates that E2PA cross sections are orders of magnitude smaller than previously claimed [51, 53, 63, 52, 50, 54, 47, 64, 55, 49, 48]. As we demonstrated in this report, the clarification of the inconsistencies in the field is underway. This is an important step forward in the quantification of the achievable "quantum advantage" and thus the merit of E2PA for spectroscopy and imaging applications.

Chapter 6

Bounding Entangled Two-Photon Absorption Cross Sections with Sensitive Transmittance Measurements

6.1 Publication Note

This chapter is an expansion of the work summarized in:

[60] Mazurek, M.D., Parzuchowski, K.M., Mikhaylov, A., Nam, S.W., Camp, C.H., Gerrits, T., Jimenez, R. and Stevens, M.J., 2021, May. Bounding entangled two-photon absorption with sensitive transmittance measurements. In *CLEO: QELS Fundamental Science* (pp. FM3N-2). Optica Publishing Group.

6.2 Introduction

In our first transmittance experiment (Chapter 4) we set upper bounds on entangled two-photon absorption (E2PA) cross sections using a transmittance-based measurement scheme that included an interferometer for a time delay. The sensitivity to changes in transmittance was at the 1% level and was limited because of residual interference artifacts. In this experiment we improve on that experiment to achieve a higher sensitivity. We incorporate a mirror mounted on a piezo-electric transducer in the delay arm of the interferometer for quick scans over interference fringes, we add a quadrant detector to monitor and account for pump beam power and pointing stability, we improve the data acquisition technique to allow for long but stable measurements and we improve the data analysis technique. We achieve a sensitivity of 0.05%. We take measurements with seven different molecules in solution at multiple concentrations, and observe no statistically significant change in transmittance. We set upper bounds on the E2PA cross sections in the range $10^{-22} - 10^{-19}$ cm^2 absorber^{-1}.

6.3 Operating Principle of the Experiment

Fig. 6.1 displays an illustration of our experimental setup, which we use to explain the operating procedure of our measurement technique. A photon pair passes through an interferometer with variable time delay. Varying the photons' temporal overlap affects the rate of 2PA in the sample (Chapter 2 Section 2.6). By using polarizing beamsplitters we ensure that any light that reaches detector D_1 (D_2) arrives via the stationary (delay) arm of the interferometer. (In reality, due to experimental imperfections, a small fraction of the light that travels through the delay arm may "leak-into" D_1. For simplicity, in this section we assume this fraction is negligible. However, we account for non-zero leakage in our final analysis, and we explain how in Section 6.5.)

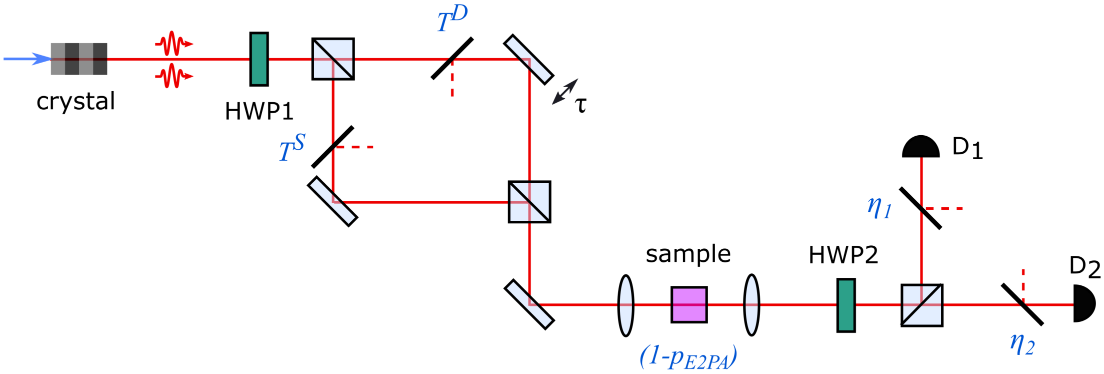

Figure 6.1: Cartoon of our experimental setup. Photon pairs are created in the SPDC crystal, after which they are probabilistically split via half-wave plate HWP1 and a polarizing beamsplitter (PBS) into two paths through an interferometer before reaching a sample. The interferometer's delay arm D contains a moveable mirror which can add a time-delay τ relative to the interferometer's stationary arm, S. One-photon loss between the crystal and sample is represented by beamsplitters inside the interferometer with transmission probabilities T^S and T^D. If both photons arrive at the sample, they will be absorbed via 2PA with probability p_{E2PA}. Half-wave plate HWP2 is rotated to ensure that all photons which traversed through the sample via the stationary arm will be directed to detector D_1, and photons from the delay arm are sent towards D_2. One-photon loss between the sample and detectors (including internal detector inefficiencies) is represented with the beamsplitters with transmission efficiencies η_1 and η_2.

The main advantage of this technique is that we can vary the 2PA rate without changing the contents of—and therefore the one-photon loss through—the cuvette. Furthermore, varying the time delay does not affect light that traverses the stationary arm, and thus the total amount of one-photon loss between the crystal and D_1 should remain constant at all time delays. As a result, if we measure a delay dependence in the click rate at D_1, we can infer that 2PA has occurred.

To infer a specific 2PA rate from this delay-dependent measurement, we compare the expected count rates at $\tau = 0$ (where the 2PA rate is maximized) to those at a very large delay $\tau = \mathcal{T}$, (where the 2PA rate is minimized). The probability that any individual photon reaches the cuvette via the stationary arm is equal to the total transmission efficiency from the crystal to the cuvette, $T^S_{XS} = R_{PBS}T^S$ where R_{PBS} is the reflection efficiency of the PBS and T^S is the transmission efficiency of all other optics between the crystal and the cuvette along the stationary arm path. Similarly, a photon will reach the sample via the delay arm with probability $T^D_{XS} = T_{PBS}T^D$ where T_{PBS} is the transmission efficiency of the PBS and T^D is the transmission efficiency of all other optics between the crystal and the cuvette along the delay arm path. If two photons arrive at the sample with negligible time delay between them, they will excite the sample via 2PA with probability p_{E2PA}. The one-photon transmission efficiency through the cuvette and to detector D_1 (D_2) (and including the detector's internal quantum efficiency) is η_1 (η_2). There are three paths the photon pairs may take through the setup which can result in a click at D_1—both photons can travel through the stationary arm, one photon can travel through each arm, or one photon may travel through the stationary arm while the other is lost. Assuming the source emits N photon pairs each second (and assuming the source is much more likely to emit a single pair than multiple pairs at the same time), the average click rate at D_1 is given by:

$$\begin{aligned} S_1(\tau) = N \Big[&\left(T^S_{XS}\right)^2 \left(1 - p_{E2PA}\right) \left(2\eta_1 - \eta_1^2\right) \\ &+ 2T^S_{XS}T^D_{XS} \left(1 - f(\tau)p_{ETPA}\right) \eta_1 + 2T^S_{XS} \left(1 - T^S_{XS} - T^D_{XS}\right) \eta_1 \Big] . \end{aligned} \tag{6.1}$$

The function $f(\tau)$ captures the time-dependence of the 2PA rate as a function of time delay: at zero delay $f(0) = 1$ and at large delay $f(\mathcal{T}) = 0$. The normalized change in click rate at these two time delays (also called the change in transmittance) is $\Delta S = \frac{(S_1(\mathcal{T}) - S_1(0))}{S_1(\mathcal{T})}$. Using Eq. (6.1) and rearranging, we find the two photon absorption probability, p_{E2PA} as:

$$p_{E2PA} = \frac{\Delta S(2 - T^S_{XS}\eta_1)}{\Delta S T^S_{XS}(2 - \eta_1) + 2T^D_{XS}}. \tag{6.2}$$

The efficiencies T^S_{XS} and T^D_{XS} can be independently characterized, and the product $T^S_{XS}\eta_1$ can be measured using a version of Klyshko's efficiency equation [87] (see Section 6.5.1 for details).

While p_{E2PA} is defined as the probability of exciting one molecule in the sample if exactly one pair of photons interacts with the sample, it can also be understood as the total 2PA rate that would occur if pairs reached the sample at an average rate of one pair per second. The E2PA rate is defined as

$$R_E = \frac{1}{2}\sigma_E Q n l, \tag{6.3}$$

where σ_E (cm^2 molecule^{-1}) is the E2PA cross section, Q (photons s^{-1}) is the single photon rate at the sample, n is the number density of the molecule in solution and l is the cuvette length. Therefore, once p_{E2PA} is characterized, we can solve for the E2PA cross section with:

$$\sigma_E = \frac{p_{E2PA}}{nl}. \tag{6.4}$$

To first order, the measured change in click rate ΔS is linearly proportional to the 2PA probability p_{E2PA} and also to the E2PA cross section σ_E. Therefore, a sensitive measurement of ΔS can provide a sensitive characterization of σ_E.

6.4 Experimental Setup

Our experimental setup consists of a photon-pair source, an interferometer, a sample and a single-mode detection stage (Fig. 6.2). Here we give a brief overview of the setup, a thorough description of the components is given in Appendix G. The photon-pair source is as described in Chapter 3, Section 3.3. In this experiment we pick off a small fraction of the 405 nm pump light and measure it with a quadrant photodiode to monitor fluctuations in total beam power and pointing direction. Due to chromatic dispersion between the SPDC crystal and sample, wavelength components far from the central wavelength contribute minimally to 2PA—keeping them would decrease the overall sensitivity of our measurement, therefore we filter the photon pairs so their marginal spectrum has a full width at half maximum (FWHM) of about 12 nm.

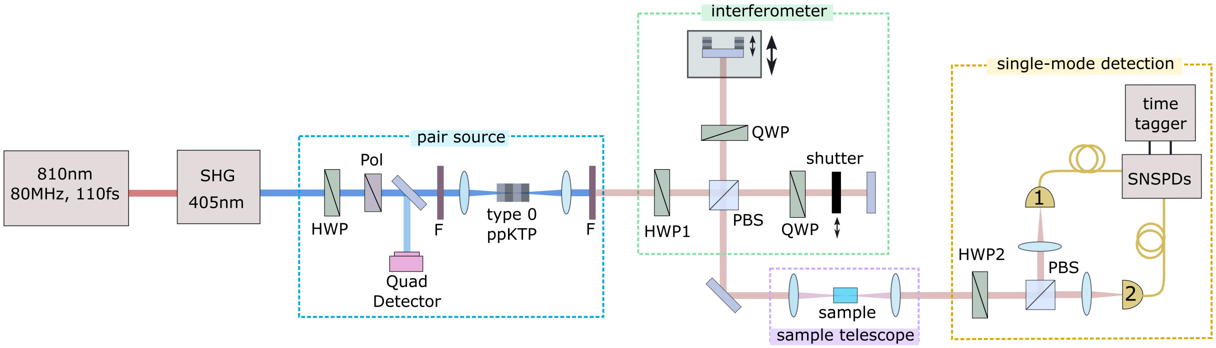

Figure 6.2: Schematic of the experimental setup. The 810 nm laser (dark red) is frequency doubled (blue) via second-harmonic generation (SHG) and focused into a type-0 ppKTP crystal to generate collinear SPDC photon pairs at 810 nm (light red). Filters (F) are used to remove the remaining 405 nm light. A half-wave plate (HWP1) rotates the polarization of the photons such that they are split probabilistically and equally at a polarizing beamsplitter (PBS). Half of the light travels through the delay arm of the interferometer. This arm has a mirror mounted on a piezo which itself is mounted on a motorized delay stage for time delay control. The other half travels through the stationary arm. The light is recombined at a PBS and focused into a sample. The transmitted light is collimated and detected at the single-mode detection stage. HWP2 switches between detection modes.

We measure the joint spectral intensity (JSI) of our source using the time-of-fight spectrometer described in Chapter 3 Section 3.6. The result is shown in Fig. 6.3(a). The bandwidth is set by a bandpass filter placed after the SPDC source. The JSI projections onto vertical and horizontal axes in Fig. 6.3(b) are used to estimate the marginal FWHM bandwidths of the photons, which are 11.1 nm and 12.8 nm. We estimate the total group delay dispersion (GDD) of our optical elements between the ppKTP crystal and the center of the sample to be approximately 2800 fs^2 at 810 nm. We use this GDD to simulate the joint temporal intensity (JTI) using the procedure described in Chapter 3 Section 3.7. The result is shown in Fig. 6.3(c). The FWHM of the projection of the JTI onto the antidiagonal axis (Fig. 6.3(d)) is used to estimate the entanglement time, which is 153 fs. We note that this size of GDD has a small effect on our entanglement time due to the narrow bandwidth of our filtered SPDC. The pulse duration of the SPDC can be estimated by the projections of the JTI onto the horizontal and vertical axes and is ≈ 190 fs.

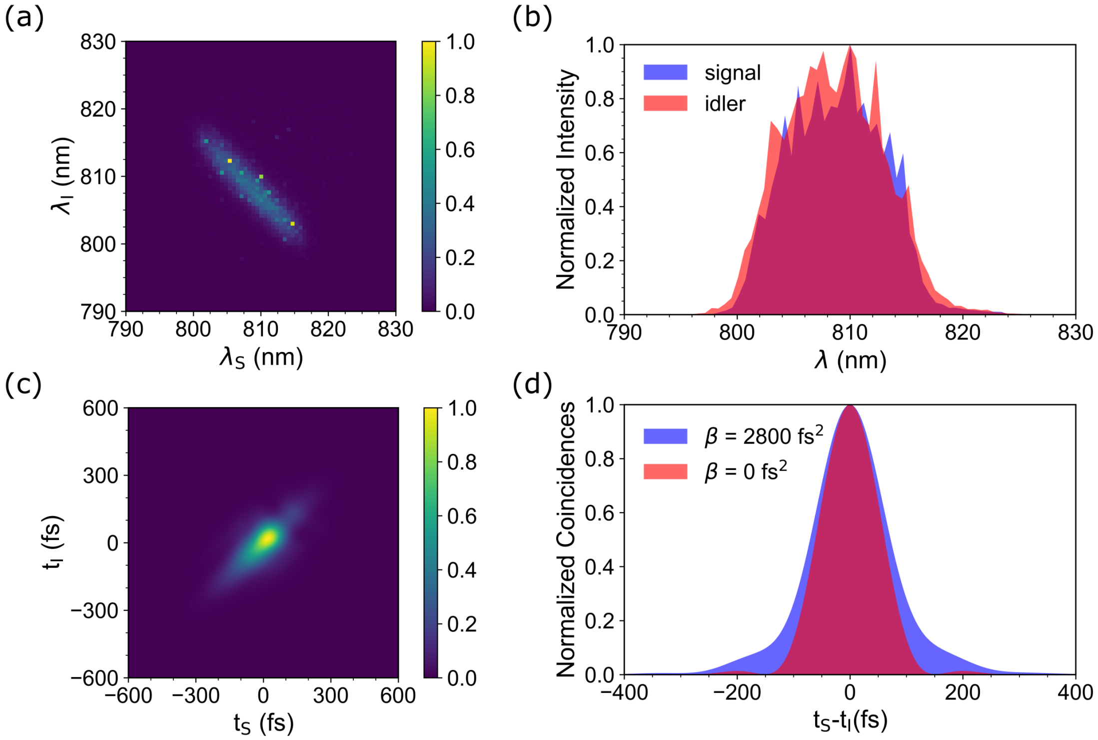

Figure 6.3: (a) Measured joint spectral intensity (JSI) where $\lambda_{\mathrm{S,I}}$ are the signal and idler wavelengths. (b) The JSI is projected onto the horizontal axis and vertical axis showing the signal (blue) and idler (red) spectra respectively. The FWHM of the signal and idler spectra are 11.1 and 12.8 nm respectively, which is set by an optical filter. The overlap of the spectra is evident in the dark red region. (c) Calculated joint temporal intensity (JTI) obtained through a discrete Fourier transform. (d) Projection onto the antidiagonal axis, $\mathrm{t_S}$-$\mathrm{t_I}$, of the JTI shown in (c) (blue) and for a transform-limited ($\beta = 0\,\mathrm{fs}^2$) pulse (red). The FWHM of these projections are 153 fs and 131 fs.

After the source stage of the experiment, a half-wave plate (HWP1) rotates the photon pairs to diagonal linear polarization, before a polarizing beamsplitter (PBS) probabilistically splits the pairs into two arms of a Michelson interferometer. The end mirror in the delay arm is mounted on a piezo-electric transducer which sits on a delay stage, for fine and coarse control of delay. A quarter-wave plate (QWP) in each interferometer arm rotates the polarization so that light from both arms is recombined into a single beam before it is focused with a 75 mm focal length lens into a 10 mm long quartz cuvette containing the sample under test. The beam size at the focus and the Rayleigh range is measured using an 810 nm diode laser back-propagated through the fiber of the single-mode detection stage and all the optics to the sample position. The FWHM beam size is $\approx 59\,\mu$m and the Rayleigh range is ≈ 9.1 mm. The full set of samples we measure is summarized in Table 6.1.

The light is collimated after the sample, and then travels through the single-mode detection stage (Chapter 3 Section 3.3). Rotating half-wave plate HWP2 to 0° ensures that all light from the stationary (delay) arm is sent towards detector D_1 (D_2), and this is the configuration we measure 2PA in. We can rotate HWP2 to 22.5° to observe interference in the click rates at each detector, as well as the coincidences between them (Fig. 6.4). These interference patterns also indicate the zero-delay position of our interferometer. Critically, the visibility of the interference pattern quantifies the overlap of the beams from both interferometer arms—a high visibility indicates high temporal and spatial overlap. In Chapter 4 Section 4.5 we discussed how to model this interference pattern.

To characterize each sample, we compare D_1's click rate when measured at zero delay, and at a 4 mm delay (corresponding to 27 ps). We perform many measurements at each delay, and repeatedly switch between them. Due to small alignment and manufacturing imperfections in the polarization optics in our setup, a small amount of light from the delay arm leaks into detector D_1. As a result, with HWP2 set to 0 degrees and near zero delay, we measure small residual interference fringes in the click rate at D_1, with visibility on the order of ≈1%. Since these residual fringes can lead to a roughly 1% difference in the click rates at both delays, we average over them using two methods. First, we constantly vary the position of the delay-arm mirror via a piezo-electric mount which is driven by a triangular voltage wave with amplitude set to average over five interference fringes. Second, we implement further averaging by performing measurements at 14 different motor positions around each delay value (which corresponds to averaging over roughly 2 fringes). Due to differences in the delay-arm alignment at both delays, the amount of delay-arm light that is coupled into D_1 is different at the two delays. To measure the average leakage rate we also perform background measurements at both delays, by physically blocking the interferometer's stationary arm with a shutter. Finally, to monitor drifts in the power and pointing-direction of the 405 nm beam, we constantly measure the outputs of the quadrant photodiode. We measure each sample

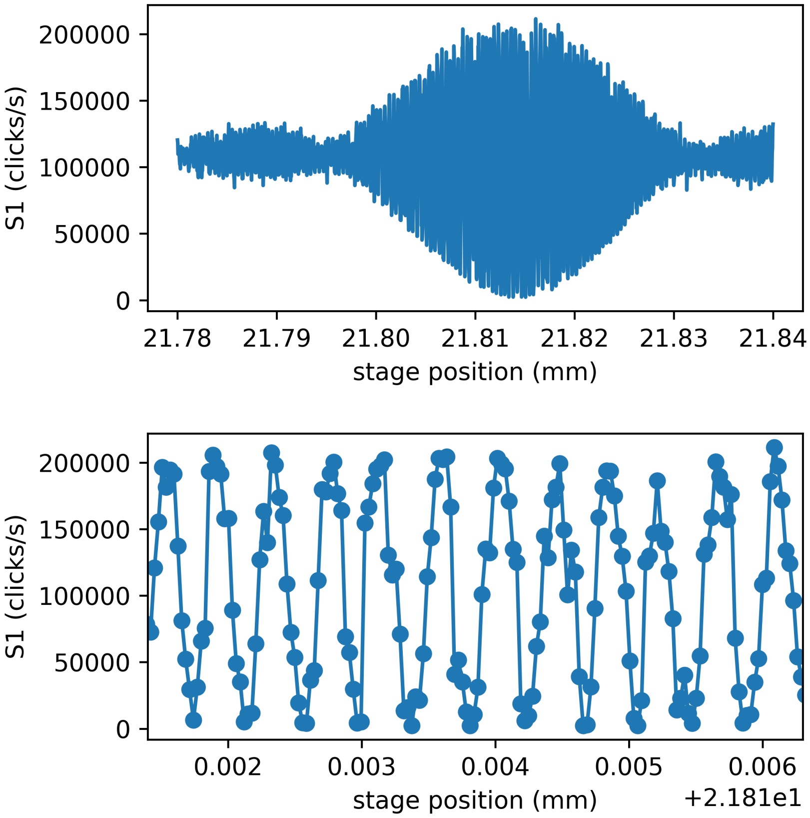

Figure 6.4: Typical interference pattern measured with HWP2 set to an angle of 22.5°. Top panel shows that the interferometer arms are considered balanced over a range of less than 0.1 mm of stage delay, much less than the 2 mm of stage delay (4 mm total delay) that we move to for 'large-delay' measurements. The bottom panel displays individual interference fringes near zero delay, with a visibility $V \approx 98\%$ — this high visibility implies that, inside the sample, light which has arrived via the stationary interferometer arm has very high modal overlap with light that that has arrived via the delay arm.

for a total of 34-65 hours corresponding to a total of roughly 1000-1900 independent measurements at each delay.

6.5 Inferring 2PA Probability

In our experiment, we measure the parameter ΔS which is the relative change in the detection rate at detector D_1 as we move the interferometer from large delay to zero delay. Our task is to infer a 2PA rate from a measurement of ΔS. In Section 6.3 we explain how to perform this inference for an experiment which satisfies two ideal assumptions; first that all the light that travels the stationary (delay) arm ends up at detector D_1 (D_2) and second that the detectors have no background counts. In this section we relax both of those assumptions and find a modified form of Eq. (6.2) which we use to infer an upper bound on p_{E2PA} from our measurement of ΔS.

To perform this inference, we begin by deriving an equation for the expected count rate S_1 at detector D_1 as a function of the transmission efficiencies through various sections of the setup. For each photon pair generated at the crystal there are five distinct paths the pair can take which may lead to a click at D_1. First, both photons could make it to the sample, and this can happen one of three ways: either both photons traverse the stationary arm (which we label path SS), both traverse the delay arm (path $D_\tau D_\tau$) or one photon traverses each arm (path SD_τ). Here the τ subscript on the delay arm labels if the interferometer is in the balanced ($\tau = 0$) or unbalanced ($\tau = \mathcal{T}$) position. If both photons reach the sample, they will make it through the sample with probability $(1 - p_{E2PA}^{path})$ — the *path* label allows us to account for the 2PA probability to depend on the specific path the two photons take before reaching the sample. Second, it is possible that only one photon reaches the sample, which can happen one of two ways: one photon is lost and the other takes the stationary arm (path S) or one photon is lost and the other takes the delay arm (path D_τ). When only one photon reaches the sample, no 2PA can occur. If one or two photons are transmitted through the sample, D_1 will click with a probability that depends on the number of photons (i.e. one or two) and the specific path the photon(s) travelled. After the sample, a single photon will make D_1 click with probability η_1^{path}.

To find an equation for the expected count rate at D_1, we start with equations for the probability that the pair of photons traverses each of the five paths explained in the above paragraph.

These are:

$$p^{SS} = (T^S_{XS})^2, \tag{6.5}$$

$$p^{D_\tau D_\tau} = (T^D_{XS})^2, \tag{6.6}$$

$$p^{SD_\tau} = 2T^S_{XS}T^D_{XS}, \tag{6.7}$$

$$p^S = 2T^S_{XS}(1 - T^S_{XS} - T^D_{XS}), \tag{6.8}$$

$$p^{D_\tau} = 2T^D_{XS}(1 - T^S_{XS} - T^D_{XS}), \tag{6.9}$$

where the transmission efficiency T^S_{XS} (T^D_{XS}) is the probability that a photon created at the crystal will traverse the interferometer's stationary (delay) arm and reach the sample. Because the path from crystal to sample is in free-space, we expect small changes in alignment caused by moving the delay arm to at most have a negligible effect on the delay-arm transmission efficiency T^D_{XS}. Thus we assume that the efficiency from the crystal to the sample via the delay arm is independent of the time delay in the interferometer, which is why we write T^D_{XS} without the τ subscript on the path-label D.

Next, we write down the conditional probabilities that D_1 will click, given the photon pair has travelled a specific path:

$$p(\text{click}|SS) = (1 - p^{SS}_{E2PA})(2\eta^S_1 - (\eta^S_1)^2), \tag{6.10}$$

$$p(\text{click}|D_\tau D_\tau) = (1 - p^{D_\tau D_\tau}_{E2PA})(2\eta^{D_\tau}_1 - (\eta^{D_\tau}_1)^2), \tag{6.11}$$

$$p(\text{click}|SD_\tau) = (1 - p^{SD_\tau}_{E2PA})(\eta^S_1 + \eta^{D_\tau}_1 - \eta^S_1\eta^{D_\tau}_1), \tag{6.12}$$

$$p(\text{click}|S) = \eta^S_1, \tag{6.13}$$

$$p(\text{click}|D_\tau) = \eta^{D_\tau}_1, \tag{6.14}$$

where the efficiency η^S_1 ($\eta^{D_\tau}_1$) is the probability that a single photon that travels path S (D_τ) **and** is transmitted through the sample will reach D_1 and cause it to click. Because the light is coupled into fiber between the sample and detector D_1, we expect that small alignment changes in the delay arm may lead to large changes in the fiber-coupling efficiency, and so we allow the efficiency $\eta^{D_\tau}_1$ to depend on the time delay in the interferometer.

We can use Eqs. (6.5)-(6.14) to find the desired equation for the expected rate of clicks at D_1:

$$\begin{aligned} S_1(\tau) = N \Big[&(T^S_{XS})^2(1-p^{SS}_{E2PA})(2\eta^S_1 - (\eta^S_1)^2) \\ &+ (T^D_{XS})^2(1-p^{D_\tau D_\tau}_{E2PA})(2\eta^{D_\tau}_1 - (\eta^{D_\tau}_1)^2) \\ &+ 2T^S_{XS}T^D_{XS}(1-p^{SD_\tau}_{E2PA})(\eta^S_1 + \eta^{D_\tau}_1 - \eta^S_1\eta^{D_\tau}_1) \\ &+ 2T^S_{XS}(1-T^S_{XS}-T^D_{XS})\eta^S_1 \\ &+ 2T^D_{XS}(1-T^S_{XS}-T^D_{XS})\eta^{D_\tau}_1 \Big] + p_{BG}, \end{aligned} \tag{6.15}$$

where N is the pair-production rate at the source and we have introduced the parameter p_{BG} to represent the background and dark count rate on D_1. If we make the substitutions $\eta^{D_\tau}_1 \to 0$ and $p_{BG} \to 0$, we recover Eq. (6.1).

To estimate (and subtract) the rate of leakage from the delay arm into D_1, we also perform measurements with a shutter blocking the stationary interferometer arm. In this configuration, we have $T^S_{XS} = 0$, and measure

$$\begin{aligned} S^{BG}_1(\tau) = N \Big[&(T^D_{XS})^2(1-p^{D_\tau D_\tau}_{E2PA})(2\eta^{D_\tau}_1 - (\eta^{D_\tau}_1)^2) \\ &+ 2T^D_{XS}(1-T^S_{XS}-T^D_{XS})\eta^{D_\tau}_1 \Big] + p_{BG}. \end{aligned} \tag{6.16}$$

We then subtract our measurement of $S^{BG}_1(\tau)$ from $S_1(\tau)$ to find the **corrected** click rate at D_1:

$$\begin{aligned} S^{corr}_1(\tau) = N \big[&(T^S_{XS})^2(1-p^{SS}_{E2PA})(2\eta^S_1 - (\eta^S_1)^2) \\ &+ 2T^S_{XS}T^D_{XS}(1-p^{SD_\tau}_{E2PA})(\eta^S_1 + \eta^{D_\tau}_1 - \eta^S_1\eta^{D_\tau}_1) \\ &+ 2T^S_{XS}(1-T^S_{XS}-T^D_{XS})\eta^S_1 \big] . \end{aligned} \tag{6.17}$$

We calculate ΔS^{corr} using the corrected click rates at D_1:

$$\Delta S^{corr} = \frac{S^{corr}_1(\mathcal{T}) - S^{corr}_1(0)}{S^{corr}_1(\mathcal{T})}. \tag{6.18}$$

In general, we expect the 2PA probability to be identical for the SS and $D_\tau D_\tau$ paths, since in these cases both photons travel identical paths between the crystal and sample and therefore should be perfectly overlapped in the sample. However, the modal overlap between the stationary and delay arms may not be 100%, and thus in general we expect $p_{E2PA}^{SD_\tau} < p_{E2PA}^{SS} = p_{E2PA}^{D_\tau D_\tau}$. We can quantify this overlap by looking at the visibility, V, of the interference pattern we measure when we rotate HWP2 to 22.5°, and we expect $p_{E2PA}^{SD_\tau} = Vp_{E2PA}^{SS}$. At large delay, $\tau = \mathcal{T}$, this visibility is zero, which is why we expect no 2PA to occur if the pair traverses the $SD_{\mathcal{T}}$ path. With this definition, we can write ΔS as a function of p_{E2PA}^{SS}, the near-zero-delay visibility, V, and the one-photon transmission and detection efficiencies throughout the setup:

$$\Delta S^{corr} = \frac{T_{XS}^{D}\left[Vp_{E2PA}^{SS}\left(1+\frac{\eta_1^{D_0}}{\eta_1^{S}}\right) + (1 - Vp_{E2PA}^{SS})\eta_1^{D_0} - \eta_1^{D_{\mathcal{T}}}\right]}{T_{XS}^{S}\left[(1-p_{E2PA}^{SS})(1-\frac{1}{2}\eta_1^{S}) - 1\right] + 1 - T_{XS}^{D}\eta_1^{D_{\mathcal{T}}}}. \tag{6.19}$$

Finally, we can rearrange Eq. 6.19 to solve for p_{E2PA}^{SS}, which is the main result of this section:

$$p_{E2PA}^{SS} = \frac{\Delta S^{corr}\eta_1^{S}(1-\frac{1}{2}T_{XS}^{S}\eta_1^{S} - T_{XS}^{D}\eta_1^{D_{\mathcal{T}}}) - \eta_1^{S}T_{XS}^{D}(\eta_1^{D_0} - \eta_1^{D_{\mathcal{T}}})}{\Delta S^{corr}T_{XS}^{S}\eta_1^{S}(1-\frac{1}{2}\eta_1^{S}) + VT_{XS}^{D}(\eta_1^{S} + \eta_1^{D_0} - \eta_1^{S}\eta_1^{D_0})}. \tag{6.20}$$

If we make the simplifying assumptions that $\eta_1^{D_\tau} = 0$ and $V = 1$, we recover Eq. (6.2).

In the next section, we explain how to estimate the efficiencies η_1^{S} and $\eta_1^{D_\tau}$ from the count rates we measure on detectors D_1 and D_2, as well as the coincidence rate between them. We are able to estimate p_{E2PA}^{SS} by using Eq. (6.20) in conjunction with Eqs. (6.25) and (6.27) that we present below.

If there is no significant E2PA probability (i.e. $p_{E2PA}^{SS} \approx 0$), we can use p_{E2PA}^{SS} to upper bound the E2PA cross section (σ_E^{UB}). Similar to Eq. (6.4), we define

$$\sigma_E^{\mathrm{UB}} = \frac{p_{E2PA}}{nl} + 2\delta\sigma_E, \tag{6.21}$$

where $\delta\sigma_E$ is the propagated error from the Allan deviation of the dataset for the selected averaging chunk size (as discussed in Section 6.6) and the measurement of the concentration.

6.5.1 Estimating Detection Efficiencies

Eq. (6.20) above gives us the p_{E2PA}^{SS} probability as a function of ΔS, the interference visibility V, and the one-photon transmission and detection efficiencies through the setup. We have discussed how to measure ΔS and V, and it is relatively straightforward to measure the T_{XS}^{path} efficiencies. We can use a version of Klyshko's method [87] to measure the detection efficiencies η_1^S and $\eta_1^{D_\tau}$, and in this section we describe how to do so. We start with η_1^S, and again we begin with equations for the rate of clicks at detectors D_1, D_2, and coincidences between both detectors. In the limits $p_{E2PA} << 1$, $\eta_1^{D_\tau} << \eta_1^S$, and $\eta_2^S << \eta_2^{D_\tau}$, we can write our equation for the background-corrected rate of clicks at D_1 (Eq. (6.17)) as:

$$S_1^{corr}(\tau) \approx 2N\eta_1^S T_{XS}^S(1 - \frac{1}{2}\eta_1^S T_{XS}^S). \tag{6.22}$$

Similarly, the background-corrected rate at D_2 is:

$$S_2^{corr}(\tau) \approx 2N\eta_2^{D_\tau} T_{XS}^D(1 - \frac{1}{2}\eta_2^{D_\tau} T_{XS}^D), \tag{6.23}$$

and the coincidence rate between the two detectors is:

$$C(\tau) \approx 2NT_{XS}^S T_{XS}^D \eta_1^S \eta_2^{D_\tau}. \tag{6.24}$$

We can solve the above system of equations for η_1^S, arriving at:

$$\eta_1^S = \frac{1}{T_{XS}^S}\frac{C(\tau)}{S_2^{corr}(\tau)}\left(1 - \frac{1}{2}\frac{C(\tau)}{S_1^{corr}(\tau)}\right)\left(1 - \frac{1}{4}\frac{C^2(\tau)}{S_1^{corr}(\tau)S_2^{corr}(\tau)}\right)^{-1}. \tag{6.25}$$

This equation allows us to accurately estimate η_1^S directly from the count rates measured in the experiment.

To estimate the **leakage** efficiencies $\eta_1^{D_\tau}$, we consider the coincidence rate $C^{BG}(\tau)$ we measure when the stationary interferometer arm is blocked. In this case — ignoring background and/or dark counts in the detectors — the only way that both detectors will click is if both photons travel to the sample via the delay arm, are transmitted by the sample, and then one photon makes D_1 click while the other makes D_2 click. Thus, in the limit $p_{E2PA} << 1$, the rate is given by:

$$C^{BG}(\tau) \approx 2N(T_{XS}^D)^2 \eta_1^{D_\tau} \eta_2^{D_\tau}. \tag{6.26}$$

Using this equation and Eq. (6.24), we find:

$$\eta_1^{D_\tau} = \eta_1^S \frac{T_{XS}^S}{T_{XS}^{D_\tau}} \frac{C^{BG}(\tau)}{C(\tau)}. \tag{6.27}$$

6.5.2 Count Renormalization with a Quadrant Photodiode

Fluctuations in the power and pointing direction of the pump laser are one major source of noise in our experiment. Because we have to measure the count rates $S_1^{corr}(0)$ and $S_1^{corr}(\mathcal{T})$ at different times, this leads to extra noise in our measurement of ΔS. An important step in our analysis procedure is normalizing the background-corrected count rates based on measured fluctuations in the pump laser. In this section we explain how we perform this normalization.

We monitor fluctuations in the pump laser by directing a portion of the pump beam onto a photodiode with an active area divided into four sections. When light is incident on the photodiode, a photocurrent is created by each of the four sections, proportional to the amount of light absorbed by that section. We can monitor three outputs from this photodiode: first, the sum of the signal over all four sections, q^{sum}, second, the difference between the signal from the bottom two sections and the top two sections, q^{bt}, and third the difference between the signal from the left and right sections, q^{lr}. The q^{sum} signal is proportional to the total power incident on the photodiode, and the q^{bt} and q^{lr} signals monitor changes in the up-down and left-right position of the incident light. Thus, we can monitor fluctuations in the pump laser power and pointing direction with this quadrant photodiode.

We assume that the background-corrected singles rate at D_1, S_1^{corr}, can depend quadratically on these pump-laser fluctuations, via the relation:

$$S_1^{corr}(\tau) = \beta_0^\tau + \beta_1^\tau q^{sum} + \beta_2^\tau q^{bt} + \beta_3^\tau q^{lr} + \beta_4^\tau (q^{sum})^2 + \beta_5^\tau (q^{bt})^2 + \beta_6^\tau (q^{lr})^2, \tag{6.28}$$

for some unknown coefficients β_i^τ for $i \in \{0, 6\}$. These coefficients are unknown, and we allow them to depend on the interferometer time delay τ.

If we know the β_i^τ coefficients, we can renormalize the measured $S_1^{corr}(\tau)$ rates using the above model, and predict what rates we **would have** measured if the pump laser parameters were identical for the measurements at zero ($\tau = 0$) and large ($\tau = \mathcal{T}$) time delays. We achieve this goal by predicting the β_i^τ coefficients with a linear least-squares fit.

During our data acquisition, each independent ‘zero-delay’ or ‘large-delay’ measurement actually consists of a set of measurements, performed at 14 different delay-arm motor positions. At each of these 14 motor positions, we perform five successive, independent measurements of the count rates and quadrant photodiode readings. We use one of these measurements (i.e. 20% of the data) as 'training data' which we fit to Eq. (6.28) to estimate the β_i^τ coefficients. We use these models to renormalize the other 80% of the data.

We perform our data analysis in chunks of m τ-delay measurements — this is how we average over m independent measurements and (using the Allan deviation as discussed in Section 6.6) calculate the optimal averaging time. We begin by defining the matrix Q^τ_{train}, which contains the quadrant photodetector readings for all the training data acquired in a chunk of m τ-delay measurements. Q^τ_{train} has $14m$ rows (corresponding to the $14m$ independent training-data measurements performed at τ-delay), and the entries of Q^τ_{train} encode the quadrant photodiode readings:

$$Q^\tau_{train} = \begin{pmatrix} 1 & q_1^{sum}(\tau) & q_1^{bt}(\tau) & q_1^{lr}(\tau) & (q_1^{sum}(\tau))^2 & (q_1^{bt}(\tau))^2 & (q_1^{lr}(\tau))^2 \\ \vdots & \vdots & \vdots & \vdots & \vdots & \vdots & \vdots \\ 1 & q_{14m}^{sum}(\tau) & q_{14m}^{bt}(\tau) & q_{14m}^{lr}(\tau) & (q_{14m}^{sum}(\tau))^2 & (q_{14m}^{bt}(\tau))^2 & (q_{14m}^{lr}(\tau))^2 \end{pmatrix}. \tag{6.29}$$

We also define a vector representing all $14m$ training-data measurements of the background-corrected singles rate in the measurement chunk:

$$\vec{S}^{corr}_{1,train}(\tau) = \begin{pmatrix} (S_1^{corr}(\tau))_1 \\ \vdots \\ (S_1^{corr}(\tau))_{14m} \end{pmatrix}, \tag{6.30}$$

and a vector containing the model parameters:

$$\vec{\beta}^\tau = \begin{pmatrix} \beta_0^\tau & \beta_1^\tau & \beta_2^\tau & \beta_3^\tau & \beta_4^\tau & \beta_5^\tau & \beta_6^\tau \end{pmatrix}^T. \tag{6.31}$$

We perform a linear least-squares fit of our model to the training data by calculating:

$$\vec{\beta}^\tau = \left((Q^\tau_{train})^T Q^\tau_{train}\right)^{-1} (Q^\tau_{train})^T \vec{S}^{corr}_{1,train}(\tau). \tag{6.32}$$

The remaining, (non-training) data from the chunk of m measurements can be arranged into the matrices Q^τ and vectors $\vec{S}_1^{corr}(\tau)$ — these are defined in a similar way as Q^τ_{train} and $\vec{S}^{corr}_{1,train}(\tau)$

except they each have four times as many rows, because there is four times as much non-training data as training data. Using our model, we can **predict** the count rates we would have measured given the quadrant photodiode readings, using:

$$\vec{S}_1^{pred}(\tau) = Q^\tau \vec{\beta}^\tau. \tag{6.33}$$

We can also predict the mean rate we would have measured if the zero-delay and large-delay measurements were performed with exactly the same pump laser parameters:

$$S_1^{mean}(\tau) = \overline{\frac{1}{2}\left(Q^0 + Q^{\mathcal{T}}\right)\vec{\beta}^\tau}. \tag{6.34}$$

Finally, we arrive at our definition for the renormalized, background-corrected count rate at D_1:

$$\vec{S}_1^{norm}(\tau) = \frac{\vec{S}_1^{corr}(\tau)}{\vec{S}_1^{pred}(\tau)} S_1^{mean}(\tau). \tag{6.35}$$

6.6 Results

After acquiring data, our goal is to find an accurate estimate of ΔS. We want to analyze the data in a way that is independent of as many systematic errors as possible. We begin by subtracting the background count-rate measurements from the count rates measured at D_1. We notice a correlation between the quadrant detector readings and the count rates, implying that our experiment is sensitive to instability of the pump beam. To account for this instability, we numerically fit a function of the quadrant detector outputs to the background-subtracted counts, and renormalize the counts based on this fit—full details of this procedure are in Section 6.5.2. This procedure allows us to account for and remove pump-laser noise that adds noise to the measured count rates. Finally, we calculate the change in singles rates—ΔS—from the background-subtracted, renormalized count rates at each delay.

We also perform an Allan deviation analysis on each dataset in order to estimate the uncertainty on our measurement of ΔS and to find the optimal total averaging time. To do this, we begin by dividing the total dataset into a series of subsets each representing the same total number of measurements. We apply the full analysis procedure from the above paragraph to each subset,

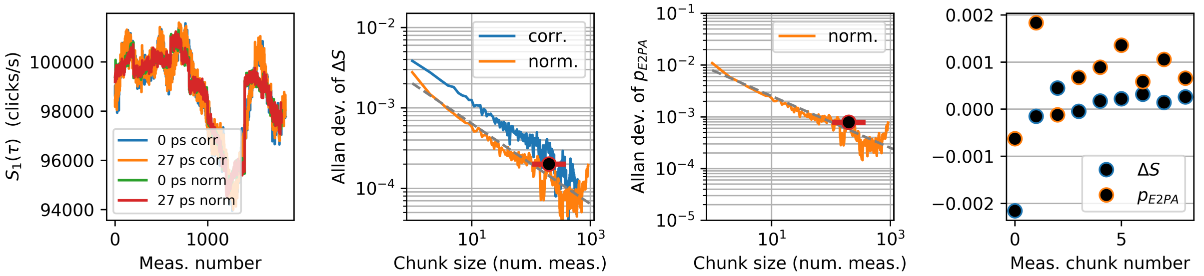

Figure 6.5: Example dataset, for 1.5×10^{-4} mol L^{-1} of ZnTPP in toluene. Plots 1-4 indicate the plots from left to right. Plot 1 shows count rates in D_1 as a function of measurement number. We plot the background-corrected count rates (corr) at both 0 ps and 27 ps interferometer delay. We also plot the count rates after renormalizing (norm) to minimize the impact of pump laser fluctuations which we monitor with the quadrant photodiode. Plot 2 shows the Allan deviation of ΔS as a function of the number of consecutive measurements we average over (i.e. the "chunk size"). The optimal averaging time (and corresponding minimum Allan deviation) is marked by the red point. The blue trace is the Allan deviation when we calculate ΔS with the background-corrected counts, and the orange is the measured Allan deviation when we calculate ΔS with the normalized counts. Our normalization procedure reduces the Allan deviation by roughly a factor of 3, indicating that this procedure successfully removes some of the noise caused by pump-laser fluctuations. Plot 3 shows the Allan deviation curve for our inference of p_{E2PA} (which we infer from our measurement of ΔS). The optimal averaging time (and corresponding Allan deviation) is marked by the red point. Plot 4 shows all measurements of ΔS and p_{E2PA} performed on this sample. For this measurement, the optimal averaging time was roughly 1/9 of the total time we collected data, and therefore we have nine independent measurements of both ΔS and p_{E2PA}. For this sample, there is no statistically significant indication that E2PA occurred.

resulting in a list of ΔS estimates from which we calculate an Allan deviation. We repeat this analysis for a variety of subset sizes. Because each sample was measured on a different day, and also because the stability of our setup varied slightly each day, the optimal averaging time varies from dataset to dataset.

We present an example dataset in Fig. 6.5. This data was taken with a 1.5×10^{-4} mol L^{-1} solution of Zinc-tetraphenylporphyrin (ZnTPP) in toluene. This dataset contains a total of 1842 independent measurements of the count rate at D_1 at each time delay (Fig. 6.5, plot 1). After background-correcting, normalizing, and averaging these counts, we calculate ΔS for a variety of different averaging times. Fig. 6.5, plot 2 shows the Allan deviation of the ΔS values as a function of averaging time, and we find the near optimal averaging time of 200 measurements gives an

Allan deviation of 0.0002 — we interpret this minimum Allan deviation as the uncertainty on our measurement of ΔS. For each sample we investigate, we independently characterize the modal overlap between the two interferometer arms with an interference measurement, and all of these measurements returned a visibility (V) greater than 95%. We also independently characterize the linear transmission efficiencies via each interferometer arm from the SPDC crystal to the cuvette, and find $T_{XS}^{S} = 36.4 \pm 2\%$ and $T_{XS}^{D} = 25.9 \pm 2\%$. Using these efficiencies and conservatively estimating $V = 0.95$, we use Eq. (6.20) (a corrected form of Eq. (6.2) that makes fewer assumptions in its derivation) to infer the probability that any pair of photons that reaches the sample is absorbed via E2PA, p_{E2PA}. We estimate the uncertainty on our measurement of p_{E2PA} by calculating the Allan deviation (Fig. 6.5, plot 3). Since this dataset has a total of 1842 measurements, and we found it is near optimal to average over subsets of 200 measurements, this dataset contains nine independent measurements of ΔS and p_{E2PA}, and these are plotted in Fig. 6.5, plot 4. The remaining 17 datasets are presented in Appendix H.

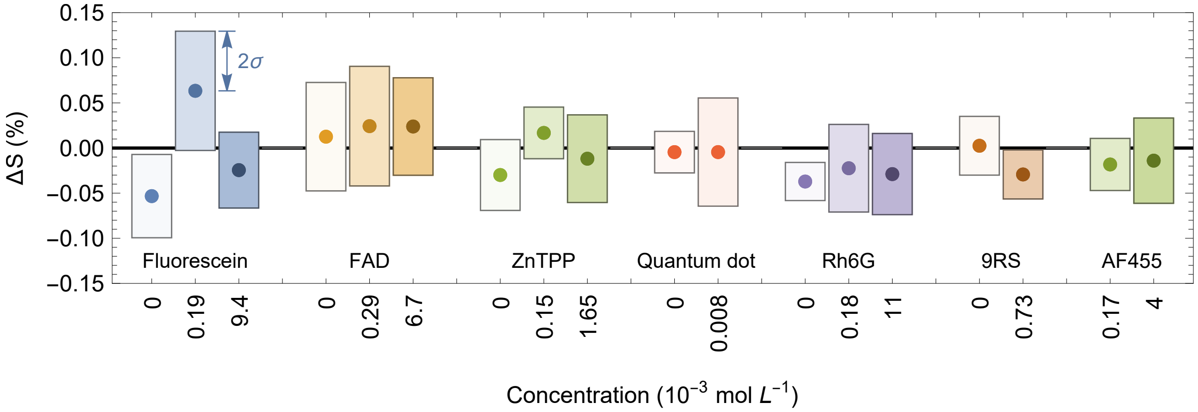

Figure 6.6: Summary of measured change in transmittance, ΔS, for all seven samples. The samples were measured at various concentrations, including some measurements of just the solvent (indicated with solution concentration set to 0). For all samples measured, we do not measure any statistically significant change in the count rate at detector D_1 when we vary the time delay in the interferometer from 0 ps to 27 ps. The error bars are set by two times the Allan deviation (2σ for $\approx$ 95% confidence that the real value lies within the error bars) for the selected averaging chunk size of each dataset.

In Fig. 6.6 we present the values of ΔS for all our datasets. We performed 18 independent data runs for 18 independent samples. The samples consist of 1.9×10^{-4} mol L^{-1} and 9.4×10^{-3} mol L^{-1}

fluorescein in pH 11 water, 2.9×10^{-4} mol L^{-1} and 6.7×10^{-3} mol L^{-1} flavin adenine dinucleotide (FAD) in phosphate buffered saline, 1.5×10^{-4} mol L^{-1} and 1.65×10^{-3} mol L^{-1} ZnTPP in toluene, 8×10^{-6} mol L^{-1} Qdot ITK carboxyl quantum dot 605 in borate buffer, 1.8×10^{-4} mol L^{-1} and 1.1×10^{-3} mol L^{-1} rhodamine 6G (Rh6G) in methanol, 7.3×10^{-4} mol L^{-1} of the benzodithiophene derivative "9R-S" in chloroform, 1.7×10^{-4} mol L^{-1} and 4.0×10^{-3} mol L^{-1} 1, 3, 5-triazine-based octupolar molecule "AF455" in toluene and each solvent. The details on sample preparation are in Appendix B. The solvent data runs are listed with solution concentration set to zero. For each dataset we find that the values of ΔS and p_{E2PA} show no statistically significant difference from zero.

In Table 6.1 we summarize the results for all our datasets. The samples, their C2PA cross sections from literature (σ_C) and an estimate for their entangled two-photon absorption cross section (σ_E^{est}) are shown. The estimate uses the probabilistic model (Eq. (2.11)). The measured sample concentrations (c), average detection efficiencies on detector 1 (η_1^S), values of ΔS, p_{E2PA} and upper bounds on the E2PA cross section (σ_E^{UB}, found using Eq. 6.21) are listed. The σ_E^{UB} values range from 3.1×10^{-22} to 6.6×10^{-19} cm^2 absorber^{-1}. These values are 5-8 orders of magnitude larger than the σ_E^{est} values, which is an estimate for the measurement sensitivity increase necessary to observe a signal.

6.7 Conclusion

In this chapter, we presented a sensitive transmittance-based E2PA measurement system. We designed a measurement technique capable of detecting changes in transmittance due only to E2PA, rather than one-photon loss mechanisms. We designed an interferometer to measure the difference in the singles rate at detector 1 at zero delay and a very large delay. These two delay positions represent states in which the E2PA rate is maximized and minimized (effectively zero), respectively. The one-photon loss between the SPDC crystal and detector 1 in these two states was kept identical. We corrected the count rate for leakage of photons from the delay arm into detector 1 and normalized our counts based on the pointing and power stability of our pump laser. These

Table 6.1: Summary of literature C2PA cross sections (σ_C), estimates for the E2PA cross sections (σ_E^{est}) (based on Eq. (2.11) using $T_e =$ 153 fs and $A_e = 2.1\,\mu\mathrm{m}^2$), measured sample concentrations (c), average detection efficiencies on detector 1 (η_1^S), change in transmittance (ΔS), probability that any pair that reaches the sample is absorbed via E2PA (p_{E2PA}) and E2PA cross-section upper bounds (σ_E^{UB}).

Sample	σ_C^{lit} [Ref.] (GM)	$\sigma_E^{\mathrm{est}} \times 10^{29}$ (cm^2 absorber^{-1})	$c \times 10^3$ (mol L^{-1})	η_1^S (%)	ΔS (%)	p_{E2PA} (%)	$\sigma_E^{\mathrm{UB}} \times 10^{21}$ (cm^2 absorber^{-1})
Fluorescein	13 ± 4 [19]	4.0 ± 1.2	0	5.99	-0.053 ± 0.042	-0.211 ± 0.166	
			0.190 ± 0.005	6.17	0.063 ± 0.033	0.246 ± 0.130	44
			9.4 ± 0.2	6.40	-0.024 ± 0.030	-0.099 ± 0.118	0.42
FAD	2.1 [54]	0.65	0	6.30	0.013 ± 0.030	0.054 ± 0.118	
			0.29 ± 0.01	6.69	0.024 ± 0.030	0.098 ± 0.118	19
			6.7 ± 0.5	7.73	0.024 ± 0.034	0.096 ± 0.133	0.90
ZnTPP	20 [53]	6.2	0	7.29	-0.030 ± 0.027	-0.122 ± 0.106	
			0.15 ± 0.01	6.55	0.017 ± 0.020	0.070 ± 0.079	25
			1.65 ± 0.10	6.89	-0.012 ± 0.030	-0.042 ± 0.118	2.4
Qdot 605	46000 ± 13000 [19]	14000 ± 4000	0	7.30	-0.005 ± 0.015	-0.018 ± 0.059	
			0.0080 ± 0.0005	5.05	-0.004 ± 0.040	-0.019 ± 0.159	660
Rh6G	51 ± 14 [19]	16 ± 4	0	6.08	-0.037 ± 0.020	-0.146 ± 0.079	
			0.18 ± 0.01	5.43	-0.022 ± 0.040	-0.083 ± 0.159	29
			11 ± 1	4.90	-0.029 ± 0.026	-0.113 ± 0.103	0.31
9R-S	22 ± 6 [19]	6.8 ± 1.9	0	5.02	0.003 ± 0.020	0.013 ± 0.079	
			0.73 ± 0.04	7.08	-0.029 ± 0.014	-0.111 ± 0.055	2.5
AF455	660 ± 180 [19]	210 ± 60	0.17 ± 0.01	5.04	-0.018 ± 0.017	-0.072 ± 0.068	13
			4.0 ± 0.2	6.41	-0.018 ± 0.030	-0.057 ± 0.118	0.98

techniques provided a sensitivity to changes in transmittance ΔS of 0.02-0.05%.

We performed measurements on seven independent samples at multiple concentrations and measured no statistically significant change in transmittance. We set upper bounds on the E2PA cross sections for the absorbers in the range $10^{-22} - 10^{-19}$ cm^2 absorber^{-1}. For four of the studied absorbers, E2PA cross sections have been published before [49, 53, 47, 54, 55, 48]. Our upper bounds are lower than these cross sections by factors in the range of $\approx 6 - 10^4$.

We find that transmittance measurements are less sensitive than fluorescence measurements. After optimizing each technique for maximum sensitivity, our transmittance measurements upper bounds are typically three orders of magnitude higher than those for our fluorescence measurements (Chapter 5). The higher sensitivity is a result of the background-free nature of fluorescence measurements. This reduces the noise and thus the minimum signal one can detect. However, some advantages do exist for transmittance measurements as discussed in Chapter 2 Section 2.5. Complicated variations of E2PA transmittance measurements could be designed to increase the sensitivity, however a many-orders-of-magnitude increase is not likely.

Chapter 7

A Toluene-Filled Hollow-Core-Fiber Platform for Two-Photon Absorption Measurements

7.1 Introduction

In our first fluorescence experiment (Chapter 5) we measured two-photon excited fluorescence (2PEF) from a sample contained in a cuvette. We measured both classical two-photon absorption (C2PA) and entangled two-photon absorption (E2PA) in the same setup under nearly identical conditions. In this chapter, we present a new platform for 2PEF measurements similar to that presented in Ref. [88], which was used for C2PA, and in Ref. [89], which was used for Raman spectroscopy. Here we confine a sample (two-photon absorbing molecules in solution) in a hollow-core fiber. We focus the excitation beam into the fiber to excite the two-photon absorbing molecules. The molecules emit fluorescence and some of that light is guided back out of the fiber and can be detected.

The benefit of this scheme is illustrated in Fig. 7.1. In the cuvette-based approach, light is focused in free space to a waist w_0 and expands quickly. The expansion is characterized by the Rayleigh range z_R. The parameter z_R scales quadratically with w_0, thus if one wants to increase the beam intensity at the focus by decreasing w_0, that intensity is maintained over a shorter distance z_R. In contrast, in a fiber-based approach, light is focused into a fiber with waist w_0 and that beam size is maintained over long lengths because of low-loss fiber confinement. A high intensity of light is advantageous for 2PA because two photons must be spatially and temporally overlapped at a molecule in order for the absorption process to occur. Maintaining that intensity over long

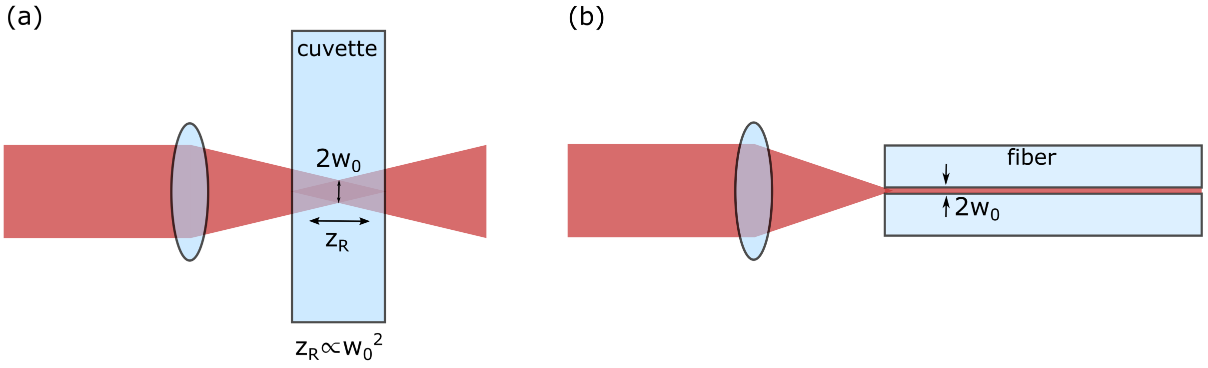

Figure 7.1: The advantage of fiber confinement for 2PA measurements. Illustration of (a) a conventional cuvette-based and (b) a fiber-based measurement. In the cuvette-based approach, the light is focused in free space to a beam waist w_0. The Rayleigh range z_R characterizes the distance over which the beam size is $\leq \sqrt{2}w_0$. When w_0 is decreased so is z_R, thus high intensity beams can only be maintained over short distances. In the fiber-based approach, the light is focused into fiber with waist w_0 and maintained over long lengths because of low-loss fiber confinement.

lengths increases the likelihood that the two photons will excite a molecule because those photons will encounter more molecules.

In this chapter, we discuss the conditions we selected for low-loss fiber confinement. Then, we present our experimental setup. We then model our experiment in order to calculate a C2PA cross section from our measurements. Afterwards, we present characterizations of the fiber platform and discuss our data acquisition technique. Finally, we present our results for the molecule AF455.

7.2 Light Guidance

In this experiment we seek to confine both the sample, excitation photons and fluorescence photons along the length of the fiber. In order to achieve broadband guidance, we designed our fiber for index guidance. In index guidance, all light traveling in the core and incident onto the core-cladding interface at an angle (with respect to the normal to the interface) equal to or greater than the critical angle, $\theta_c = \arcsin(n_{\text{clad}}/n_{\text{core}})$ where n_{clad} and n_{core} are the indices of refraction of the cladding and core of the fiber, is guided through the fiber because of total internal reflection. The critical angle is only real if the index of the cladding is smaller than the index of the core. To achieve this criteria, we use a standard capillary tubing with a silica cladding and fill the hollow core with toluene. The critical angle under these conditions is real for both the excitation and fluorescence wavelength regions.

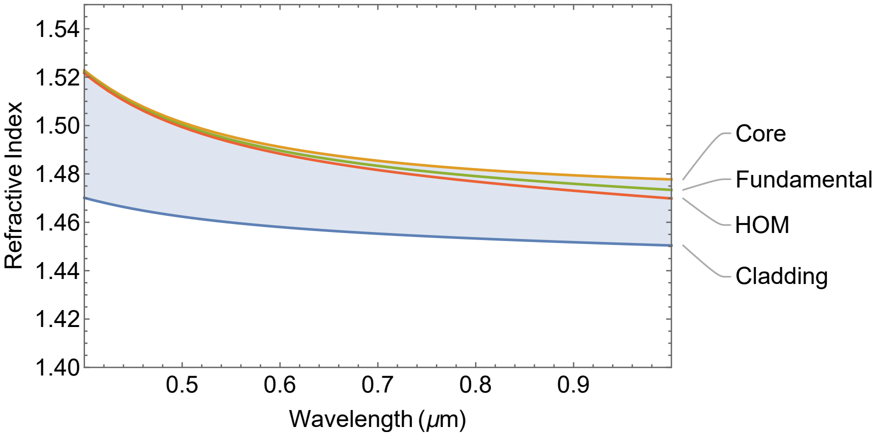

Figure 7.2: Refractive index as a function of wavelength for the relevant media and first two modes of guided light. The toluene-filled core (orange) and silica cladding (blue) indices are shown. The mode indices for the fundamental (green) and the first higher-order mode (HOM, red) are shown. Additional modes can propagate through the filled fiber with mode indices filling the blue shaded region between the HOM and cladding indices.

The refractive indices as a function of wavelength for the toluene core and silica cladding are plotted in Fig. 7.2. The range of indices lying between the core and cladding allows for the propagation of multiple modes of light. The effective index of refraction of the fundamental and first higher-order modes are shown and are calculated using Ref. [90]. We can calculate the number of modes that can propagate along the fiber using the V-number,

$$V(\lambda) = \frac{\pi d}{\lambda}\sqrt{n_{\text{core}}^2(\lambda) - n_{\text{clad}}^2(\lambda)}. \tag{7.1}$$

The number of modes that can propagate at a particular wavelength λ is then $V(\lambda)^2/2$. For the excitation wavelength of 810 nm, ≈ 16 modes can propagate. For the fluorescence wavelengths of AF455 in toluene, which is peaked at 451 nm, ≈ 80 modes can propagate. In the ideal case, all of the light would remain in the fundamental mode because this mode is less lossy, has lower dispersion and has a Gaussian spatial profile. All of these characteristics will increase the likelihood that 2PA can occur.

In addition to toluene allowing broadband guidance of light in a fiber made of silica, toluene also has a low absorption coefficient [91] at the excitation (0.0030 cm^{-1}) and fluorescence (0.0039 cm^{-1}) wavelengths. This is a necessary condition otherwise the long length of the fiber will add little to no benefit since all the light would be absorbed after a short distance. For comparison, water has an absorption coefficient that is about one order of magnitude larger at 810 nm (0.0209 cm^{-1} [91]).

7.3 Experimental Setup

To prepare the fiber, we first cut a clean facet on both ends of the fiber to minimize the loss that occurs when coupling light into fiber. We use a custom-built coil heater to remove about 20 mm of the polyamide coating from each end of the fiber. Next we cleave the fiber ends in the regions where the coatings have been removed. We inspect the ends under a digital microscope to ensure that the cut looked smooth and to check for particle contamination. The fiber ends are placed in a tubing sleeve to prevent breakage and to allow for simple attachment to the fiber adapters in the setup. Images of the fiber under a digital microscope (Keyence VHX 7000) are shown in Fig. 7.3(a)-(b).

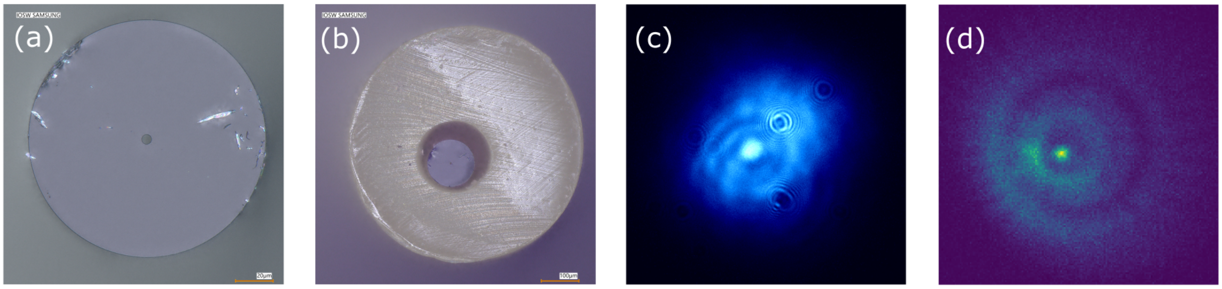

Figure 7.3: Digital microscope images of one end of (a) the capillary and (b) the capillary inside of the tubing sleeve. (c) sCMOS image of the 810 nm excitation laser guided through the capillary. (d) EMCCD image of the fluorescence from AF455 guided out of the capillary. The last two images are taken in the image plane of the fiber face. Some features of the tube and tubing sleeve are visible in both images as described in Section 7.5.

The fiber and tubing sleeves are secured into the custom-built fiber adapters (see Appendix J for technical drawings). One fiber adapter is connected with PEEK tubing to a syringe placed into a syringe pump. This pump is used to fill the fiber. Both fiber adapters are connected with PEEK tubing to valves that serve as drainage ports. The fiber adapters are fitted for fused silica optical windows, which are sealed onto the front for coupling light into and out of fiber. These windows also serve as view ports to check if fluid has flowed through the fiber.

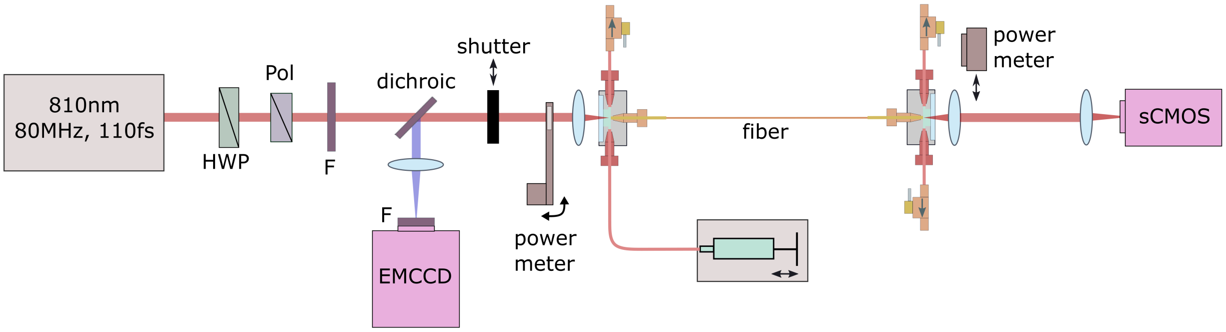

Figure 7.4: Schematic of the experimental setup. The 810 nm laser is directed through a half-wave plate (HWP), polarizer (pol) and neutral density filters (F) to control the power. The beam is then sent through a dichroic and focused into a toluene-filled hollow-core fiber held in two fiber adapters at either end with fittings. Solvent or a solution is pumped into the fiber using a syringe and syringe pump connected by PEEK tubing to one of the fiber adapters. Fluid can be drained out of the system by opening the valves connected to either fiber adapter. Light transmitted through the fiber can be detected on a power meter or an sCMOS camera. A fraction of the fluorescence generated inside the fiber is directed out of the fiber in the direction of the dichroic, where it is reflected and focused onto the EMCCD camera. Scattered light is filtered out (F). The power before the fiber can be measured with a power meter that flips in and out of the beam. A motorized shutter can be used to block the beam and take a background measurement.

The microfluidic and optical setup is shown in Fig. 7.4. Here we give a brief overview of the setup, a thorough description of the components is given in Appendix I. An 810 nm, 110 fs pulsed laser is directed through a half-wave plate (HWP), polarizing beamsplitter (PBS) and neutral density filters (F) for control over the power. The light is directed through a dichroic beamsplitter and focused into the 5-μm-diameter-core fiber. Light that is transmitted through the 37-cm-long fiber can be detected on a power meter or imaged on an scientific Complementary Metal–Oxide–Semiconductor (sCMOS) camera. The power before the fiber can be measured with a power meter that flips into the beam path. Any fluorescence generated inside of the fiber and guided out in the direction opposite of the 810 nm beam is reflected at a dichroic beamsplitter and focused onto an Electron-Multiplying Charge-Coupled Device (EMCCD) camera. Filters (F) remove any scattered 810 nm light. The sample AF455 is chosen for our measurements due to its large C2PA cross section at 810 nm and its solubility in toluene. The details on sample preparation are in Appendix B.

7.4 Calculating a C2PA Cross Section

In a similar manner to that shown in Chapter 5 Section 5.5, we can model the C2PEF signal detected on the camera, F_C (cnt s^{-1}), as

$$F_C = g \int_0^l N_C(z) \int_{\lambda_i}^{\lambda_f} \gamma(z,\lambda)\kappa(\lambda)\Phi(\lambda) d\lambda dz, \tag{7.2}$$

where g (pulses s^{-1}) is the pulse repetition rate, l (cm) is the length of the fiber, $N_C(z)$ (excitations cm^{-1} pulse^{-1}) is the number of excitations per infinitesimal length of fiber dz (cm) per pulse, λ_i and λ_f (nm) are wavelengths chosen such that the integral extends over the entire emission spectrum of the sample, $\gamma(z,\lambda)$ (cnt photon^{-1}) is the component transmission efficiency, $\kappa(\lambda)$ is the collection efficiency and $\Phi(\lambda)$ (photon excitation^{-1} nm^{-1}) is the differential fluorescence quantum yield. A proper normalization of quantum yield is used such that $\Phi = \int_0^\infty \Phi(\lambda) d\lambda$ gives the value published in literature for the total quantum yield of the fluorophore.

From this equation, we find that it is advantageous to increase the length of the fiber for all z such that $N_C(z)\gamma(z,\lambda) > 0$. This product never drops below zero, but can be zero if the photons are dispersed in time far enough that two photons are never temporally overlapped at that position z, or if the photon loss along the length l is 100% for either the excitation photons or the fluorescence photons, or some combination of both leading to a negligible product $N_C(z)\gamma(z,\lambda) \approx 0$. In this experiment we try to make l long enough that $N_C(l)\gamma(l,\lambda) \approx 0$, so that we can achieve the highest signal at a given photon flux. We would like the sensitivity improvement relative to our prior fluorescence technique (Chapter 5) to be as high as possible.

Here we define the collection efficiency as the fraction of light that can be collected by the fiber and directed out in the direction of the detector. Here we assume that the fluorescence is emitted isotropically and that the fraction of that light collected can be described by the solid angle of a cone with apex angle $2(90° - \theta_c)$, where θ_c is the critical angle (Section 7.2). Then we can write,

$$\kappa(\lambda) = \frac{1}{2}\left[1 - \cos\left(\arcsin\left(\frac{n_{\text{core}}^2(\lambda) - n_{\text{clad}}^2(\lambda)}{n_{\text{core}}(\lambda)}\right)\right)\right], \tag{7.3}$$

where $n_{\text{core}}(\lambda)$ and $n_{\text{clad}}(\lambda)$ are the indices of refraction of the core and cladding materials (toluene and silica) at the wavelength of the fluorescence. The component transmission efficiency describes the transmission efficiency of fluorescence from its point of generation z (cm) to the detector, under the assumption that it is directed out of the fiber. It takes into account all the loss mechanisms from various optical components and the media the light propagates through. We define this quantity as

$$\gamma(z, \lambda) = \text{Exp}\left(-(a_{\text{sol}}(\lambda) + \epsilon_{\text{sam}}(\lambda)c + \mu(\lambda))z\right)\mathcal{T}_{\text{window}}(\lambda)\mathcal{T}_{\text{lens}}(\lambda)\mathcal{R}_{\text{dichroic}}(\lambda)\mathcal{T}_{\text{lens}}(\lambda)\mathcal{T}_{\text{filter}}(\lambda)\text{QE}(\lambda), \tag{7.4}$$

where $a_{\text{sol}}(\lambda)$ (cm^{-1}) is the absorption coefficient of the solvent, $\epsilon_{\text{sam}}(\lambda)$ (L mol^{-1} cm^{-1}) is the extinction coefficient of the sample, c (L mol^{-1}) is the concentration of the sample, $\mu(\lambda)$ (cm^{-1}) is the scattering coefficient of the fiber, $\mathcal{T}$ describes the transmittance of an optic, $\mathcal{R}$ describes the reflectance of an optic and QE (cnt photon^{-1}) describes the quantum efficiency of the camera.

We describe the number of excitations per infinitesimal length dz per pulse as

$$N_C(z) = \frac{1}{2}\sigma_C n \int_{-1/2g}^{1/2g}\int_{-\infty}^{\infty}\int_{-\infty}^{\infty}\phi(x, y, z, t)^2 dx dy dt \tag{7.5}$$

where σ_C (1 GM = 10^{-50} cm^4 s photon^{-1} fluorophore^{-1}) is the C2PA cross section, n (fluorophores cm^{-3}) is the number density of the fluorophores and $\phi(x, y, z, t)$ (photons cm^{-2} s^{-1}) is the photon flux of the laser beam. The factor of 1/2 carries units of excitations per photons absorbed. The temporal and transverse spatial profiles of the laser beam are approximated by Gaussian distributions. The transverse spatial profile of the light inside the fiber will not fit a Gaussian distribution if it is confined into the higher-order modes of the fiber, but in this calculation we make a few approximations based on the assumption that all the light is in the fundamental mode. Assuming the laser is always on, $\phi(x,y,z,t)$ takes the form

$$\phi(x,y,z,t) = \phi_0(z)\mathrm{Exp}\left(-4\mathrm{ln}2\left(\frac{x^2}{\Delta x_0^2} + \frac{y^2}{\Delta y_0^2}\right)\right)\sum_{i=-\infty}^{\infty}\mathrm{Exp}\left(-4\mathrm{ln}2\frac{(t+i/g)^2}{\tau(z)^2}\right), \tag{7.6}$$

where $\phi_0(z)$ (photons cm^{-2} s^{-1}) is the peak photon flux as a function of z, $\tau(z)$ (fs) is the FWHM pulse duration and Δx_0 (cm) and Δy_0 (cm) are the FWHM beam widths. The peak photon flux has z dependence because of loss and dispersion in the fiber. We can define the average photon rate $Q(z)$ in terms of the photon flux,

$$Q(z) = g\int_{-1/2g}^{1/2g}\int_{-\infty}^{\infty}\int_{-\infty}^{\infty}\phi(x,y,z,t)dxdydt = \frac{W(z)}{h\nu} \tag{7.7}$$

where $W(z)$ (W) is the average power of the beam as a function of z and $h\nu$ (J) is the average energy of an incident photon. We can also write the power in a form to show its dependence on propagation losses in fiber,

$$W(z) = W_0\mathrm{Exp}\left(-(a_{\mathrm{sol}}(\lambda_e) + \epsilon_{\mathrm{sam}}(\lambda_e)c + \mu(\lambda_e))z\right) \tag{7.8}$$

where W_0 (W) is the average power at $z = 0$, $\lambda_e = 810$ nm and $\epsilon_{\mathrm{sam}}(\lambda_e) \approx 0$. The parameter W_0 is related to the power measured at the input of the fiber W_{in} (W) by $W_0 = \eta_C W_{\mathrm{in}}$ where η_C is the coupling efficiency into fiber. The power measured at the output of the fiber W_{out} is a good estimate for $W(l)$. We can solve for the $\phi_0(z)$ using Eq. 7.7 by integration of the flux over x, y and t,

$$\phi_0(z) = \left(\frac{4\mathrm{ln}(2)}{\pi}\right)^{3/2}\frac{W(z)}{h\nu g\Delta x_0\Delta y_0\tau(z)}. \tag{7.9}$$

The pulse duration has z dependence because of dispersion and can be described by

$$\tau(z) = \sqrt{\tau_0^4 + (4\mathrm{ln}2)^2(D_0+\beta z)^2}/\tau_0 \tag{7.10}$$

where D_0 is the group delay dispersion (GDD) accumulated by the pulse before the fiber and β is the total group velocity dispersion (GVD) of the fiber.

Now we can rewrite Eq. (7.2) using these equations as

$$F_C = \sqrt{2}\left(\frac{\mathrm{ln}(2)}{\pi}\right)^{3/2}\frac{\sigma_C n W_0^2}{g(h\nu)^2\Delta x\Delta y}\int_0^l\frac{\mathrm{Exp}(-2(a_{\mathrm{sol}}(\lambda_e)+\mu(\lambda_e))z)}{\tau(z)}\int_{\lambda_i}^{\lambda_f}\gamma(z,\lambda)\kappa(\lambda)\Phi(\lambda)d\lambda dz. \tag{7.11}$$

Then we can solve for the C2PA cross section

$$\sigma_C = \frac{1}{\sqrt{2}}\left(\frac{\pi}{\ln(2)}\right)^{3/2}\frac{g(h\nu)^2\Delta x\Delta y}{n}\frac{F_C/W_0^2}{\int_0^l \mathrm{Exp}(-2(a_{\mathrm{sol}}(\lambda_e)+\mu(\lambda_e))z)/\tau(z)\int_{\lambda_i}^{\lambda_f}\gamma(z,\lambda)\kappa(\lambda)\Phi(\lambda)d\lambda dz}. \tag{7.12}$$

All the parameters in Eq. 7.12 are known through experiments or simulations. The parameter τ_0 is measured using a SwampOptics Grenouille 8-50-USB, D_0 is measured, β is estimated using Comsol Multiphysics Simulation software, g and $h\nu$ are specified by the laser manufacturer, n is measured, $k(\lambda)$ is calculated, Δx_0 and Δy_0 are estimated, $a_{\mathrm{sol}}(\lambda)$ is from literature [91], $\mu(\lambda)$ is determined from scattering measurements (Section 7.5), $\Phi(\lambda)$ is known from published measurements [79] and F_C/W_0^2 (cnt s^{-1} μW^{-2}) is the fit to our experimental C2PEF data. The parameter $\gamma(\lambda)$ is calculated based on optics' specifications, our scattering measurements and the published extinction coefficient and spectra of AF455 [17].

7.5 Experimental Characterization

In this section we discuss the experimental characterizations we performed in order to derive a C2PA cross section using Eq. (7.12). First, we discuss the transmission efficiency of the fiber. Then, we discuss the characterization of propagation losses of the fiber by imaging fiber scatter. Afterwards, we present images of the excitation and fluorescence light at the fiber facet for identification of the mode content of the fiber. Finally, we discuss our characterization of the setup's dispersion.

We maximize the transmission of the 810 nm light through the fiber by using mirrors to walk the beam and adjusting the position of the focusing lens before the fiber. We measure the power before and after the fiber, and the ratio of the power transmitted out to the power sent in is what we call our transmission efficiency ($\frac{W_{\mathrm{out}}}{W_{\mathrm{in}}}$). This efficiency accounts for coupling, scattering and absorption losses. The best alignment resulted in about $> 55\%$ transmission efficiency. However, during our measurements the transmission efficiency was $\approx 40\%$ but varied from dataset to dataset.

We characterize the loss of light along the length of the fiber by imaging the scattering. The intensity of the scattering is proportional to the power $W(z)$, and thus should exponentially decay according to Eq. (7.8) with λ_e replaced with the wavelength of the light propagating through the fiber.

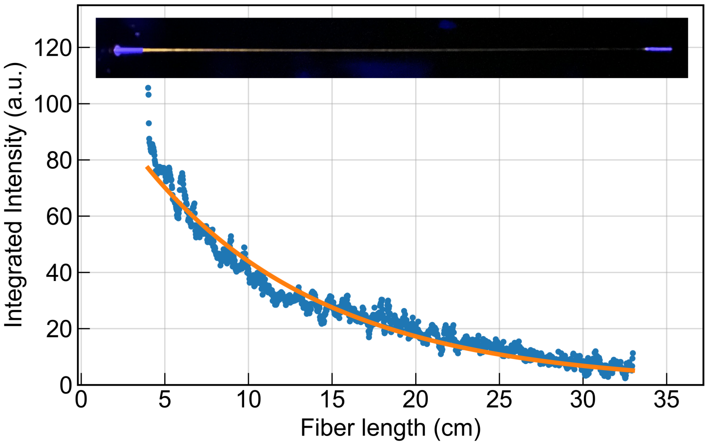

Figure 7.5: An image of the scatter from the alignment laser (inset) and a plot of the integrated intensity (blue) of the scatter as a function of fiber length. The intensity of the scatter is higher at the ends due to secondary reflections off the fiber tubing sleeves and fittings. These regions are removed from the plotted data. The fiber is not visible inside of the fittings and fiber adapters. The integrated intensity is fit (orange) to an exponential decay.

With only the solvent in the fiber ($c = 0$), we send a 458 nm alignment laser through the fiber and image the scattering on a smart phone camera using long exposure settings as shown in Fig. 7.5. The image is integrated vertically to find an integrated intensity as a function of fiber length. The intensity is fit to the exponential in Eq. (7.8) to derive $a_{\text{sol}}(458\,\text{nm}) + \mu(458\,\text{nm}) = 0.0093\ \text{cm}^{-1}$. This corresponds to a loss of 96.9% of the light along the length of the fiber. We take the same measurement with 750 nm (a visible wavelength close to our excitation wavelength) light and the data does not fit to an exponential. We believe that $a_{\text{sol}}(750\,\text{nm}) + \mu(750\,\text{nm})$ is not large enough to measure this way. As mentioned in Section 7.2, the values of $a_{\text{sol}}(\lambda)$ are known. From publications $a_{\text{sol}}(750\,\text{nm}) = 0.0036\ \text{cm}^{-1}$ and $a_{\text{sol}}(810\,\text{nm}) = 0.0030\ \text{cm}^{-1}$. If we set $\mu(750\,\text{nm}) = \mu(810\,\text{nm}) = 0$, we find that these absorption coefficients correspond to a loss of 12.5% and 10.5%, respectively, of the light along the length of the fiber. Considering with our best alignment $\frac{W_{\text{out}}}{W_{\text{in}}} > 55\%$, and that some fraction of that light is lost due to the coupling efficiency η_C in addition to the 10.5% absorption loss, we find it reasonable to estimate $\mu(810\,\text{nm}) \approx 0$. This low scattering loss is consistent with the light primarily occupying the fundamental mode of the fiber.

We image the 810 nm light at the output of the fiber using two lenses and the sCMOS camera, as shown in Fig. 7.3(c). In this image, the bright larger and smaller concentric circles are the imaged fiber cladding outer diameter and the outline of the core modes, respectively. The larger elliptical shape is likely formed by light guided through the inside of the tubing sleeve as can be seen by comparison to the digital microscope image in Fig. 7.3(b). Thus, we find that the light occupies some lower intensity cladding and tubing sleeve modes in addition to the core modes.

The fluorescence is collected at the front of the fiber using the lens optimized to focus 810 nm light into the fiber, which roughly collimates the visible fluorescence. The light is reflected at the dichroic beamsplitter, and another lens focuses the image plane of the fiber facet onto the EMCCD, as shown in Fig. 7.3(d). In this image, the high intensity bright spot is from fluorescence guided through the core. Light forms an elliptical ring around this bright spot, and is likely from light guided through the core of the tubing sleeve as can be seen by comparison to the digital microscope image in Fig. 7.3(b). A larger circular ring of light surrounds that elliptical ring, and is likely from light guided through the cladding of the tubing sleeve. Thus, there are many modes occupied by the fluorescence as predicted by the calculation of a large number of modes in Section 7.2.

To measure the GDD D_0 accumulated by the pulse as it propagates through the optical setup, we use the GDD tuning function of the Chameleon Discovery laser. We increase the dispersion compensation in increments and take C2PA measurements at each step. The step with the maximum C2PA signal corresponds to the value at which the GDD is optimally compensated at the input of the fiber. We measure $D_0 \approx 1300$ fs^2, which agrees with an independent calculation of the GDD in the setup. To determine the fiber GVD β, a Comsol simulation is used to model the filled fiber. The low-order modes are solved for. For the fundamental mode, β is identical to β of toluene, thus there are no contributions from waveguide dispersion. However, for higher order modes it's likely that β is affected by waveguide dispersion. These higher-order modes are not considered in the calculations of Section 7.4.

7.6 Data Acquisition

In the Section we discuss the camera settings used for data acquistion, the characterization of camera baseline and dark count rates, the operations that go into measuring a single frame of data and the conversion of a camera signal to a detected fluorescence rate.

To determine which camera settings were optimal, we wrote a script to calculate the signal to noise ratio (SNR) of our measurements at various EMCCD settings based on our expected signal levels. We determined the optimum camera settings to be: electron multiplying (EM) output amplifier, EM gain set to 30, preamplifier set to 1, 1 MHz horizontal shift rate, 10 s integration time and 24x24 binned pixels (a superpixel). Although the integration time could be increased further to increase the SNR, we found that clock-induced charge (CIC) occurred more frequently at those integration times. Any CIC was removed from the data. To speed up frame readout on the EMCCD, a pixel region of interest (ROI) is selected and only those pixels are read out. To select a ROI, the fluorescence was imaged at a relatively high power and the region with significant photon counts was selected.

Before datasets are acquired, the baseline and dark count rates of the camera are characterized. Both are characterized with the built-in camera shutter closed. The baseline measurements are taken at the minimum integration time of the camera. The dark rate measurements are taken at the 10 s measurement integration time. From each of these characterization datasets we calculate an average value and uncertainty using an Allan deviation analysis like that shown in Fig. 7.6 for the fluorescence rate. A typical baseline measurement in our ROI yields 570.4 ± 1.0 ADU pixel^{-1} and a typical dark rate measurement in our ROI yields 2.09 ± 0.05 electrons s^{-1} pixel^{-1}.

Each measurement frame consists of a background and a signal measurement. The difference between a background and a signal measurement being that the shutter (Fig. 7.4) is closed during a background measurement. The power meter after the fiber is used to measure the power before each signal measurement and is used for plotting the power dependence of the signal (Fig. 7.7). The number of measurements done at each power varied. As the power decreased, the signal decreased and thus we performed more measurements to lower the uncertainty.

To calculate the fluorescence rate F_C in cnt s^{-1} detected by the camera, the pixels of interest are integrated over to determine the camera signal N (ADU). We converted N to a count rate using,

$$F_C = \frac{NS}{GT}, \tag{7.13}$$

where S (electrons ADU^{-1}) is the CCD sensitivity for the selected output amplifier and preamplifier, G (electrons cnt^{-1}) is the EM gain and T (s) is the integration time.

7.7 Results

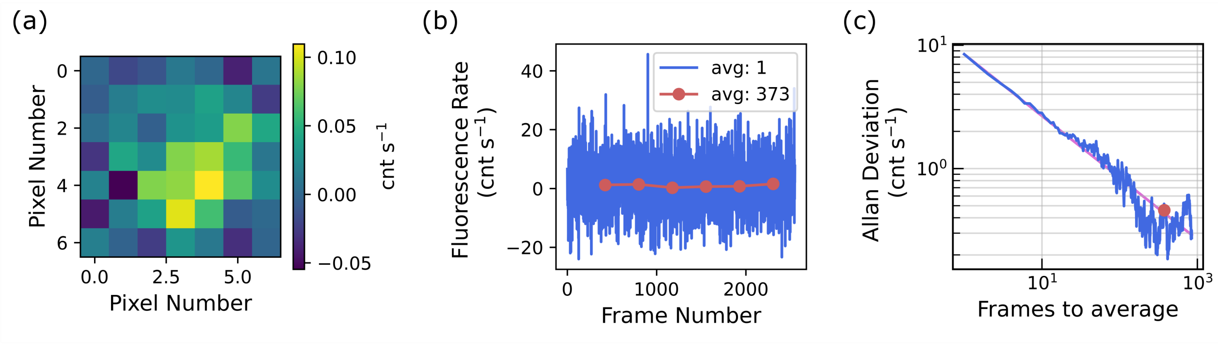

Figure 7.6: Example dataset for 21.8 nW excitation power. (a) The average background subtracted image is shown for the 7x7 superpixel region of interest. (b) The fluorescence count rate calculated from each frame's background subtracted imaged is plotted in blue vs frame number. Averaging in chunks of 373 frames is shown in red which gives a photon rate of 0.98 cnt s^{-1}. (c) The Allan deviation of the photon rate is calculated as a function of chunks of frames used to average. A $1/\sqrt{N}$ (where N is the number of frames) line is used to guide the eye to the best number of frames to average. The value used in the analysis is indicated by a red data point, corresponding to averaging chunks of 373 frames with an Allan deviation of 0.52 cnt s^{-1}. This dataset consists of 2547 frames, which took about 12 hours to run.

An example dataset is shown in Fig. 7.6 for the lowest W_0 of 21.8 nW. This dataset was acquired over ≈ 12 hours. In Fig. 7.6(a), the background-subtracted image, which is averaged over the duration of the dataset, is shown for the 7x7 superpixel ROI. In Fig. 7.6(b) the fluorescence rate extracted from each frame's background-subtracted image is plotted in blue as a function of frame number. In Fig. 7.6(c) the Allan deviation of the fluorescence rate is plotted for different numbers of frames averaged over. A near optimum number of frames to average of 373 is selected which corresponds to an Allan deviation of 0.52 cnt s^{-1}. We average the data in chunks of 373 frames and plot the result in red in Fig. 7.6(b). These measurements have an average value of 0.98 cnt s^{-1}.

The results of our fluorescence measurements for a sample of 2×10^{-5} mol L^{-1} AF455 in toluene are plotted in Fig. 7.7. Here we show measured fluorescence count rates as a function of the power transmitted out of the fiber. The fit to the data is a linear regression performed on a log-log scale. The slope of the fit is 2.05, which confirms the two-photon origin of the signal. The lowest data point is measured at a power out W_{in} of 19.5 nW, which corresponds to an initial power W_0 of 21.8 nW.

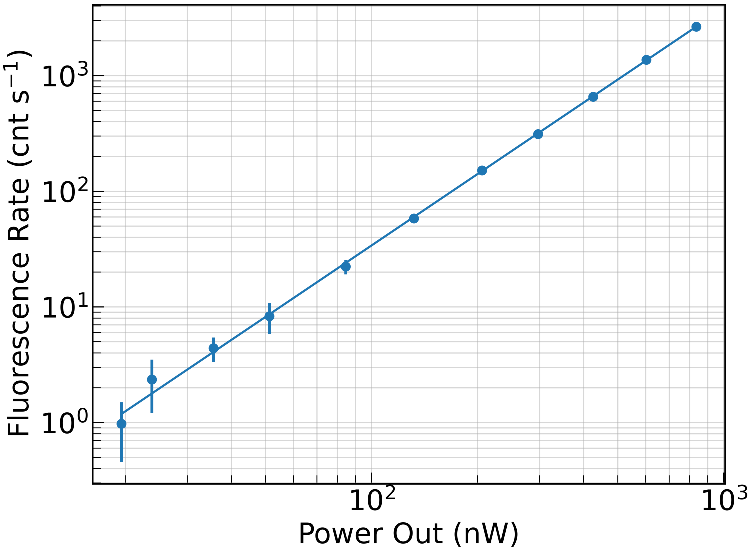

Figure 7.7: Fluorescence rate measured on the detector as a function of the power transmitted out of the fiber for a sample of 2×10^{-5} mol L^{-1} AF455 in toluene. The fit to the data has a slope of 2.05.

Using Eq. 7.12, we derive a C2PA cross section for AF455 of 170 GM. This result is 2-4 fold lower than cross sections reported in literature [17, 19]. We suspect that our cross section is lower due to two assumptions in our calculations that rely on all the light being confined to the fundamental mode of the fiber. In reality there are 16 modes which can propagate through the fiber and a fraction of the light is likely occupying those higher order modes as shown in Fig. 7.3(c). The photons in those higher-order modes have a decreased likelihood to be overlapped spatially and temporally at a molecule due to the complex spatial profiles and the increased group velocity dispersion.

7.8 Conclusions

We designed a toluene-filled hollow-core-fiber platform for two-photon excited fluorescence measurements. We used the results of our measurements and the characterizations we performed on the experimental setup to derive a C2PA cross section for AF455. The cross section agrees within a factor of 2 and 4 to the values of published cross sections. We believe that using a quantitative characterization of the mode composition of the excitation laser inside of the fiber would improve our calculation. Nevertheless, the close agreement to literature cross sections is strong evidence that our fiber platform can be used to derive absolute values of two-photon cross sections.

We measured C2PEF down to 21.8 nW excitation power. This is a 4-fold improvement from the sensitivity of the cuvette-based measurement system presented in Chapter 5. We believe that this is an underestimate of the system capabilities. Higher concentration samples should be measurable using this platform and will likely increase the signal strength. Measurements at an $\approx 2 \times 10^{-4}$ mol L^{-1} concentration level are feasible and would presumably lead to an additional 3-fold sensitivity improvement.

We minimized the losses in the system and optimized the alignment for 40% transmission efficiency through the fiber rendering this platform ideal for E2PA studies, in which loss is detrimental to the measurement sensitivity (Chapter 2 Section 2.6). Our future studies will implement entangled photon excitation with the goal of quantifying the first E2PA cross section, rather than an upper bound.

Chapter 8

Conclusions and Outlook

In this thesis we presented three sensitive experiments designed and used for entangled two-photon absorption (E2PA). Two are transmittance schemes and one is a fluorescence scheme. In all three cases, we were unable to resolve an E2PA signal because of its very small magnitude under excitation by typical values of spontaneous parametric down-conversion (SPDC) photon fluxes. We were the first to set upper bounds on E2PA cross sections, and we did so for a wide variety of absorbers - eight independent absorbers in room temperature liquids. Observing E2PA is challenging due to the nonlinear nature of 2PA and SPDC. The former requires strong spatial, temporal and spectral correlations between two photons while the latter occurs with a low likelihood ($\approx 10^{-7}$) set by the material of the crystal and the stringent phase-matching conditions. In our work, our maximum SPDC photon rate, which was limited by the damage threshold of the nonlinear crystal, is $\approx 10^{10}$ photons s^{-1} (a few nanowatts). For comparison, the expected classical two-photon absorption (C2PA) rate at a few nanowatts of excitation power (in a standard scheme) is about 1 molecule excited every few minutes – which is not detectable. Further complications arise in the fact that the E2PA signal at this maximum photon flux is already expected to have some contribution from the classical quadratic-photon-flux-dependent term (Eq. (2.3)). This is the regime where photon pairs are overlapped (mean photon number ≈ 150 photons pulse^{-1}) and a photon from one pair and another from a separate pair can excite a two-photon transition. In the quadratic regime, the quantum advantage of E2PA is not expected to be large.

The results of these experiments are unsurprising considering the recent theory [5, 27, 26, 25] and experiments [62, 57, 58] that have predicted or measured similar results. There exists the other camp of researchers whose results disagree with ours and motivated our investigation in the first place. However, their results do not prove the origin of the signal that they measure. In a paper of ours that is not covered in this thesis [61], we designed an experiment to measure E2PA, but instead measured a signal from hot-band absorption (HBA) that mimicked the behavior of E2PA. We distinguished between the two processes by testing for signatures of E2PA, such as the quadratic dependence of the signal on attenuation of the SPDC and by filtering the SPDC (Chapter 2, Section 2.6). The signals measured by other groups could be HBA, scattering [58] or some other one-photon loss mechanism.

In our efforts to measure E2PA we developed C2PA measurement systems. We made one-to-one comparisons between E2PA and C2PA to place upper bounds on the quantum advantage on the order of $10^2 - 10^3$ in the studied photon flux regime. Our cuvette-based fluorescence measurement system was used to derive absolute values of C2PA cross sections that agreed within a factor of two to literature cross sections. Our most recent C2PA system is the toluene-filled hollow-core fiber presented in Chapter 7. This system is capable of measuring C2PA at nanowatt excitation powers, thus making it ideal to attempt an E2PA measurement with.

The absolute magnitude of E2PA cross sections has yet to be narrowed down experimentally, as evidenced by Fig. 2.3. A few routes exist to get to that point. The first is to use waveguides such as our hollow-core fiber system. Another route is to use recent theory to guide the choice of experimental studies. Atomic systems may show promise due to the energy anticorrelations of SPDC being ideal for tuning to resonance with a narrow atomic transition. These simple atomic systems are nice starting points because they are theoretically well understood. Once an E2PA signal is measured, a wide range of parameters can be tuned to try to improve the signal.

Going forward, the perspective around the use of E2PA is shifting. It's clear that if there is a measurable quantum advantage of E2PA, it's much smaller than earlier experimental reports had thought. All the work that goes into designing a sensitive experiment to simply attempt to measure an E2PA signal indicates that using E2PA for microscopy is likely not going to be fruitful.

The use of E2PA for applications like sensing and spectroscopy is possible, and leads to a more realistic and constructive ideology.

Bibliography

[1] Robert W. Boyd. Nonlinear Optics, Third Edition. Academic Press, 2008.

[2] Daniel Adam Steck. Quantum and Atom Optics. Open Publication, 2007.

[3] J. Schneeloch and J. C. Howell. Introduction to the transverse spatial correlations in spontaneous parametric down-conversion through the biphoton birth zone. J. Opt, 18(5):053501, April 2016.

[4] Vatshal Srivastav, Natalia Herrera Valencia, Saroch Leedumrongwatthanakun, Will McCutcheon, and Mehul Malik. Characterizing and tailoring spatial correlations in multimode parametric down-conversion. Phys. Rev. Appl., 18(5):054006, November 2022.

[5] Michael G. Raymer, Tiemo Landes, and Andrew H. Marcus. Entangled two-photon absorption by atoms and molecules: A quantum optics tutorial. J. Chem. Phys., 155(8):081501, August 2021.

[6] Hong-Bing Fei, B. M. Jost, S. Popescu, B. E. A. Saleh, and M. C. Teich. Entanglement-induced two-photon transparency. Phys. Rev. Lett, 78(9):1679, March 1997.

[7] Bradley M. Jost, Alexander V. Sergienko, Ayman F. Abouraddy, Bahaa E. A. Saleh, and Malvin C. Teich. Spatial correlations of spontaneously down-converted photon pairs detected with a single-photon-sensitive ccd camera. Opt. Express, 3(2):81–88, July 1998.

[8] Roy J. Glauber. The quantum theory of optical coherence. Phys. Rev., 130(6):2529, June 1963.

[9] M. J. Stevens. Single-Photon Generation and Detection, chapter Photon Statistics, Measurements, and Measurements Tools. Academic Press, October 2013.

[10] Christopher C. Gerry and Peter L. Knight. Introductory Quantum Optics. Cambridge University Press, 2005.

[11] L. Gilles and P. L. Knight. Two-photon absorption and nonclassical states of light. Phys. Rev. A, 48:1582, August 1993.

[12] Maria Göppert-Mayer. Elementary processes with two quantum transitions. Ann. Phys., 401(3):273—-294, 1931.

[13] Peter Cronstrand. Quantum Chemical Calculations of Nonlinear Optical Absorption. PhD thesis, Royal Institute of Technology, 2004.

[14] W. Martin McClain and Robert A. Harris. Excited States, chapter Two-Photon Molecular Spectroscopy in Liquids and Gases. Academic Press, 1977.

[15] Mariacristina Rumi and Joseph W. Perry. Two-photon absorption: an overview of measurements and principles. Adv. Opt. Photonics, 2(4):451–518, December 2010.

[16] Nikolay S. Makarov, Mikhail Drobizhev, and Aleksander Rebane. Two-photon absorption standards in the 550–1600 nm excitation wavelength range. Opt. Express, 16(6):4029–4047, March 2008.

[17] S. de Reguardati, J. Pahapill, A. Mikhaylov, Y. Stepanenko, and A. Rebane. High-accuracy reference standards for two-photon absorption in the 680-1050 nm wavelength range. Opt. Express, 24(8):9053–9066, May 2016.

[18] Robert R. Birge and Brian M. Pierce. Semiclassical time-dependent theory of two-photon spectroscopy. the effect of dephasing in the virtual level on the two-photon excitation spectrum of isotachysterol. Int. J. Quantum Chem., 29(4):639–656, April 1986.

[19] Kristen M. Parzuchowski, Alexander Mikhaylov, Michael D. Mazurek, Ryan N. Wilson, Daniel J. Lum, Thomas Gerrits, Jr. Charles H. Camp, Martin J. Stevens, and Ralph Jimenez. Setting bounds on entangled two-photon absorption cross sections in common fluorophores. Phys. Rev. Appl., 15(4):044012, April 2021.

[20] W. Denk, J. H. Strickler, and W. W. Webb. Two-photon laser scanning fluorescence microscopy. Science, 248(4951):73–75, April 1990.

[21] W. R. Zipfel, R. M. Williams, and W. W. Webb. Nonlinear magic: multiphoton microscopy in the biosciences. Nat. Biotechnol, 21:1369–1377, October 2003.

[22] Konstantin E. Dorfman, Frank Schlawin, and Shaul Mukamel. Nonlinear optical signals and spectroscopy with quantum light. Rev. Mod. Phys, 88(4):045008, December 2016.

[23] J. Javanainen and P. L. Gould. Linear intensity dependence of a two-photon transition rate. Phys. Rev. A, 41(9):5088, May 1990.

[24] J. Gea-Banacloche. Two-photon absorption of nonclassical light. Phys. Rev. Lett, 62(14):1603, April 1989.

[25] C. Drago and J. E. Sipe. Aspects of two-photon absorption of squeezed light: The continuous-wave limit. Phys. Rev. A, 106(2):023115, August 2022.

[26] Tiemo Landes, Michael G. Raymer, Markus Allgaier, Sofiane Merkouche, Brian J. Smith, and Andrew H. Marcus. Quantifying the enhancement of two-photon absorption due to spectral-temporal entanglement. Opt. Express, 29(13):20022–20033, June 2021.

[27] Michael G. Raymer and Tiemo Landes. Theory of two-photon absorption with broadband squeezed vacuum. Phys. Rev. A, 106(1):013717, July 2022.

[28] Jr. Jan Peřina, Bahaa E. A. Saleh, and Malvin C. Teich. Multiphoton absorption cross section and virtual-state spectroscopy for the entangled n-photon state. Phys. Rev. A, 57(5):3972, May 1998.

[29] B. R. Mollow. Two-photon absorption and field correlation functions. Phys. Rev, 175(5):1555, 1968.

[30] G. S. Agarwal. Field-correlation effects in multiphoton absorption processes. Phys. Rev. A, 1:1445, May 1970.

[31] G. Kang, K. N. Avanaki, M. A. Mosquera, R. K. Burdick, J. P. Villabona-Monsalve, T. Goodson III, and G. C. Schatz. Efficient modeling of organic chromophores for entangled two-photon absorption. J. Am. Chem. Soc, 142(23):10446–10458, May 2020.

[32] Jun Kojima and Quang-Viet Nguyen. Entangled biphoton virtual-state spectroscopy of the $a^2\sigma^+$–$x^2\pi$ system of OH. Chem. Phys. Lett, 396(4–6):323–328, August 2004.

[33] Ryan K. Burdick, Oleg Varnavski, Andrew Molina, Leslie Upton, Paul Zimmerman, and Theodore Goodson III. Predicting and controlling entangled two-photon absorption in diatomic molecules. J. Phys. Chem, 122(41):8198–8212, September 2018.

[34] Heinz P. Weber. Two-photon-absorption laws for coherent and incoherent radiation. IEEE J. Quantum Electron, 7(5):189–195, May 1971.

[35] A. Jechow, M. Seefeldt, H. Kurzke, A. Heuer, and R. Menzel. Enhanced two-photon excited fluorescence from imaging agents using true thermal light. Nat. Photonics, 7:973–976, October 2013.

[36] F. Schlawin, K. E. Dorfman, and S. Mukamel. Entangled two-photon absorption spectroscopy. Acc. Chem. Res, 51(9):2207–2214, September 2018.

[37] Roberto de J. León-Montiel, J. Svozilík, J. P. Torres, and A. B. U'Ren. Temperature-controlled entangled-photon absorption spectroscopy. Phys. Rev. Lett, 123(2):023601, July 2019.

[38] E. Giese, R. Fickler, W. Zhang, L. Chen, and R. W. Boyd. Influence of pump coherence on the quantum properties of spontaneous parametric down-conversion. Phys. Scr, 93(8):084001, July 2018.

[39] Alejandra Valencia, Maria V. Chekhova, Alexei Trifonov, and Yanhua Shih. Entangled two-photon wave packet in a dispersive medium. Phys. Rev. Lett, 88(18):183601, April 2002.

[40] T. B. Pittman, D. V. Strekalov, D. N. Klyshko, M. H. Rubin, A. V. Sergienko, and Y. H. Shih. Two-photon geometric optics. Phys. Rev. A, 53(4):2804, April 1996.

[41] Wuhong Zhang, Robert Fickler, Enno Giese, Lixiang Chen, and Robert W. Boyd. Influence of pump coherence on the generation of position-momentum entanglement in optical parametric down-conversion. Opt. Express, 27(15):20745–20753, July 2019.

[42] M.P. Edgar, D.S. Tasca, F. Izdebski, R.E. Warburton, J. Leach, M. Agnew, G.S. Buller, R.W. Boyd, and M.J. Padgett. Imaging high-dimensional spatial entanglement with a camera. Nat. Commun, 3(984), August 2012.

[43] Manuel Unternährer, Bänz Bessire, Leonardo Gasparini, Matteo Perenzoni, and André Stefanov. Super-resolution quantum imaging at the Heisenberg limit. Optica, 5(9):1150–154, September 2018.

[44] W. M. McClain. Polarization of two-photon excited fluorescence. J. Chem. Phys, 58(1):324, January 1973.

[45] Joseph R. Lakowicz, Ignacy Gryczynski, Henryk Malak, and Zygmunt Gryczynski. Two-color two-photon excitation of fluorescence. Photochem. Photobiol, 64(4):632–635, June 1996.

[46] Alexandra Rapaport, Ferenc Szipöcs, and Michael Bass. Dependence of two-photon-absorption-excited fluorescence on the angle between the linear polarizations of two intersecting beams. Appl. Phys. Lett, 82(26):4642, April 2003.

[47] A. Eshun, Z. Cai, M. Awies, L. Yu, and T. Goodson III. Investigations of thienoacene molecules for classical and entangled two-photon absorption. J. Phys. Chem. A, 122(41):8167–8182, September 2018.

[48] D. Tabakaev, M. Montagnese, G. Haack, L. Bonacina, J.-P. Wolf, H. Zbinden, and R. T. Thew. Energy-time-entangled two-photon molecular absorption. Phys. Rev. A, 103(3):033701, March 2021.

[49] J. P. Villabona-Monsalve, O. Calderón-Losada, M. Nuñez Portela, and A. Valencia. Entangled two photon absorption cross section on the 808 nm region for the common dyes Zinc tetraphenylporphyrin and rhodamine B. J. Phys. Chem. A, 121(41):7869–7875, September 2017.

[50] A. R. Guzman, M. R. Harpham, Ö. Süzer, M. M. Haley, and T. G. Goodson III. Spatial control of entangled two-photon absorption with organic chromophores. J. Am. Chem. Soc, 132(23):7840–7841, May 2010.

[51] Dong-Ik Lee and T. Goodson. Entangled photon absorption in an organic porphyrin dendrimer. J. Phys. Chem. B, 110(51):25582—25585, December 2006.

[52] M. R. Harpham, Ö. Süzer, C. Ma, P. Bäuerle, and T. Goodson III. Thiophene dendrimers as entangled photon sensor materials. J. Am. Chem. Soc, 131(3):973–979, January 2009.

[53] L. Upton, M. Harpham, O. Suzer, M. Richter, S. Mukamel, and T. Goodson III. Optically excited entangled states in organic molecules illuminate the dark. J. Phys. Chem. Lett, 4(12):2046–2052, May 2013.

[54] J. P. Villabona-Monsalve, O. Varnavski, B. A. Palfey, and T. Goodson III. Two-photon excitation of flavins and flavoproteins with classical and quantum light. J. Am. Chem. Soc, 140(44):14562–14566, October 2018.

[55] J. P. Villabona-Monsalve, R. K. Burdick, and T. Goodson III. Measurements of entangled two-photon absorption in organic molecules with cw-pumped type-I spontaneous parametric down-conversion. J. Phys. Chem. C, 124(44):24526—24532, October 2020.

[56] Juan P. Villabona-Monsalve, Nikolai A. Tcyrulnikov, Emmaline R. Lorenzo, Nicole LaBine, Ryan Burdick, Matthew D. Krzyaniak, Ryan M. Young, Michael R. Wasielewski, and Theodore Goodson III. Two-photon absorption in electron donor–acceptor dyads and triads using classical and entangled photons: Potential systems for photon-to-spin quantum transduction. J. Phys. Chem. C, 126(14):6334–6343, March 2022.

[57] Samuel Corona-Aquino, Omar Calderón-Losada, Mayte Y. Li-Gómez, Hector Cruz-Ramirez, Violeta Álvarez Venicio, María del Pilar Carreón-Castro, Roberto de J. León-Montiel, and Alfred B. U'Ren. Experimental study of the validity of entangled two-photon absorption measurements in organic compounds. J. Phys. Chem. A, 126(14):2185–2195, April 2022.

[58] Bryce P. Hickam, Manni He, Nathan Harper, Szilard Szoke, and Scott K. Cushing. Single-photon scattering can account for the discrepancies among entangled two-photon measurement techniques. J. Phys. Chem. Lett., 13(22):4934–4940, May 2022.

[59] Alexander Mikhaylov, Kristen M. Parzuchowski, Michael D. Mazurek, Daniel J. Lum, Thomas Gerrits, Charles H. Camp, Martin J. Stevens, and Ralph Jimenez. A comprehensive experimental system for measuring molecular two-photon absorption using an ultrafast entangled photon pair excitation source. In Adv. Opt. Tech. for Quantum Information, Sensing, and Metrology, volume 11295. International Society for Optics and Photonics, SPIE, February 2020.

[60] Michael D. Mazurek, Kristen M. Parzuchowski, Alexander Mikhaylov, Sae Woo Nam, Charles H. Camp, Thomas Gerrits, Ralph Jimenez, and Martin J. Stevens. Bounding entangled two-photon absorption with sensitive transmittance measurements. In Conf. on Lasers and Electro-Optics, page FM3N.2. Optica Publishing Group, February 2021.

[61] Alexander Mikhaylov, Ryan N. Wilson, Kristen M. Parzuchowski, Michael D. Mazurek, Charles H. Camp Jr., Martin J. Stevens, and Ralph Jimenez. Hot-band absorption can mimic entangled two-photon absorption. J. Phys. Chem. Lett., 13(6):1489–1493, February 2022.

[62] Tiemo Landes, Markus Allgaier, Sofiane Merkouche, Brian J. Smith, Andrew H. Marcus, and Michael G. Raymer. Experimental feasibility of molecular two-photon absorption with isolated time-frequency-entangled photon pairs. Phys. Rev. Res., 3(3):033154, August 2021.

[63] O. Varnavski, B. Pinsky, and T. Goodson III. Entangled photon excited fluorescence in organic materials: An ultrafast coincidence detector. J. Phys. Chem. Lett, 8(3):388–393, January 2017.

[64] O. Varnavski and T. Goodson III. Two-photon fluorescence microscopy at extremely low excitation intensity: The power of quantum correlations. J. Am. Chem. Soc, 142(30):12966–12975, July 2020.

[65] B. Dayan, A. Pe'er, A. A. Friesem, and Y. Silberberg. Nonlinear interactions with an ultrahigh flux of broadband entangled photons. Phys. Rev. Lett, 94(4):043602, February 2005.

[66] Barak Dayan. Theory of two-photon interactions with broadband down-converted light and entangled photons. Phys. Rev. A, 76(4):043813, October 2007.

[67] L. Neri, S. Tudisco, F. Musumeci, A. Scordino, G. Fallica, M. Mazzillo, and M. Zimbone. Note: Dead time causes and correction method for single photon avalanche diode devices. Rev. Sci. Instrum, 81(8):0086102, August 2010.

[68] Pieter Kok, W. J. Munro, Kae Nemoto, T. C. Ralph, Jonathan P. Dowling, and G. J. Milburn. Linear optical quantum computing with photonic qubits. Rev. Mod. Phys, 79(1):135, January 2007.

[69] T. Gerrits, M. J. Stevens, B. Baek, B. Calkins, A. Lita, S. Glancy, E. Knill, S. Woo Nam, R. P. Mirin, R. H. Hadfield, R. S. Bennink, W. P. Grice, S. Dorenbos, T. Zijlstra, T. Klapwijk, and V. Zwiller. Generation of degenerate, factorizable, pulsed squeezed light at telecom wavelengths. Opt. Express, 19(24):24434–24447, November 2011.

[70] J. Stöhr. Overcoming the diffraction limit by multi-photon interference: a tutorial. Adv. Opt. Photonics, 11(1):215–313, November 2018.

[71] L. A. Rozema, J. D. Bateman, D. H. Mahler, R. Okamoto, A. Feizpour, A. Hayat, and A. M. Steinberg. Scalable spatial superresolution using entangled photons. Phys. Rev. Lett, 112(22):223602, June 2014.

[72] Ryan K. Burdick, Juan P. Villabona-Monsalve, George A. Mashour, and Theodore Goodson III. Modern anesthetic ethers demonstrate quantum interactions with entangled photons. Sci. Rep., 9(11351), August 2019.

[73] Graham H. Barnett, Mervyn F. Hudson, and Kevin M. Smith. Concerning meso-tetraphenylporphyrin purification. J. Chem. Soc., Perkin Trans. 1, pages 1401–1403, 1975.

[74] Yoon-Ho Kim and Warren P. Grice. Generation of pulsed polarization-entangled two-photon state via temporal and spectral engineering. J. of Mod. Opt., 49:2309–2323, July 2002.

[75] C. K. Hong, Z. Y. Ou, and L. Mandel. Measurement of subpicosecond time intervals between two photons by interference. Phys. Rev. Lett., 59:2044–, November 1987.

[76] Keiichi Edamatsu, Ryosuke Shimizu, and Tadashi Itoh. Measurement of the photonic de broglie wavelength of entangled photon pairs generated by spontaneous parametric down-conversion. Phys. Rev. Lett., 89:213601, November 2002.

[77] Till T. Meiling, Piotr J. Cywiński, and Hans-Gerd Löhmannsröben. Two-photon excitation fluorescence spectroscopy of quantum dots: Photophysical properties and application in bioassays. J. Phys. Chem. C, 122(17):9641–9647, April 2018.

[78] Ramamurthi Kannan, Guang S. He, Tzu-Chau Lin, Paras N. Prasad, Richard A. Vaia, and Loon-Seng Tan. Toward highly active two-photon absorbing liquids. synthesis and characterization of 1,3,5-triazine-based octupolar molecules. Chem. Mater, 16(1):185–194, November 2004.

[79] J. E. Rogers, J. E. Slagle, D. G. McLean, R. L. Sutherland, B. Sankaran, R. Kannan, Loon-Seng Tan, and P. A. Fleitz. Understanding the one-photon photophysical properties of a two-photon absorbing chromophore. J. Phys. Chem. A, 108(26):5514–5520, June 2004.

[80] A. K. Gaigalas, P. DeRose, L. Wang, and Yu-Zhong Zhang. Optical properties of CdSe/ZnS nanocrystals. J. Res. Natl. Inst. Stand. Technol, 119:610–628, December 2014.

[81] M. M. Martin and L. Lindqvist. The pH dependence of fluorescein fluorescence. J. Lumin, 10(6):381–390, March 1975.

[82] A. Penzkofer and W. Leupacher. Fluorescence behaviour of highly concentrated rhodamine 6G solutions. J. Lumin, 37(2):61–72, May 1987.

[83] R. Królicki, W. Jarzęba, M. Mostafavi, and I. Lampre. Preferential solvation of coumarin 153 - the role of hydrogen bonding. J. Phys. Chem. A, 106(9):1708–1713, February 2002.

[84] G. Mainfray and C. Manus. Multiphoton ionization of atoms, chapter 2. Academic Press, 1984.

[85] Ariel Ashkenazy, Kai Wang, Manuel Unternährer, Dror Fixler, and André Stefanov. Estimation of the rate of entangled-photon-pair interaction with metallic nanoparticles based on classical-light second-harmonic generation measurements. J. Phys. B, 52(14):145401, June 2019.

[86] T. Li, F. Li, C. Altuzarra, A. Classen, and G. S. Agarwal. Squeezed light induced two-photon absorption fluorescence of fluorescein biomarkers. Appl. Phys. Lett, 116(25):254001, June 2020.

[87] D N Klyshko. Use of two-photon light for absolute calibration of photoelectric detectors. Sov. J. of Quantum Electron., 10(9):1112, September 1980.

[88] Gareth O. S. Williams, Tijmen G. Euser, Jochen Arlt, Philip St.J. Russell, and Anita C. Jones. Taking two-photon excitation to exceptional path-lengths in photonic crystal fiber. ACS Photonics, 1(9):790–793, August 2014.

[89] Di Yan, Jürgen Popp, Mathias W. Pletz, and Torsten Frosch. Highly sensitive broadband raman sensing of antibiotics in step-index hollow-core photonic crystal fibers. ACS Photonics, 4(1):138–145, January 2017.

[90] John M Fini. Microstructure fibres for optical sensing in gases and liquids. Meas. Sci. Technol., 15(6):1120, May 2004.

[91] S. Kedenburg, M. Vieweg, T. Gissibl, and H. Giessen. Linear refractive index and absorption measurements of nonlinear optical liquids in the visible and near-infrared spectral region. Opt. Mater. Express, 2(11):1588–1611, November 2012.

[92] Aliaksandr Karotki, Mikhal Drobizhev, Mikalai Kruk, Charles Spangler, Erik Nickel, Nugzar Mamardashvili, and Aleksander Rebane. Enhancement of two-photon absorption in tetrapyrrolic compounds. J. Opt. Soc. Am. B, 20(2):321–332, February 2003.

[93] M. D. Young, J. J. Field, K. E. Sheetz, R. A. Bartels, and J. Squier. A pragmatic guide to multiphoton microscope design. Adv. Opt. and Photonics, 7(2):276–378, May 2015.

Appendix A

Literature summary

In Table A.1, a summary of data from all (to the best of our knowledge) experimental E2PA reports in literature is shown. E2PA cross sections (σ_E) or cross section upper bounds (σ_E^{UB}) are listed for various studied absorbers. Abbreviated name are sometimes shown for the absorbers. Here we list more formal names for the absorbers, however the reports should be referenced for a more thorough description. The abbreviated absorbers are:

- FAD = flavin adenine dinucleotide
- ZnTPP = Zinc tetraphenylporphyrin
- Qdot 605 = Qdot ITK carboxyl quantum dot 605
- Rh6G = rhodamine 6G
- AF455 = 1,3,5-triazine-based octupolar molecule “Air Force 455”
- RhB = rhodamine B
- Dyad 1 = 9-(N-piperidinyl)perylene-3,4-dicarboximide (6PMI) linked to naphthalene-(1,4:5,8)-bis(dicarboximide) (NDI)
- Dyad 2 = 6PMI linked to NDI via a phenyl spacer
- Triad 1 = dyad 1 with the additional link of 6PMI to a tetrathiafulvalene (TTF) donor
- Triad 2 = dyad 2 with the additional link of 6PMI to a TTF donor
- LDS 798 = styryl 11

- C153 = coumarin 153
- OM82C = nitrogen centered tolane dendrimer
- FMN = flavin mononucleotide
- 9R = 9-Ringed benzodithiophene compound
- 9R-X = 9-Ringed benzodithiophene derivative with central atom X
- XT = thiophene dendrimers with X thiophene units
- H_2TPP = tetraphenylporphyrin

A few of the references in the table did not report a σ_E^{UB}, however the information in their report could be used to estimate σ_E^{UB}. Here we discuss how we calculated these values.

In Ref. [62], the authors designed a sensitive fluorescence measurement technique, but could not measure a fluorescence signal due to E2PA. We can estimate σ_E^{UB} in their experiment using a version of Eq. (5.19). From their report we find the values for the measurable fluorescence lower bound $F^{\mathrm{LB}} = 0.7\ \mathrm{s}^{-1}$, the concentration $c = 2 \times 10^{-3}$ mol L^{-1} ($n \propto cN_A$, where N_A is Avogadro's number), the cuvette length $l = 1$ cm, the quantum yield $\Phi = 0.8$, the detection efficiency $\gamma = 0.1$, the collection efficiency $\kappa = 0.019$. We also find the SPDC photon pair rate at the sample 2.0×10^9 photons s^{-1}, which is a lower bound on the photon rate because of fiber coupling. This value intrinsically accounts for loss in the setup and effectively gives $\mathcal{T}Q = 4.0 \times 10^9$ photons s^{-1}. We then solve for the upper bound using,

$$\sigma_E^{\mathrm{UB}} = \frac{2F^{\mathrm{LB}}}{\mathcal{T}Qn\kappa l\gamma\Phi}, \tag{A.1}$$

and derive $\sigma_E^{\mathrm{UB}} = 1.9 \times 10^{-25}$ cm^2 absorber^{-1}.

In our work, Ref. [61], a sensitive fluorescence measurement was implemented for two samples. The provided information in the paper gives the values for parameters necessary to calculate σ_E^{UB} using Eq. (A.1). For the 3.0×10^{-4} mol L^{-1} LDS798 sample, a signal was measured due to hot-band absorption (HBA). We can use the HBA signal as lower bound for the signal that could be detected due to E2PA in this setup: $F^{\mathrm{LB}} \approx 33$ cnt s^{-1} for $1.0\,\mu$W SPDC excitation. The other

Table A.1: A summary of all E2PA cross sections (σ_E) and cross section upper bounds (σ_E^{UB}) published in literature prior to 2023. For each report, the publication date, group, and excitation wavelength is listed. Each reported absorber is listed with its C2PA cross section (σ_E) and E2PA cross sections (σ_E) or cross section upper bounds (σ_E^{UB}). References marked with a * did not report σ_E^{UB}, but we calculated it based on their experimental details as discussed in this Appendix.

Date [Ref.] MM/DD/YY	Group	Wavelength (nm)	Absorber	σ_C [Ref.] (GM)	$\sigma_E \times 10^{18}$ (cm^2 absorber^{-1})	$\sigma_E^{\mathrm{UB}} \times 10^{24}$ (cm^2 absorber^{-1})
This work (Chapter 6)	JILA/NIST	810	Fluorescein	13 ± 4 [19]		420
			FAD	2.1 [54]		900
			ZnTPP	20 [53]		2400
			Qdot 605	46000 ± 13000 [19]		660000
			Rh6G	51 ± 14 [19]		310
			9R-S	22 ± 6 [19]		2500
			AF455	660 ± 180 [19]		980
04/06/22 [57] *	UNAM	810	RhB	260 ± 39 [16]		1700
			ZnTPP	20 [53]		18000
05/29/22 [58] *	Caltech	812	Rh6G	51 ± 14 [19]		2000 ± 1000
03/31/22 [56]	Univ. Michigan	810	Dyad 1	4.06 ± 0.41	0.038 ± 0.007	
			Dyad 2	0.60 ± 0.05	0.19 ± 0.02	
			Triad 1	3.82 ± 0.21	0.092 ± 0.011	
			Triad 2	0.82 ± 0.14	0.071 ± 0.004	
02/07/22 [61] *	JILA/NIST	1064	Rh6G	9.9 ± 2.8		0.00027 ± 0.00006
			LDS 798	220 ± 60		4.7 ± 1.1
08/13/21 [62] *	Univ. Oregon	1064	Rh6G	9.9 ± 2.8 [61]		0.19
04/06/21 [19]	JILA/NIST	810	AF455	660 ± 180		0.21 ± 0.05
			Qdot 605	46000 ± 13000		48 ± 12
			Fluorescein	13 ± 4		0.10 ± 0.02
			9R-S	22 ± 6		2.0 ± 0.6
			Rh6G	51 ± 14		0.12 ± 0.03
			C153	14 ± 4		0.16 ± 0.04
03/01/21 [48]	Univ. Geneva	1064	Rh6G	9.9 ± 2.8 [61]	0.0019 ± 0.0009	
10/26/20 [55]	Univ. Michigan	810	Bisannulene	150 [50]	4.50 ± 0.58	
			OM82C	370 [53]	3.08 ± 0.06	
			FAD	2.1 [54]	0.979 ± 0.009	
			ZnTPP	20 [53]	0.754 ± 0.010	
			FMN	1.6 [54]	0.038 ± 0.002	
02/28/20 [59]	JILA/NIST	810	ZnTPP	20 [53]		170000
10/22/18 [54]	Univ. Michigan	800	FAD	2.1	0.29	
			FMN	1.6	1.4	
09/25/18 [47]	Univ. Michigan	800	9R	29.5	0.810 ± 0.097	
			9R-N	82.5	0.525 ± 0.0063	
			9R-S	27.9	0.202 ± 0.024	
			9R-Se	9.01	0.164 ± 0.020	
09/21/17 [49]	Uniandes	808	ZnTPP	20 [53]	42 ± 5.2	
			RhB	260 ± 39 [16]	4.2 ± 0.34	
05/21/13 [53]	Univ. Michigan	800	OM82C	370	23.3	
			ZnTPP	20	23.7	
			42T	620	12.7	
			90T	1130	20.8	
05/24/10 [50]	Univ. Michigan	800	Bisannulene	150	32	
			Triannulene	1650	81	
			Tetraannulene	2960	99	
01/05/09 [52]	Univ. Michigan	800	6T	6	0.13	
			18T	230	0.71	
			42T	620	2.6	
			90T	1130	5.9	
12/07/06 [51]	Univ. Michigan	800	H_2TPP	10 [92]	10	

parameters are the component transmission efficiency (which includes the detection efficiency as well as the transmission efficiency of other optical components such as filters) $\gamma = 0.025$, the quantum yield $\phi = 0.054$, the loss between the crystal and the sample $\mathcal{T} = 0.26$, the length of the sample $l = 1$ cm and the collection efficiency $\kappa = 0.042$. For the 1.1×10^{-3} mol L^{-1} sample of Rh6G, $\gamma = 0.082$, $\phi = 0.9$ and no signal was detected, thus we use the sensitivity of the detection system $F^{\mathrm{LB}} = 0.5$ cnt s^{-1}. Then we derive $\sigma_E^{\mathrm{UB}} = 4.7 \times 10^{-24}$ cm^2 $\mathrm{absorber}^{-1}$ for LDS798 and $\sigma_E^{\mathrm{UB}} = 2.7 \times 10^{-28}$ cm^2 $\mathrm{absorber}^{-1}$ for Rh6G.

In Ref. [58], the authors present a sensitive transmittance and fluorescence measurement system, but instead of measuring E2PA, they measure a scattering signal from Rh6G with cross section $(2 \pm 1) \times 10^{-21}$ cm^2 $\mathrm{absorber}^{-1}$. The authors were not able to filter out the scattering to achieve a higher sensitivity, thus this cross section serves as a σ_E^{UB} value as well.

In Ref. [57] the authors designed a sensitive transmittance experiment with the goal of making their experiment insensitive to one-photon losses. The authors derived Eq. (10),

$$\sigma_E = \frac{\Gamma}{clN_A}, \tag{A.2}$$

where Γ is the measured one-photon loss insensitive change in transmittance, found using singles and coincidence rates measured through sample and solvent. The authors used multiple measurement techniques of differing levels of complexity, including a time-delay technique. For all measurement techniques and for two samples of varying concentrations, $\Gamma \approx 0$. To set a σ_E^{UB}, we estimate upper bounds on Γ from their measurements. We use their measurements for the highest concentrations of their samples, for RhB $c = 5.8 \times 10^{-2}$ mol L^{-1} and for ZnTPP $c = 1.4 \times 10^{-3}$ mol L^{-1}. Then for all measurement techniques $\Gamma \leq 0.060$ for RhB and $\Gamma \leq 0.015$ for ZnTPP. We plug these upper bounds for Γ into Eq. (A.2) using the length of the sample $l = 1$ cm, and derive $\sigma_E^{\mathrm{UB}} = 1.7 \times 10^{-21}$ cm^2 $\mathrm{absorber}^{-1}$ for RhB and $\sigma_E^{\mathrm{UB}} = 1.8 \times 10^{-20}$ cm^2 $\mathrm{absorber}^{-1}$ for ZnTPP.

Appendix B

Sample preparation details

The “AF455” fluorophore [78, 79] is provided by Drs. T. Loon-Seng Tan and T. Cooper from the Air Force Research Laboratory. Flavin adenine dinucleotide (FAD), Zinc tetraphenylporphyrin (ZnTPP), fluorescein, rhodamine 590 (6G) and coumarin 153 (540A) are ordered from Sigma-Aldrich and used as received. Qdot ITK Carboxyl Quantum dot 605 (qdot 605) in borate buffer is ordered from ThermoFisher, stored at 4°C and only used for six months after receiving. The thienoacene fluorophore “9R-S” [47] is provided by Prof. T. Goodson from the University of Michigan. Various solvents are used to prepare the samples including phosphate buffered saline (PBS, prepared), toluene ($\geq$ 99.98%), pH 11 water (Hydrion pH 11 buffer capsule in distilled water), methanol ($\geq$ 99.9%), ethanol ($\geq$ 99.5%), chloroform ($\geq$ 99.9%) and borate buffer (prepared). The concentration and absorption/emission spectra of all samples (except qdot 605) are checked using a UV-VIS-NIR spectrophotometer (Agilent Cary 5000 Scan) and a fluorometer (Horiba Fluorolog-3 FL3-222). The absorption and emission spectra are compared with published spectra to ensure the samples are not contaminated or degraded.

Appendix C

Detailed experimental diagram and parts list for Chapter 4

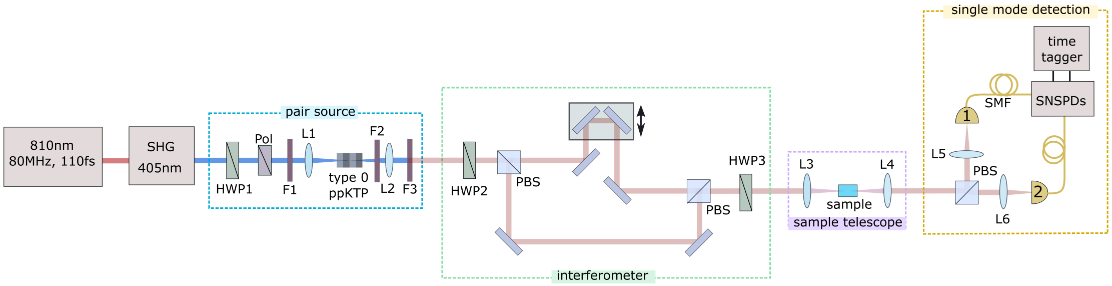

Figure C.1: Detailed diagram of our experimental setup. See main text for abbreviation definitions and part numbers.

In Fig. C.1, we show a detailed diagram of our setup with labeled parts. We list the part numbers below.

Main source

- Laser source = Coherent Chameleon Discovery
- SHG = APE HarmoniXX SHG

Pair source

- HWP1 = zero-order half-wave plate 405 nm (Thorlabs WPH05M-405)
- Pol = glan laser calcite polarizer (Thorlabs GL10-A)

- F1 = dichroic mirrors (3 x 10Q20BB.1 and TLM-400-45S-1025), interference bandpass filters (2 x Thorlabs FBH405-10, 1 x Thorlabs FB405-10, 1 x Semrock FF01-405/10-25) and colored glass filter (Thorlabs FGB37M)
- L1 = 300 mm focal length lens (Thorlabs LA4579-A)
- ppKTP crystal (Raicol Crystals Ltd., type-0 SHG, AR coated, 3.425 μm poling period, 10 mm long)
- crystal temperature controller (Covesion PV10) set to $30.00°\text{C} \pm 0.01°\text{C}$
- F2 = interference longpass filters (Semrock BLP01-442R-25, BLP01-633R-25 and 3 x FF01-496/LP)
- L2 = 175 mm focal length lens (KPX103AR.16)
- F3 = dichroic mirrors (2 x ARO MR6040) and bandpass filters (Thorlabs FBH800-40, FBH810-10)

Interferometer

- HWP2 = zero-order half-wave plate 808 nm (Thorlabs WPH10M-808)
- PBS = polarizing beam splitting cube (Thorlabs PBS12-780-HP)
- hollow roof prism mirror (Thorlabs HR1015-AG)
- Newport PM10069 motorized translation stage
- Newport PM500-C precision motion controller
- PBS = polarizing beam splitting cube (Thorlabs PBS12-780-HP)
- HWP3 = half-wave plate 800 nm (Tower Optical)

Sample telescope

- L3 = 50 mm focal length lens (Thorlabs LA1131-B)
- 1 cm UV quartz sample cuvette (Starna, 23-Q-10)

- L4 = 50 mm focal length lens (Thorlabs LA1131-B)

Single-mode detection stage

- PBS = polarizing beam splitting cube (Thorlabs PBS12-780-HP)
- L5 and L6 = 12.7 mm focal length achromatic doublet (Thorlabs AC064-013-B)
- SMF = 2 x 5 m-long patch cables (Thorlabs 780HP), optional 2 x 500 m-long single mode fiber (Nufern 780-OCT)
- SNSPDs = superconducting nanowire single-photon detectors (Quantum Opus, LLC, Opus One, optimized for the 850-1200 nm wavelength region) with a detection efficiency of $\approx 75\%$ at 810 nm
- closed-cycle helium cryocooler (Sumitomo HC-4E2)
- temperature monitor (SIM 922)
- detector bias and readout modules (Quantum Opus, LLC, QO-SIM-CRYO)
- time tagger = picosecond event timer and time-correlated single photon counting system (PicoQuant HydraHarp 400)

Appendix D

Data for Chapter 4

Coincidence rate data recorded in our experiments (illustrated in Fig. 4.5) and used in the analysis section are presented in Table D.1 for neat solvent and sample at zero and τ delays. All rates are presented at 10 different 405 nm pump powers ranging from ≈ 60 μW to 10.9 mW. The rates are listed in counts per second (cnt s^{-1}). The rates are averaged near τ and zero delays, marked as R_τ and R_0, respectively. Measurements at each pump power are repeated multiple times, from which averages and standard deviations (used as the uncertainties) are calculated.

Table D.1: Coincidence rates measured with solvent (solv) and sample (samp) at zero (0) and τ delays.

Pump Power (mW)	R_τ^{solv} (cnt s^{-1})	R_τ^{samp} (cnt s^{-1})	R_0^{solv} (cnt s^{-1})	R_0^{samp} (cnt s^{-1})
0.06	198 ± 8	163 ± 6	195 ± 5	165 ± 5
0.10	306 ± 6	258 ± 9	300 ± 5	252 ± 6
0.45	1491 ± 35	1240 ± 60	1481 ± 23	1249 ± 39
1.08	3670 ± 60	3120 ± 70	3650 ± 50	3103 ± 48
2.15	6960 ± 100	59960 ± 120	6920 ± 70	5880 ± 110
3.25	11200 ± 100	9640 ± 140	11140 ± 70	9590 ± 170
4.72	16350 ± 120	14080 ± 140	16230 ± 110	14010 ± 230
6.53	22670 ± 130	19530 ± 310	22520 ± 100	19340 ± 330
8.60	29850 ± 90	25830 ± 310	29670 ± 140	25540 ± 300
10.9	37780 ± 200	32790 ± 380	37520 ± 190	32570 ± 270

Appendix E

Detailed experimental diagram and parts list for Chapter 5

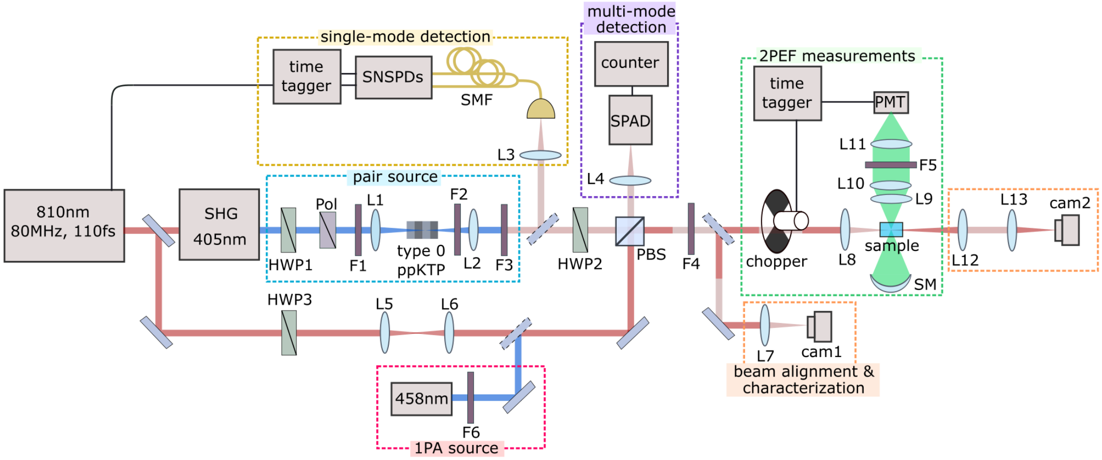

Figure E.1: Detailed diagram of our experimental setup. See main text for abbreviation definitions and part numbers.

In Fig. E.1, we show a detailed diagram of our setup with labeled parts. We list the part numbers below.

Main source

- Laser source = Coherent Chameleon Discovery
- SHG = APE HarmoniXX SHG

Pair source

- HWP1 = zero-order half-wave plate 405 nm (Thorlabs WPH05M-405)

- Pol = glan laser calcite polarizer (Thorlabs GL10-A)
- F1 = dichroic mirrors (3 x 10Q20BB.1 and TLM-400-45S-1025), interference bandpass filters (2 x Thorlabs FBH405-10, 1 x Thorlabs FB405-10, 1 x Semrock FF01-405/10-25) and colored glass filter (Thorlabs FGB37M)
- L1 = 300 mm focal length lens (Thorlabs LA4579-A)
- ppKTP crystal (Raicol Crystals Ltd., type-0 SHG, AR coated, 3.425 μm poling period, 10 mm long)
- crystal temperature controller (Covesion PV10) set to $30.00°\text{C} \pm 0.01°\text{C}$
- F2 = interference longpass filters (Semrock BLP01-442R-25, BLP01-633R-25 and 3 x FF01-496/LP)
- L2 = 200 mm focal length lens (Thorlabs LA1979-B)
- F3 = dichroic mirrors (2 x ARO MR6040) and interference longpass filter (Thorlabs FELH0700)

Single-mode detection stage

- L3 = 12.7 mm focal length achromatic doublet (Thorlabs AC064-013-B)
- fiber beamsplitter (Thorlabs FC830-5OB-FC)
- SMF = 2 x 500 m-long single mode fiber (Nufern 780-OCT)
- SNSPDs = superconducting nanowire single-photon detectors (Quantum Opus, LLC, Opus One, optimized for the 850-1200 nm wavelength region) with a detection efficiency of $\approx 75\%$ at 810 nm
- closed-cycle helium cryocooler (Sumitomo HC-4E2)
- temperature monitor (SIM 922)
- detector bias and readout modules (Quantum Opus, LLC, QO-SIM-CRYO)

- time tagger = picosecond event timer and time-correlated single photon counting system (PicoQuant HydraHarp 400)

Multi-mode detection stage

- L4 = 50.2 mm focal length lens (Newport KPX082AR.16)
- SPAD = single-photon avalanche diode (PerkinElmer SPCM-AQR-14)
- counter = timer/counter/anaylzer (Tektronix FCA3103)

2PEF measurements

- optical chopper head and controller (New Focus 3501 Optical Chopper)
- L8 = 50 mm focal length lens (Thorlabs LA1131-B)
- UV quartz sample cuvette with 2 mm width × 10 mm path length (FireFlySci, 1FLUV2), the narrow width is chosen to reduce fluorescence self-absorption in the sample
- machined cuvette holder designed for stability and low footprint to bring optics close to excitation volume
- L9, L10, L11 = Collection Optic with High Numerical Aperture (COHNA) lens system [93]
- F5 = shortpass filter (Semrock FF01-758/SP-25) and sample-dependent bandpass filter (AF455 and C153 - Semrock FF02-470/100-25, qdot 605 and 9R-S - Chroma ET610/75m, fluorescein and Rh6G - Semrock FF01-535/150-25) (filter spectra is shown in Fig. 5.3)
- SM = spherical mirror with 15 mm focal length, 35 mm diameter (Edmund Optics, #43-467)
- PMT = photon-counting metal package photomultiplier tube (Hamamatsu H10682-210)
- thermoelectric cooler (TEC) (CP40336) to cool PMT to 5°C
- CPU cooler (Rosewell PB120) for heat sink of TEC
- time tagger = picosecond event timer and time-correlated single photon counting system (PicoQuant HydraHarp 400)

Beam alignment and characterization (details on use in Appendix F)

- L7 = 50 mm focal length lens (Thorlabs LA1131-B)
- L12 = 50 mm focal length lens (Thorlabs LA1131-B)
- L13 = 62.9 mm focal length lens (Newport KPX085AR.16)
- cam1 = UI-3590LE-C-HQ camera
- cam2 = Thorlabs UI-224XSE camera

1PA source

- 458 nm source = OBIS 458 LX
- F6 = neutral density (ND) filter wheel (Thorlabs)

Other parts

- HWP2 = zero-order half-wave plate 808 nm (Thorlabs WPH10M-808)
- HWP3 = half-wave plate 800 nm (Tower Optical)
- L5 = 88.3 mm focal length lens (Newport KPX091AR.16)
- L6 = 75 mm focal length lens (Newport KPC037AR.16)
- PBS = polarizing beam splitting cube (Thorlabs PBS122)
- F4 = longpass interference filter (FELH0700)

Appendix F

Alignment details for Chapter 5

A telescope (L5 and L6) is used to resize the laser beam close to the SPDC beam size at their foci in the sample. The alignment of the beam into the sample is checked using two cameras (cam1 and cam2). Lenses L7 and L8 are placed approximately the same distance from the flip mirror, enabling a view on cam1 of the beams at and near their foci in the cuvette. With this camera, we check the alignment of the beams through alignment irises, and measure beam size, Rayleigh range and overlap of the laser and SPDC beams. Two lenses after the sample (L12 and L13) collimate and focus either beam onto cam2. With this camera, we verify that the beams remain overlapped after passage through the cuvette, are centered along the x-direction inside of the cuvette and propagate nearly perpendicular to the cuvette walls they are incident on. To check that the beams are centered in the x-direction, we first use a translation stage to translate the cuvette along this axis and observe on the camera when the beams' strike the walls of the cuvette. We translate the micrometer to the midpoint of the locations of the wall striking events. To check that the beams propagate perpendicular to the walls they are incident on, we ensure that adding the cuvette does not displace the beams in the x and y-directions significantly.

A typical transverse spatial overlap of the two beams at their foci (cam1) in the sample is shown in Fig. 5.2(b). The centers of the laser and SPDC beam are displaced from one another by $\approx 5\,\mu$m vertically and horizontally. Zemax simulations (Fig. 5.2) indicate that displacements of this magnitude have no effect on the collection efficiency. The beams' centers on cam2 are also overlapped within $\approx 5\,\mu$m vertically and horizontally. The beam overlap is checked regularly. To initially align the beams in the z-direction, the lens L8 is placed roughly one focal length away from the center of the cuvette.

The COHNA lens system (L9, L10 and L11) and filters (F5) are contained within a 25.4 mm-diameter lens tube. The spacing of the optics in the lens tube is based on Ref. [93]. The COHNA lens system (and filters) and the spherical mirror (SM) are each placed on a three-axis stage and initially aligned in the three directions based on the optimal spacings found using Zemax's OpticStudio. To optimize the alignment of the system (COHNA, SM and lens L8), we first adjust lens L8 to optimize collected C2PEF, which ensures that the excitation volume is centered with respect to the collection optics. Next, the COHNA lens system and the spherical mirror are each adjusted to maximize the collection of C2PEF. This process is iterated until the collection efficiency is optimal. A CW 458 nm source excites 1PEF in the sample to aid in the characterization of the geometrical collection efficiency (Section 5.4).

The alignment procedure using C2PEF optimizes the alignment of the system for C2PEF. For E2PEF, the alignment (only lens L8) must be slightly altered because we observe (on cam1) a shift between the foci of the laser and SPDC beam in the z-direction of $\approx 500\,\mu$m. We compensate for this by shifting lens L8 so that either beam's focus is in the center of the cuvette prior to measurements.

Appendix G

Detailed experimental diagram and parts list for Chapter 6

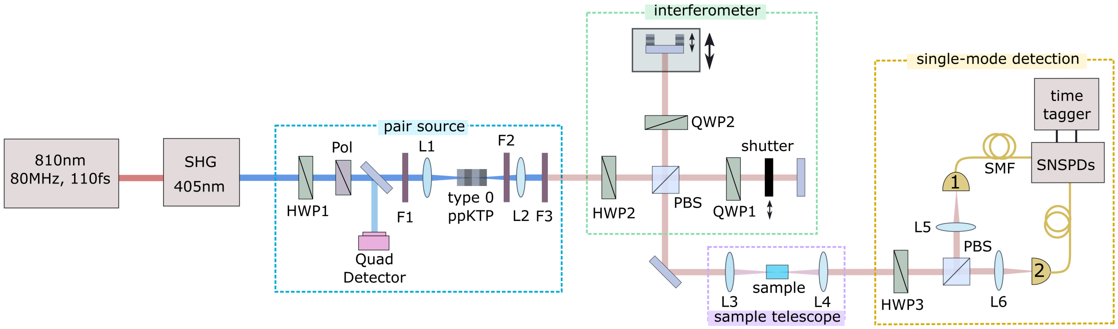

Figure G.1: Detailed diagram of our experimental setup. See main text for abbreviation definitions and part numbers.

In Fig. G.1, we show a detailed diagram of our setup with labeled parts. We list the part numbers below.

Main source

- Laser source = Coherent Chameleon Discovery
- SHG = APE HarmoniXX SHG

Pair source

- HWP1 = zero-order half-wave plate 405 nm (Thorlabs WPH05M-405)
- Pol = glan laser calcite polarizer (Thorlabs GL10-A)

- F1 = dichroic mirrors (3 x 10Q20BB.1 and TLM-400-45S-1025), interference bandpass filters (2 x Thorlabs FBH405-10, 2 x Semrock FF01-405/10-25) and colored glass filter (Thorlabs FGB37M)
- Quad detector = quadrant photodiode (First Sensor QP50-6-18u-SD2)
- L1 = 300 mm focal length lens (Thorlabs LA4579-A)
- ppKTP crystal (Raicol Crystals Ltd., type-0 SHG, AR coated, 3.425 μm poling period, 10 mm long)
- crystal temperature controller (Covesion PV10) set to 30.00°C ± 0.01°C
- F2 = interference longpass filters (Semrock BLP01-442R-25, BLP01-633R-25 and 3 x FF01-496/LP)
- L2 = 200 mm focal length lens (Thorlabs LA1979-B)
- F3 = dichroic mirrors (2 x ARO MR6040) and bandpass filter (Semrock FF01-810-10)

Interferometer

- HWP2 = zero-order half-wave plate 808 nm (Thorlabs WPH10M-808)
- PBS = polarizing beam splitting cube (Thorlabs PBS12-780-HP)
- QWP1 = quarter-wave plate (Tower Achromatic Waveplate A-12.7-A-250-B-2)
- QWP2 = quarter-wave plate (Thorlabs AQWP05M-980)
- shutter = optical beam shutter (Thorlabs SH05)
- piezoelectric Optic Mount (Thorlabs KC1-P)
- motorized actuator (Thorlabs Z825B)

Sample telescope

- L3 = 75 mm focal length lens (Thorlabs LA1608-B)
- 1 cm UV quartz sample cuvette (Starna, 23-Q-10)

- L4 = 75 mm focal length lens (Thorlabs LA1608-B)

Single-mode detection stage

- HWP3 = half-wave plate 800 nm (Tower Optical)
- PBS = polarizing beam splitting cube (Thorlabs PBS12-780-HP)
- L5 and L6 = 12.7 mm focal length achromatic doublet (Thorlabs AC064-013-B)
- SMF = 2 x 5 m-long patch cables (Thorlabs 780HP) optional 2 x 500 m-long single mode fiber (Nufern 780-OCT)
- SNSPDs = superconducting nanowire single-photon detectors (Quantum Opus, LLC, Opus One, optimized for the 850-1200 nm wavelength region) with a detection efficiency of $\approx 75\%$ at 810 nm
- closed-cycle helium cryocooler (Sumitomo HC-4E2)
- temperature monitor (SIM 922)
- detector bias and readout modules (Quantum Opus, LLC, QO-SIM-CRYO)
- time tagger = picosecond event timer and time-correlated single photon counting system (PicoQuant HydraHarp 400)

Appendix H

Data for Chapter 6

The plots that follow show the datasets for each of 17 independent measurements (1 additional measurement shown in Chapter 6). Here I describe the layout of the plots which is common to all datasets. Plots 1-4 indicate the plots from left to right. Plot 1 shows count rates on D_1 as a function of measurement number. We plot the background-corrected (corr) count rates at both 0 ps and 27 ps interferometer delay. We also plot the count rates after renormalizing (norm) to minimize the impact of pump laser fluctuations which we monitor with the quadrant photodiode. Plot 2 displays the Allan deviation of ΔS as a function of the number of consecutive measurements we average over (i.e. the "chunk size"). The optimal averaging time (and corresponding minimum Allan deviation) is marked by the red point. The blue trace is the Allan deviation when we calculate ΔS with the background-corrected counts, and the orange is the Allan deviation when we calculate ΔS with the normalized counts. Our normalization procedure reduces the Allan deviation, indicating that this procedure successfully removes some of the noise caused by pump-laser fluctuations. Plot 3 displays the Allan deviation curve for our inference of p_{E2PA} (which we infer from our measurement of ΔS). The optimal averaging time (and corresponding Allan deviation) is marked by the red point. Plot 4 shows all measurements of ΔS and p_{E2PA} performed on the sample as a function of the measurement chunk number.

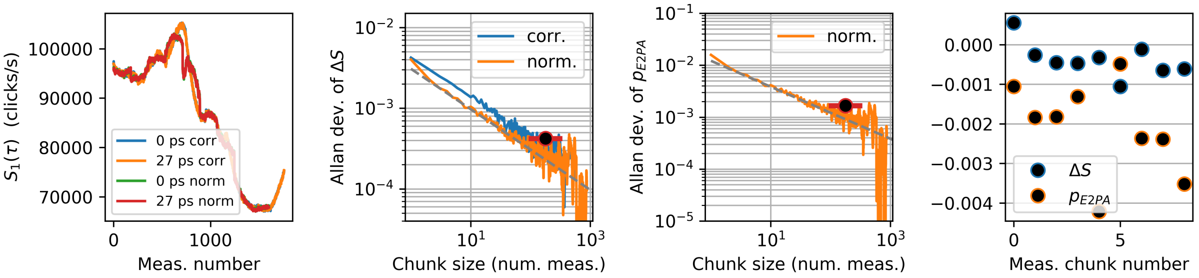

Figure H.1: Dataset for pH 11 water.

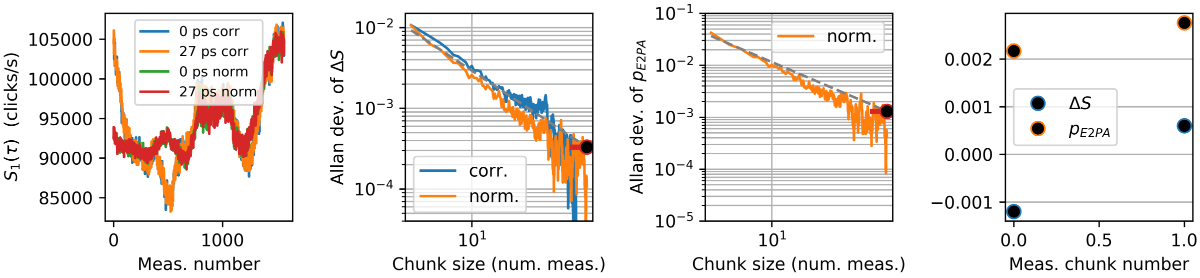

Figure H.2: Dataset for 1.9×10^{-4} mol L^{-1} fluorescein in pH 11 water.

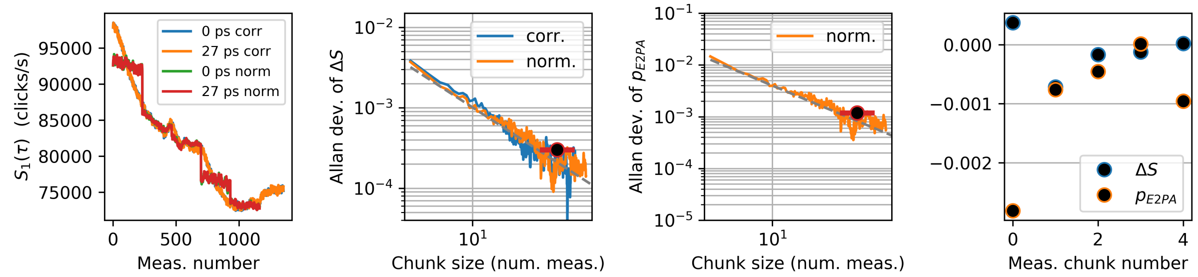

Figure H.3: Dataset for 9.4×10^{-3} mol L^{-1} fluorescein in pH 11 water.

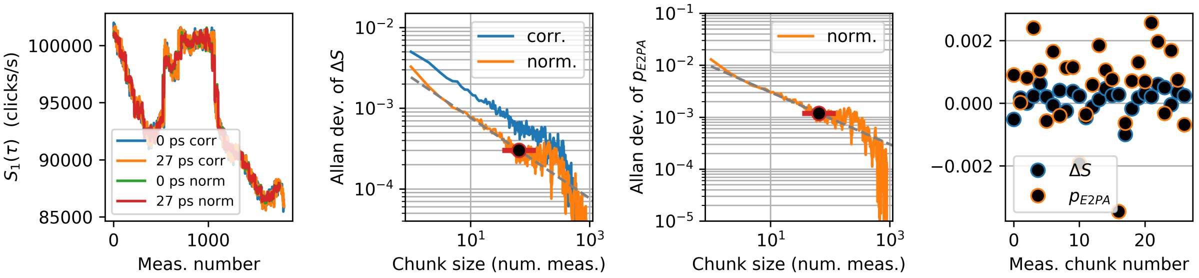

Figure H.4: Dataset for PBS.

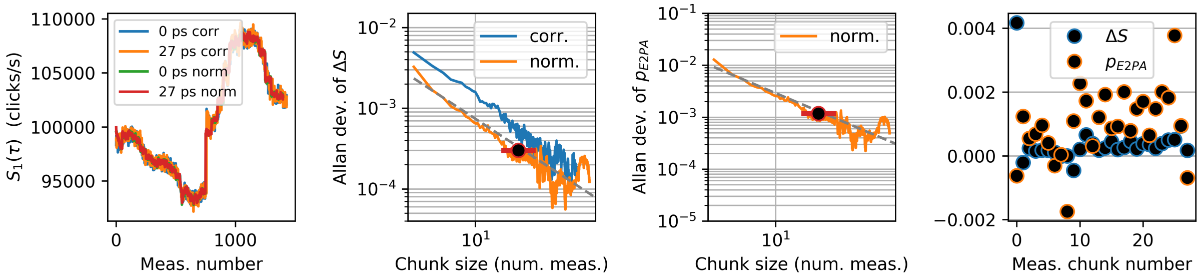

Figure H.5: Dataset for 2.9×10^{-4} mol L^{-1} FAD in PBS.

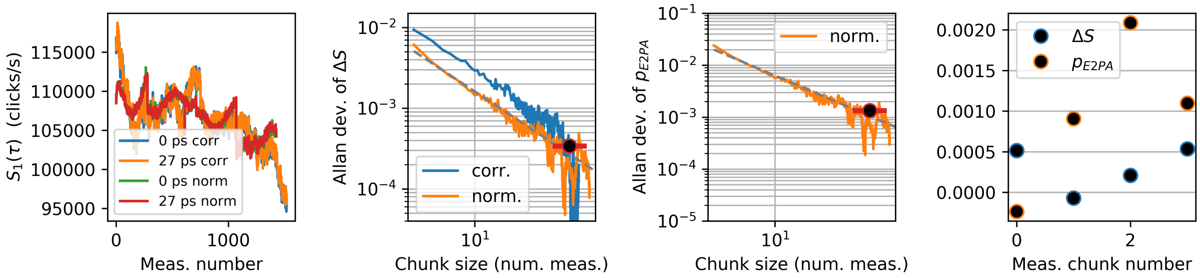

Figure H.6: Dataset for 6.7×10^{-3} mol L^{-1} FAD in PBS.

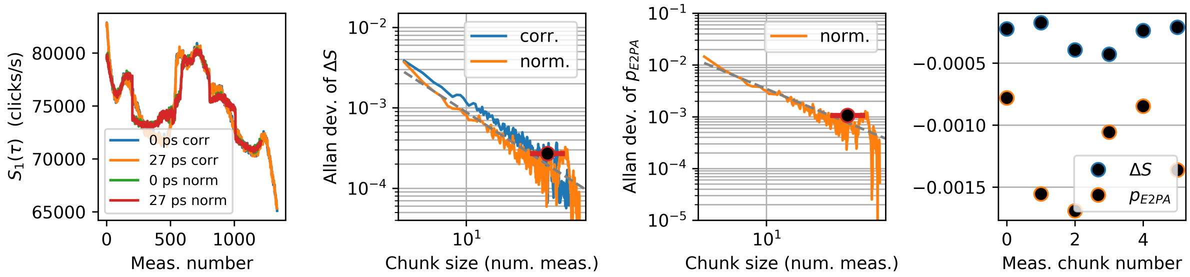

Figure H.7: Dataset for toluene.

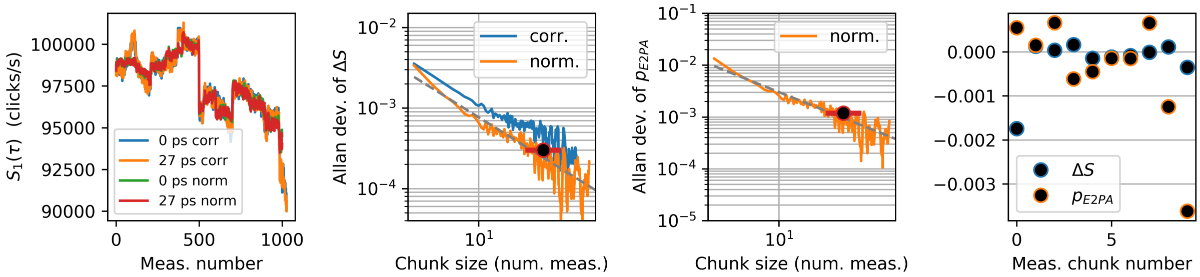

Figure H.8: Dataset for 1.65×10^{-3} mol L^{-1} ZnTPP in toluene.

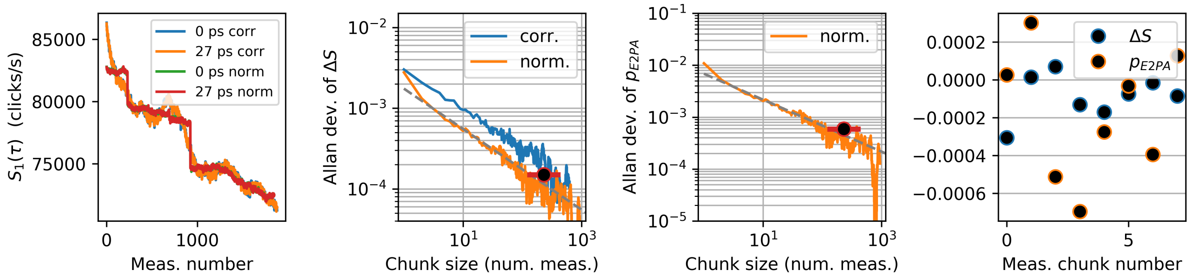

Figure H.9: Dataset for borate buffer.

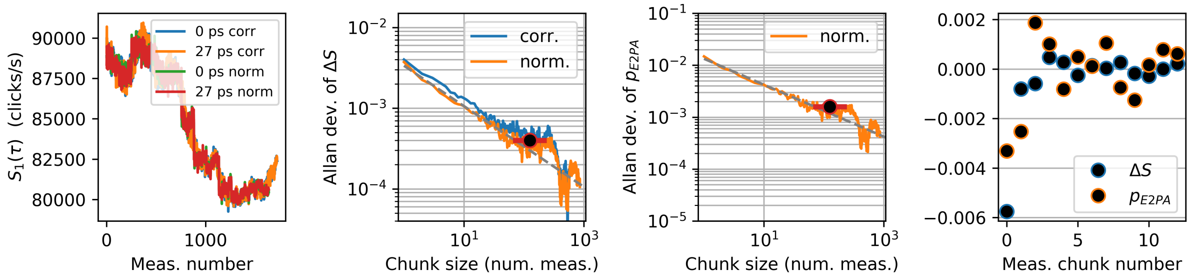

Figure H.10: Dataset for 8×10^{-6} mol L^{-1} qdot 605 in borate buffer.

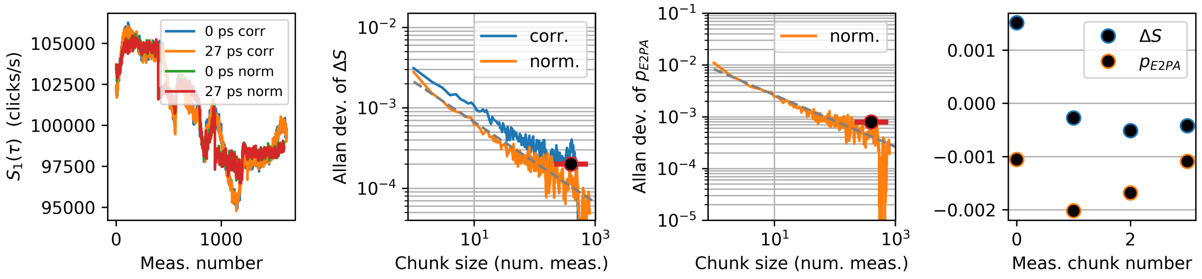

Figure H.11: Dataset for methanol.

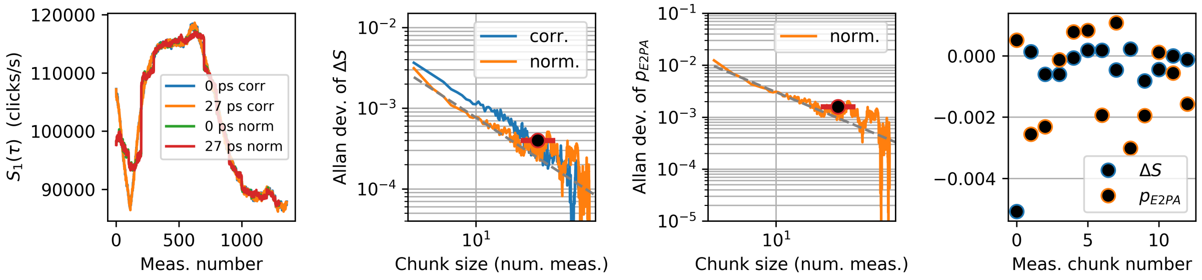

Figure H.12: Dataset for 1.8×10^{-4} mol L^{-1} Rh6G in methanol.

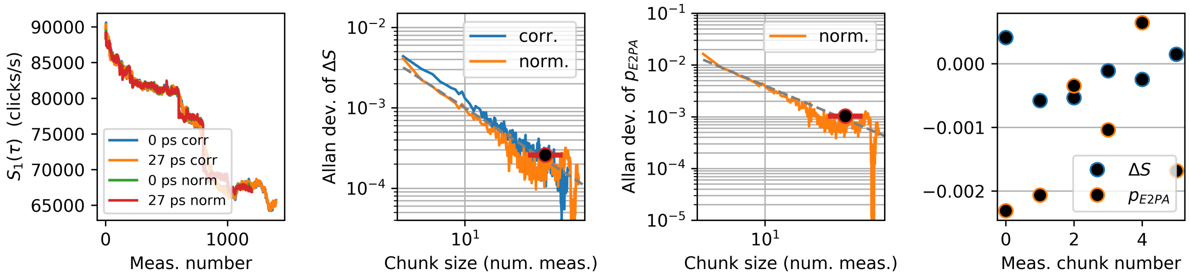

Figure H.13: Dataset for 1.1×10^{-2} mol L^{-1} Rh6G in methanol.

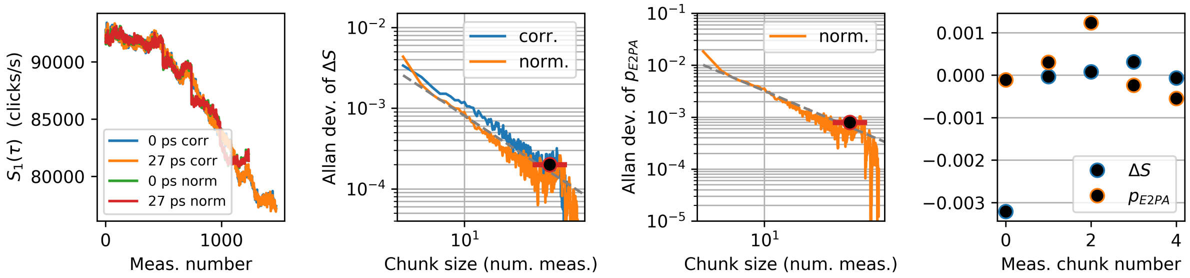

Figure H.14: Dataset for chloroform.

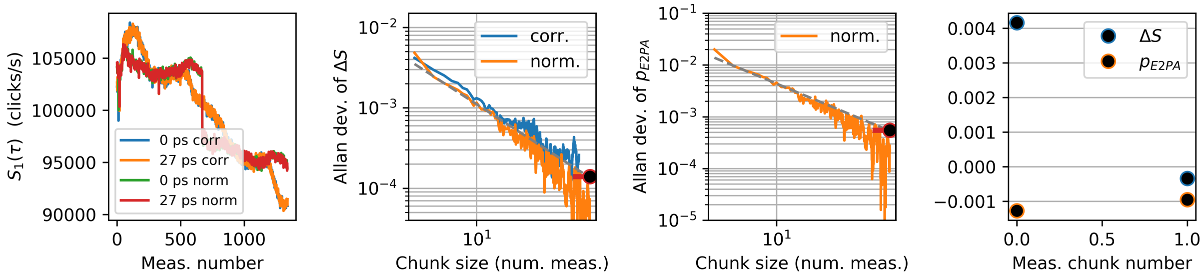

Figure H.15: Dataset for 7.3×10^{-4} mol L^{-1} 9R-S in chloroform.

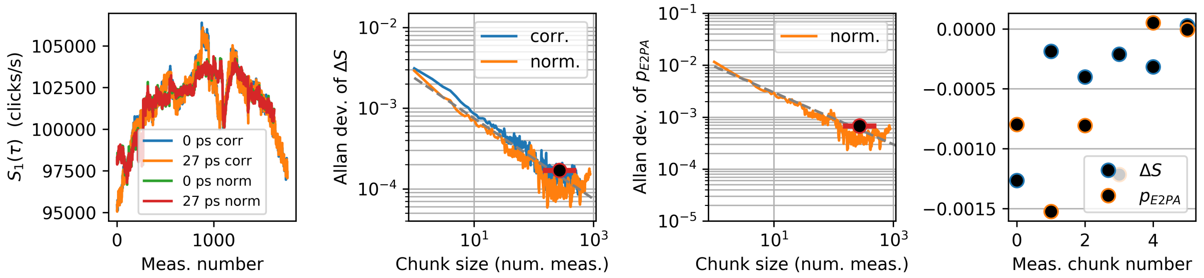

Figure H.16: Dataset for 1.7×10^{-4} mol L^{-1} AF455 in toluene.

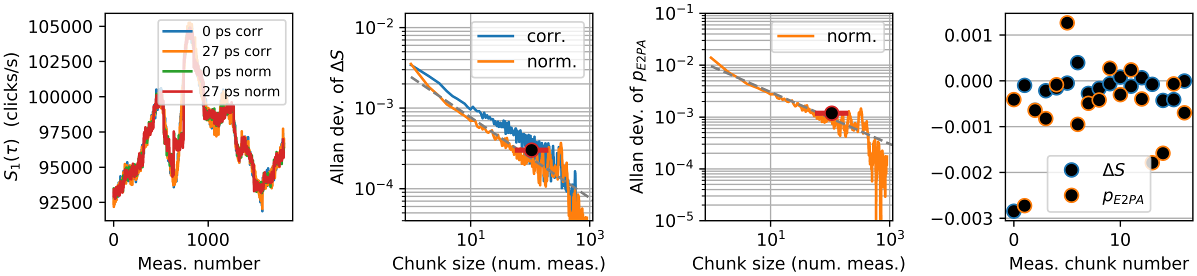

Figure H.17: Dataset for 4.0×10^{-3} mol L^{-1} AF455 in toluene.

Appendix I

Detailed experimental diagram and parts list for Chapter 7

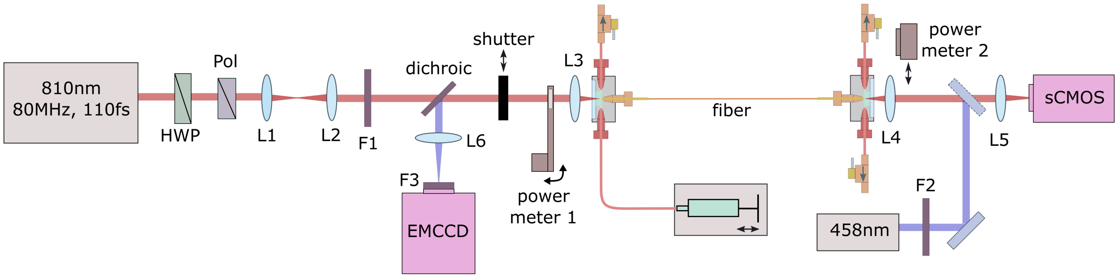

Figure I.1: Detailed diagram of our experimental setup. See main text for abbreviation definitions and part numbers.

In Fig. I.1, we show a detailed diagram of our setup with labeled parts. We list the part numbers below.

Optical components for 810 nm

- Laser source = Coherent Chameleon Discovery
- HWP = zero-order half-wave plate 808 nm (Thorlabs WPH10M-808)
- Pol = polarizing beam splitting cube (Thorlabs PBS12-780-HP)
- L1 = 200 mm focal length lens (Newport KBX076AR.16)
- L2 = 175 mm focal length lens (Thorlabs KBX073AR.16)
- F1 = neutral density filters (Thorlabs ND02A, ND20A, NE06A, NE30A, NDUV10A)

- dichroic = dichroic beamsplitter (Semrock FF738-FDi01-t3)
- shutter = optical beam shutter (Thorlabs SH05)
- K-cube solenoid controller (Thorlabs KSC101)
- power sensor 1 = photodiode sensor (Thorlabs S130C)
- power meter 1 (Thorlabs PM100D)
- motorized flip mount (Thorlabs MFF101)
- L3 = 10 mm focal length aspheric lens (Thorlabs ASL1210)
- 1 mm thick fused silica window (Edmund 84-449)
- fiber = silica capillary tubing (Molex 1068150002)
- 1 mm thick fused silica window (Edmund 84-449)
- power sensor 2 = photodiode sensor (Ophir PD300R-UV)
- power meter 2 (Ophir Starbright)
- L4 = 8 mm focal length aspheric lens (Thorlabs C240TMD)
- L5 = 125 mm focal length lens (Newport KPX097AR.16)
- sCMOS = Andor Marana back-illuminated sCMOS (MARANA-4BV6U-99BE)

Additional components for ≈ 450 nm

- 458 nm source = OBIS 458 LX
- F2 = neutral density filters (Thorlabs NE40A, NE05A)
- L6 = 125 mm focal length lens (Newport KPX097AR.14)
- F3 = filters (Semrock FF01-750/SP and FF02-470/100)
- EMCCD = Andor iXon Ultra 888 EMCCD (DU-888U3-CS0-#BV)

Microfluidics

- KDS 230 Legacy syringe pump
- 2.5 ml stainless steel syringe (KDS 780801)
- PEEK tubing (Idex 1576)
- one-way valves (Idex P-732A)
- custom-built fiber adapters (Appendix J)
- fitting (Idex F-125 Microtight)
- tubing sleeve (Idex F-181 Microtight)
- fitting (Idex F-126SX Microtight)
- AppleRubber o-ring (Viton with inner diameter of 3.56 mm and width of 0.5 mm)

Appendix J

Fiber adapter technical drawings

Here we show the technical drawings for the fiber adapter base and clamp. This adapter is designed to fit an o-ring (Viton with inner diameter of 3.56 mm and width of 0.5 mm) and window (fused silica with diameter of 5 mm and width of 1 mm) in between the base and the clamp. The adapter is used with three fittings, one for connecting to fiber (Idex F-125) and two for connecting to PEEK tubing (Idex F-126SX).

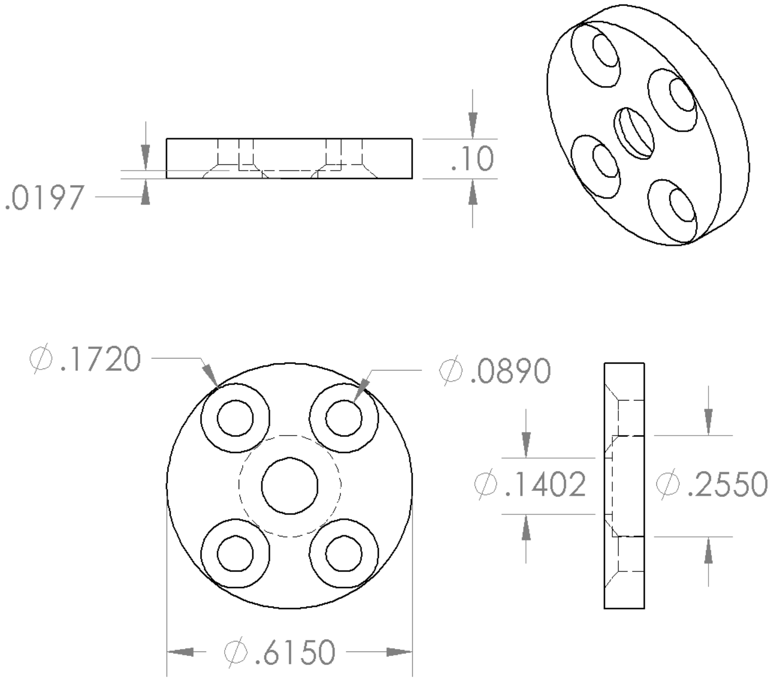

Figure J.1: Technical drawing of fiber adapter clamp. Hidden dimensions are shown as dashed lines. Dimensions are shown in inches.

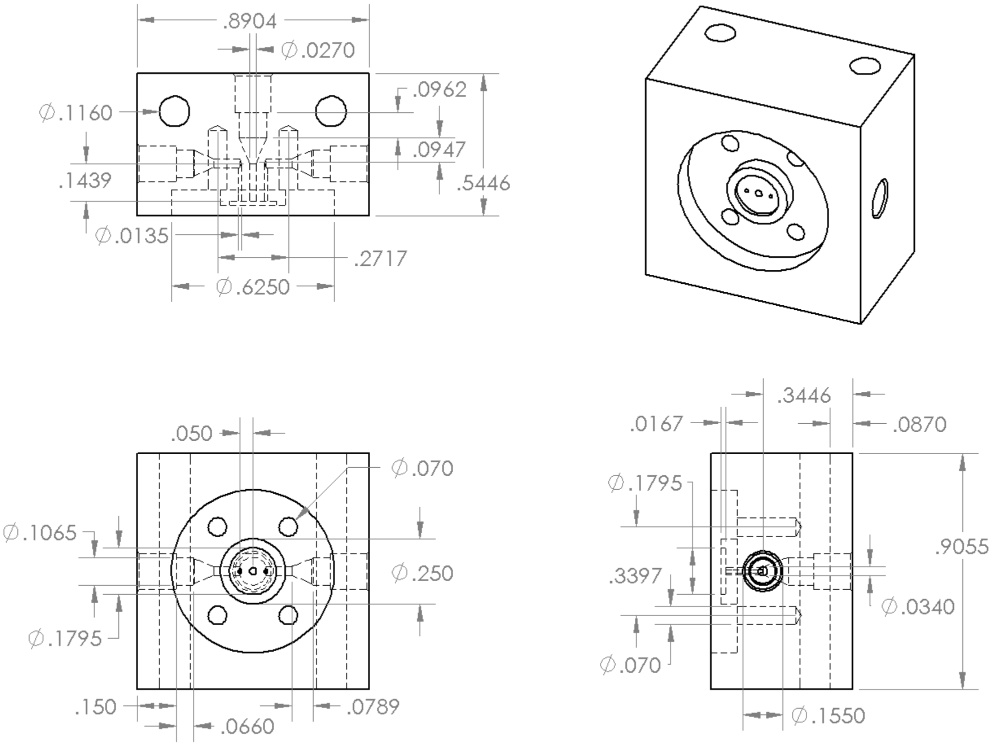

Figure J.2: Technical drawing of fiber adapter base. Hidden dimensions are shown as dashed lines. Dimensions are shown in inches.